Multiproxy Terrestrial Records of Climatic and Ecological Change During the Early Eocene Climatic Optimum

by

Ethan Gordon Hyland

A dissertation submitted in partial fulfillment
of the requirements for the degree of
Doctor of Philosophy
(Geology)
in the University of Michigan
2014

Doctoral Committee:

Associate Professor Nathan D. Sheldon, Chair
Associate Professor Catherine E. Badgley
Professor Kyger C. Lohmann
Assistant Research Scientist Selena Y. Smith
Professor Donald R. Zak

ACKNOWLEDGMENTS

I owe a great debt of gratitude to the University of Michigan and the Department of Earth and Environmental Sciences (Geology!) for helping me to accomplish all of my goals as a graduate student and build my career as a scientist. Specifically I owe this success to my advisor Nathan Sheldon and his continual support, high expectations, and friendly collaboration, and I hope to continue both our friendship and research in the future. I also thank the rest of my committee: Selena Smith, Catherine Badgley, Kacey Lohmann, and Don Zak, for their help in crafting this dissertation and improving my student experience here at Michigan.

There are many other people to thank for helping me succeed and grow as a student, researcher, teacher, collaborator, and person through my years in Ann Arbor and I cannot name them all here, but here are some: my fiancée Carli Arendt, my CERG role model Jen Cotton, my friends and fellow graduate students Rich, Lydia, Tara, Dan, Laura, Rohit, Petr, Meredith, Sarah, and the GeoFrat, my EARTH and STPP cohorts, the InSPIRE group, Iyad and my Saudi friends at the SGS and KSU, my loving and always supportive family, and the assistance, opportunities, and enthusiasm of faculty and researchers at University of Michigan and throughout the Earth science community.

And for specific chapters:

Chapter 2

For this chapter, I would like to thank my collaborator Nathan Sheldon, as well as editor and reviewer Finn Surlyk for feedback and contributions. I would also like to thank Mark Hyland for field support and sample collection, and Jennifer Cotton and Lora Wingate for assistance and suggestions in the lab. I am also grateful for the financial support of this research by the Geological Society of America's Graduate Research Grants, the American Association of Petroleum Geologists' Grants in Aid Program, and the University of Michigan's Turner Research Program.

Chapter 3

For this chapter, I would like to thank my collaborators Nathan Sheldon, Rob Van der Voo, Catherine Badgley, and Sasha Abrajevitch (Australian National University), as well as Carli Arendt and editor and reviewer Rónadh Cox for feedback and comments. I would also like to thank Jen Cotton, Henry Ferguson, Randy Southard, Neil Tabor, and Larry West for assistance in sampling and compiling modern soil series for analysis, and Meredith Dennis, Anja Schleicher, and Lydia Staisch for analytical assistance. I am also grateful for the financial support of this research by the Geological Society of America's Farouk El-Baz Research Award and National Science Foundation Awards EAR1050760 (Sheldon) and EAR0957992 (Badgley) for funding this project.

Chapter 4

For this chapter, I would like to thank my collaborators Nathan Sheldon and Majie Fan (University of Texas at Arlington), as well as editor and reviewer A. Hope Jahren for feedback and comments. I would also like to thank Carli Arendt for field support and sample collection, Lillian McMath and Richard Schwind for their hospitality and access to outcrops on private land, and Lora Wingate, Tess Nugent, and Selena Smith for assistance and discussions in the lab. I am also grateful for the financial support of this research by the Geological Society of America's Graduate Research Grants, the University of Michigan's Rackham Research Grants, and the University of Texas at Arlington (Dr. Majie Fan) for funding this project.

Chapter 5

For this chapter, I would like to thank my collaborators Nathan Sheldon, Jennifer Cotton (University of Utah/Oregon State University), and Rich Fiorella, as well as CERG lab members for feedback and comments. I would also like to thank SEGEMAR Argentina for field and sample collection assistance, and Rob Van der Voo, Meredith Dennis, and Lora Wingate for assistance and discussions in the lab. I am also grateful to the University of Michigan's Rackham International Research Grants and ExxonMobil's Geoscience Grants for funding this project.

Thank you to all who contributed!

TABLE OF CONTENTS

LIST OF FIGURES

Figure

LIST OF TABLES

Table

LIST OF APPENDICES

Appendix

ABSTRACT

The Eocene (~56–34 million years ago) was a period of major global changes, and perhaps the most substantial of these changes occurred during the Early Eocene Climatic Optimum (EECO), a period of extreme global warmth that lasted for as much as 3 million years (53–50 million years ago). This period was characterized not only by the highest global temperatures of the Cenozoic Era, but also involved high atmospheric carbon dioxide concentrations and substantial changes in the global hydrologic cycle and in global biotic diversity. These conditions make the EECO an important period for understanding Earth's climate system and its impact on the biosphere, as current projections of the future include many of the conditions experienced during the early Eocene. Problematically, few records of terrestrial conditions exist during this time period, and none are of sufficient resolution to address many of the outstanding questions about what the early Eocene may have looked like on the continents, or what changes to the global climate system may have caused the extreme conditions of the EECO. In order to address some of these questions, this dissertation employs a multiproxy approach using a wide variety of terrestrial-based paleosol and sedimentological techniques including field analysis, stable isotope and whole-rock geochemistry, paleosol magnetic analyses, phytolith analysis, and carbon cycle modeling in order to constrain and explore the climatic and ecological conditions of the early Eocene.

In Chapter 1, we introduce more fully the EECO and the methods employed for expanding high-resolution terrestrial records during the event. In Chapter 2, we present the first high-resolution multiproxy record of the EECO on land, from a site in the Green River Basin of

southwest Wyoming. We find that the warm and wet terrestrial conditions during the EECO were the result of a rapid increase in atmospheric carbon dioxide, and that the overall timescale of the peak event was much shorter than previously realized. In Chapter 3, we develop a new proxy for paleoprecipitation based on the magnetic properties of modern soils, and apply this new proxy to the record from the Green River Basin. We find that this new proxy robustly reconstructs the same hydrological conditions for the EECO, and that it is likely applicable to a much wider spatial and temporal range of paleoclimatic studies than any other available proxy. In Chapter 4, we present another high-resolution multiproxy record of the EECO from Wyoming, this time comparing our Green River Basin record to data from the nearby Wind River Basin. We find broadly similar results for regional climate, and describe a pattern of climate zone migration resulting from local topographic influences. In Chapter 5, we present a new high-resolution multiproxy record from the Southern Hemisphere (Salta Basin, Argentina) and develop a global carbon cycle model to test scenarios for different causal mechanisms of the EECO. We find distinct similarities between temperate region responses in each hemisphere, and suggest that the transient nature and terrestrial conditions of the peak EECO are inconsistent with previously suggested causal mechanisms. In Chapter 6, we summarize our overall conclusions about the early Eocene and suggest further avenues for exploring the dynamics of the EECO.

Overall, this dissertation contributes to our understanding of different climate states, and attempts to explore both the causes of and terrestrial responses to major warming events in the past. While there is more to be done in terms of explaining past events like the Early Eocene Climatic Optimum, this work provides both new techniques for developing terrestrial records and a platform for more detailed spatial and temporal examinations of rapid climatic events and their causes.

CHAPTER I

Introduction: The Early Eocene Climatic Optimum

1.1 THE EARLY EOCENE CLIMATIC OPTIMUM

Modern climate change and its global dynamics are a major concern of researchers and governments worldwide (e.g., QDRR, 2010; NRC, 2011; Zeebe, 2011; Howells et al., 2013; IPCC, 2014). As atmospheric pCO_2 continues to rise and increasing global temperatures impact the hydrological cycle (e.g., Piao et al., 2010; IPCC, 2014) and ecosystem composition (e.g., Choat et al., 2012; Garcia-Pichel et al., 2013), understanding and predicting changes in the climate system will be crucial for confronting and combating these impacts (i.e., changing water availability, migration of crop zones). Improving our understanding of warming events and examining the effects of potential high-emission climate trajectories requires the study of past greenhouse climates and their impacts on these related ecological systems (e.g., NRC, 2011; Valdes, 2011; Braconnot et al., 2012; IPCC, 2014). In order to assess future climatological and ecological responses to elevated atmospheric pCO_2 under high-emission or non-mitigation scenarios (~1000 ppm, Scenarios IV through VI; IPCC, 2014), we must examine proxy records from the past, for which the most recent analogue may be the Early Eocene Climatic Optimum (Figure 1.1).

This dissertation outlines work to expand global coverage of terrestrial proxy records of climatological and ecological change during the Early Eocene Climatic Optimum (EECO; 53–50

million years ago) and their integration with model simulations in order to evaluate potential mechanisms and directions of change. While some proxy records (e.g., Greenwood and Wing, 1995; Smith et al., 2008) and paleoclimate model simulations (e.g., Thrasher and Sloan, 2009, 2010; Winguth et al., 2010) exist for temperate continental regions (~25–45 ° N), most regions remain understudied or exhibit significant discrepancies between proxy and modeled results (e.g., Sloan, 1994; Shellito et al., 2003; Huber and Caballero, 2011; PALAEOSENS, 2012). The broad goal of this dissertation is to develop new high-resolution proxy records for these regions and test proxy and simplified carbon modeling approaches for describing the EECO. Specific objectives of this work include:

1) Documenting climatological change and climatic gradients during the EECO. This work involves expanding climate proxy records in both the Northern and Southern Hemispheres, and focuses on terrestrial sections with abundant paleosols and pedogenic materials (carbonates, clays, organic materials) that can be used to reconstruct paleotemperatures and hydrologic conditions throughout the EECO.

2) Developing a new paleoprecipitation proxy to describe high-precipitation climatic regimes characteristic of the EECO. This work involves the measurement of soil magnetic properties (goethite-hematite ratios) and climatic data for a suite of modern soils, and the development of a new climate transfer function that can be used to estimate paleoprecipitation quantitatively in a broad range of paleoenvironments.

3) Documenting patterns of ecological change during the EECO. This work involves expanding high-resolution floral proxy records at these same sites, with emphasis on well-preserved paleosols bearing plant microfossils and organic matter that can be used to reconstruct shifts in vegetation range and diversity through time.

4) Evaluating the ability of proxy methods and basic carbon cycle models to predict causes of climatic/ecological change during the EECO. Current model predictions (e.g., Huber and Caballero, 2011) of the conditions surrounding the EECO are consistently unclear about potential drivers and feedbacks for explaining proxy data on a global scale; this work compares an expanded dataset including multiple proxy types (climatological and ecological) to new carbon cycle models in order to evaluate these dynamics.

Recent work has revealed that the EECO was the warmest period in the last 65 million years (Ma herein), and correlates to major changes in both marine (e.g., Zachos et al., 2001, 2008; Hollis et al., 2012) and terrestrial records (e.g., Greenwood and Wing, 1995; Smith et al., 2008; Krause et al., 2010). Originally known primarily from marine core records, the Early Eocene Climatic Optimum is a broad temperature maximum spanning 53–50 million years ago (Mya herein) that correlates to increased atmospheric pCO_2 (e.g., Zachos et al., 2001; Demicco et al., 2003; Smith et al., 2010; Chew and Oheim, 2013). Increases in atmospheric carbon dioxide at the EECO to over 1000 ppm (3-5× preindustrial) have been previously attributed to increased volcanism and substantial changes (reduction) in silicate weathering rates through the late Paleocene–early Eocene (e.g., Figure 1.1; Zachos et al., 2008; Kent and Muttoni, 2008), and are considered the primary driver of these higher global temperatures and consequent changes in the hydrological cycle (e.g., Hren et al., 2010; Thrasher and Sloan, 2010; Chamberlain et al., 2012) and floral and faunal turnover events (e.g., Wasatchian-Bridgerian boundary; Zonneveld et al., 2000; Jaramillo et al., 2006; Stucky et al., 2009; Woodburne et al., 2009; Chew and Oheim, 2013).

Despite the broad, gradual changes observed in marine records (2–3 Ma), terrestrial records from North America (e.g., Sewall and Sloan, 2006; Smith et al., 2008; Hren et al., 2010)

and other continents (e.g., Wilf et al., 2003; Gayo et al., 2005; Krause et al., 2010) may indicate more rapid changes in temperature, precipitation, and ecology. This type of event structure, where the terrestrial climatic and ecological changes of the EECO appear more transient and severe than previously indicated by marine records (Figure 1.1), suggests that there is still significant work to be done in order to characterize fully and understand the causes and dynamics of change during the EECO, and in order to effectively apply this knowledge to other rapid climate change events like the modern.

While some work has been done to describe the climatological and ecological conditions of western North America (e.g., Greenwood and Wing, 1995; Wilf et al., 1998; Willis and McDonald, 2011) and southern South America (e.g., Wilf et al., 2003; Gayo et al., 2005; Krause et al., 2010) during the early Eocene, few quantitative data exist in terms of the high-resolution and integrated multiproxy climatological and ecological reconstructions necessary to describe the shorter-timescale terrestrial dynamics and overall causes of global change during the EECO. Therefore, this dissertation focuses on characterizing and detailing the impacts of the portion of the global EECO record that is currently most lacking: high-resolution multiproxy records of temperate latitudes in both hemispheres and their importance in tuning global carbon cycle models. This work is a synthesis of and expansion upon recent progress in the field of high-resolution terrestrial climate and ecology proxies (e.g., Strömberg et al., 2007; Yapp, 2008; Nordt and Driese, 2010; Retallack and Huang, 2010; Cotton et al., 2012; Gallagher and Sheldon, 2013), the improved characterization of the EECO event and its potential causes and impacts in the marine realm (e.g., Kent and Muttoni, 2008; Zachos et al., 2008; Stucky et al., 2009; Hollis et al., 2012), and the newest generation of carbon cycle modeling simulations (e.g., Kump and Arthur, 1999; McInerney and Wing, 2011; Zeebe, 2012; Sluijs et al., 2013).

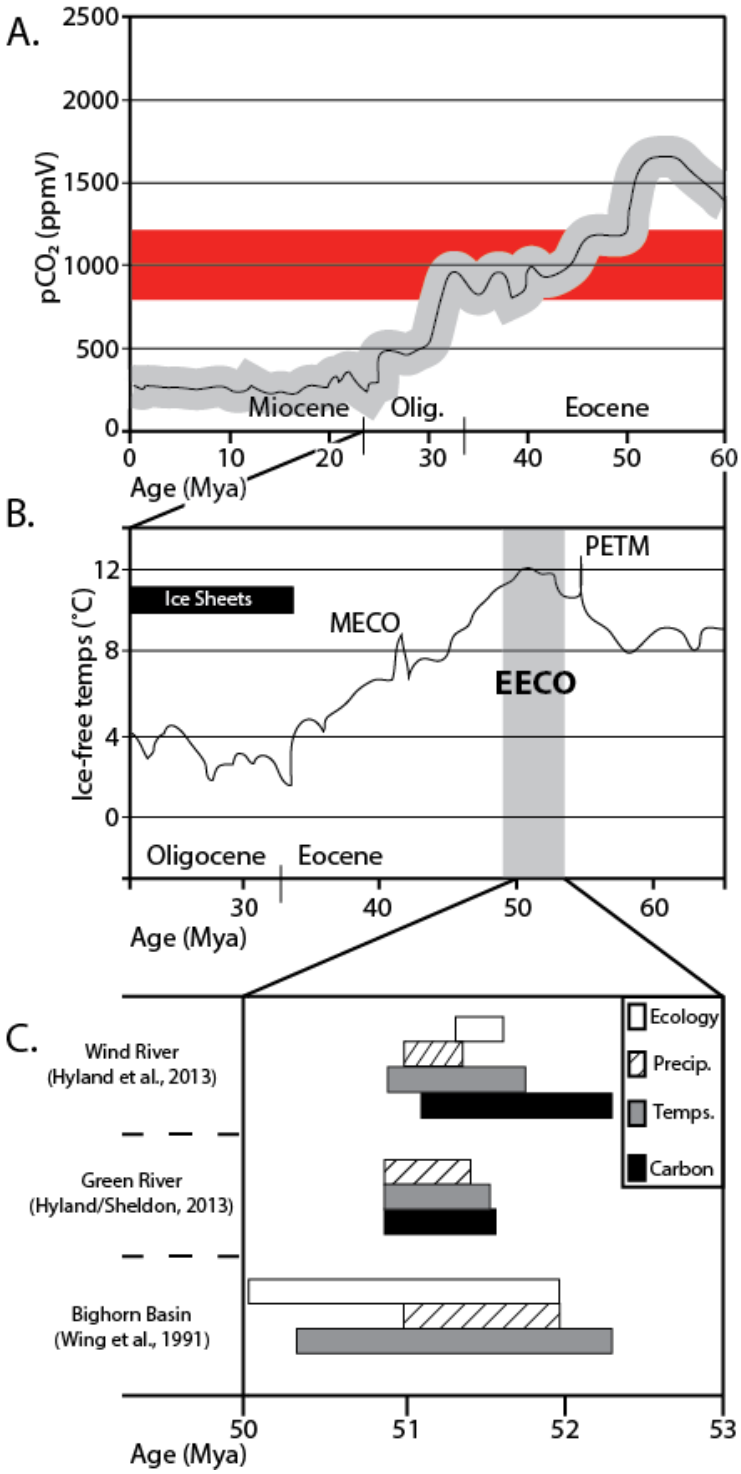

Figure 1.1 A) Atmospheric pCO_2 through time (Beerling and Royer, 2011), with labelled high-emission scenarios (red; NRC, 2011), B) bottom water temperature estimates through the Cenozoic (based on foraminiferal $\delta^{18}O$), with the EECO event labelled (gray; Zachos et al., 2008), C) exemplar timescales of terrestrial change for the EECO (this work).

1.2 TERRESTRIAL RECORDS

Throughout this dissertation, the development of high-resolution terrestrial climate and ecological records involves a number of established and newly-developed field and analytical methods, including stratigraphic and pedological description, stable isotope geochemistry, bulk paleosol elemental geochemistry, and phytolith identification and assemblage analysis. It should be noted that in terrestrial settings, due to variable deposition rates and preservation, high-resolution refers to those records which can resolve climatic and ecological changes on the order of thousands to tens-of-thousands of years (kyr herein), which in many cases means that terrestrial records inherently have lower fidelity than available marine records for the Cenozoic.

The identification of specific paleosol features allows for the environmental classification of most pedotypes based on the degree of soil development and type of preservation of environmental indicators (e.g., Mack et al., 1993; Kraus and Hasiotis, 2006), and physical measurements such as the depth-to-Bk horizon serve as quantitative proxies for climatic conditions like paleoprecipitation based on the relationship between soil water saturation and carbonate precipitation (Retallack, 2005; Sheldon and Tabor, 2009). These descriptive techniques have been used extensively for paleoenvironmental reconstructions throughout the Cenozoic, including other instances of rapid global change (e.g., Kraus, 1999; Kraus and Hasiotis, 2006; Retallack, 2012). Pedological description involved the identification of pedogenic features and pedotypes based on horizonation, color, burrowing/root traces, and ped morphologies (e.g., Mack et al., 1993; Kraus, 1999). Identified paleosols were trenched (>20 cm) to avoid modern contamination and then described and sampled on fresh surfaces. In addition, physical soil measurements (e.g., soil thicknesses, horizon depths, etc.) were taken and later corrected for burial compaction (Sheldon and Retallack, 2001).

The $\delta^{18}O$ composition of pedogenic calcite serves both as a proxy for rainfall composition values and as a proxy for atmospheric temperature. Oxygen isotope compositions of pedogenic calcite nodules are related to the isotopic compositions of the waters from which they form, which has been demonstrated to record the $\delta^{18}O$ composition of rainfall (e.g., Quade et al., 1989; Cerling and Quade, 1993; Koch, 1998). The $\delta^{18}O$ composition of these waters is also impacted by atmospheric temperature, and in many cases this composition can be related to mean annual temperatures at the time of formation (e.g., Cerling and Quade, 1993; Koch, 1998; Dworkin et al., 2005). Oxygen isotope proxies have been used extensively in describing changes in local mean temperatures, as well as rainfall and precipitation patterns due to climate and topography (e.g., Koch, 1998; Chamberlain and Poage, 2000; DeCelles et al., 2007; Quade et al., 2007; Yapp, 2008; Fox et al., 2011).

The $\delta^{13}C$ composition of both pedogenic calcite and preserved organic carbon serves as a proxy for plant type, moisture availability, and plant water use. Carbon isotope compositions of organic materials (preserved plant carbon) are related to the isotopic composition and partial pressure of atmospheric pCO_2 inside the plant, and because the primary source of variability in these factors is diffusion of CO_2 into the plant, $\delta^{13}C$ changes as a function of either plant type or water availability and use within the leaf, with greater isotopic discrimination resulting from increased rainfall (e.g., Farquhar et al., 1989; Fox and Koch, 2004; Diefendorf et al., 2010; Kohn, 2010). These carbon isotope proxies have been used widely based on the amount of isotopic discrimination to differentiate plant types (e.g., Kleinert and Strecker, 2001; Cotton et al., 2012) or in the absence of C_4 and CAM vegetation to describe water availability patterns and changes in plant type/water use efficiency as a result of climate change (e.g., Diefendorf et al., 2010, Fox et al., 2011b).

Stable isotope geochemistry included both the isotopic analyses of pedogenic carbonates ($\delta^{18}O$ and $\delta^{13}C$) and preserved organic carbon material ($\delta^{13}C$). Pedogenic carbonate analyses were conducted on a ThermoFinnigan MAT253 isotope ratio mass-spectrometer with a Kiel IV carbonate autosampling device at the Stable Isotope Laboratory at the University of Michigan. Multiple nodules were collected from each paleosol Bk horizon (> 30cm depth to avoid diffusive enrichment; Koch, 1998) and were thin-sectioned and micro-sampled to avoid diagenetically altered calcite, and each nodule was resampled to ensure reproducibility and examine intra-nodule variability. Isotopic analyses of preserved organic carbon material including carbon occluded within carbonate nodules, carbon from organic root traces, and dispersed soil carbon were conducted on a ThermoFinnigan Delta V+ isotope ratio mass spectrometer with a Costech elemental analyzer at the University of Michigan. Samples were cleaned in methanol to remove modern carbon and dissolved in dilute HCl to extract and isolate occluded organic matter. Samples were then powdered and weighed into tin capsules before being analyzed.

Major element geochemical compositions of paleosol B-horizons serve as proxies for both paleotemperature and paleoprecipitation. The development of paleosols and the accumulation and distribution of mineral phases (primary and secondary) within a soil profile are related to both the temperature and precipitation values of the environment in which they form (e.g., Sheldon and Tabor, 2009). The chemical index of alteration (CIA-K) and the paleosol weathering index (PWI) are a measure of this distribution, and change as a function of the amount of mean annual precipitation (CIA-K of Sheldon et al., 2002; CALMAG of Nordt and Driese, 2010) and mean annual temperature (PWI; Gallagher and Sheldon, 2013). Bulk paleosol geochemical proxies have been applied successfully to Cenozoic paleosols worldwide (e.g., Driese et al., 2005; Kraus and Riggins, 2007; Retallack, 2007; Sheldon, 2009; Gallagher and

Sheldon, 2013). Paleosol elemental geochemical analyses included major elements analyses of bulk samples conducted at the commercial labs of ALS Chemex in Vancouver (Canada) by X-ray fluorescence. Samples from multiple horizons of each paleosol were collected, and these sampling profiles were separately pulverized and subsampled before being analyzed. Previous replicate analyses indicate analytical uncertainty for major elements analyzed by ALS Chemex is <0.1 wt%.

Phytolith morphologies and assemblage compositions serve as a proxy for floral diversity and abundance. Phytoliths (plant biosilica microfossils) form within and between the cells of different plant structures (e.g., stems, leaves, fruits) and can be diagnostic of the plant family or ecosystem functional group (e.g., Piperno, 1988; Strömberg, 2002, 2005; Pearsall, 2011). In many cases phytolith assemblages are either directly or predictably representative of original vegetation types and abundances (e.g., Strömberg et al., 2007; Hyland et al., 2013), and have been used worldwide, but especially in North and South America, to reconstruct past ecosystems (e.g., Strömberg, 2005; Strömberg, 2011; Miller et al., 2012; Cotton et al., accepted; Hyland et al., in review). Phytolith identification involved the morphological analyses of phytolith material conducted in the preparatory laboratory space of Dr. Selena Smith at the University of Michigan. Samples were collected from paleosol A-horizons and processed via the heavy-liquid floatation method (e.g., Strömberg et al., 2007), wherein 1–2g of homogenized paleosol material was disaggregated via dissolution in dilute HCl and processed through 250 and 53 μm sieves. Samples were also cleaned of organic contaminants via dissolution in concentrated HNO_3 and $KClO_3$, and then isolated via zinc bromide heavy liquid floatation before being mounted on slides and analyzed using a petrographic microscope. Counting procedures followed the

functional group method defined by Strömberg (2003, 2005) and were interpreted using the environmental criteria of Hyland et al. (2013).

Each succeeding results chapter includes an abbreviated description of the analytical and field methods employed at a given locality or for a given chapter, and explores the application and limitations of these methods in terrestrial reconstructions.

1.3 DISSERTATION SUMMARY

This dissertation is comprised of this introductory chapter (1), followed by four results-based chapters (2–5), and concluded by a summary chapter (6). The results-based chapters use the methods discussed above (*1.2*) to address goals for understanding the Early Eocene Climatic Optimum (*1.1*). Chapter 2 establishes the first high-resolution multiproxy record of the EECO in a terrestrial locality, describing transient peak climatic and ecological conditions in the Green River Basin of western North America (Wyoming, USA). Chapter 3 describes the development of a new paleoprecipitation proxy based on magnetic properties (goethite-hematite ratio) from modern soils worldwide, and details its application to the Green River Basin locality during the EECO (with a comparison to the records generated in Chapter 2). Chapter 4 establishes a new high-resolution multiproxy record of the EECO from the Wind River Basin (Wyoming, USA), and compares these results to previous records (e.g., Chapter 2) to examine regional climate change and geographic gradients during the EECO. Chapter 5 establishes the first high-resolution multiproxy record of the EECO from the Southern Hemisphere (Salta Basin, Argentina), and compares these results to Northern Hemisphere records (e.g., Chapters 2–4) to examine global change patterns and to provide basic quantitative constraints for an early Eocene global carbon cycle model.

1.4 PUBLICATIONS RESULTING FROM THIS DISSERTATION

1) Hyland, E., Sheldon, N.D., 2013. Coupled CO_2-climate response during the Early Eocene Climatic Optimum. Palaeogeography, Palaeoclimatology, Palaeoecology 369, 125–135, **(Chapter 2).**
2) Hyland, E., Sheldon, N.D., Van der Voo, R., Badgley, C., Abrajevitch, A., *in preparation*. A new paleoprecipitation proxy based on soil magnetic properties: Implications for expanding paleoclimate reconstructions, **(Chapter 3)**.
3) Hyland, E., Fan, M., Sheldon, N.D., 2013. Terrestrial paleoenvironmental reconstructions indicate transient peak warming during the Early Eocene Climatic Optimum. Geological Society of America Bulletin 125, 1338–1348, **(Chapter 4)**.
4) Hyland, E., Cotton, J.M., Sheldon, N.D., Fiorella, R.P., *in preparation*. Constraining the Early Eocene Climatic Optimum: An inter-hemispheric comparison, **(Chapter 5)**.

REFERENCES CITED

Beerling, D.J., Royer, D.L., 2011. Convergent Cenozoic CO_2 history. Nature Geoscience 4, 418–420.

Braconnot, P., Harrison, S.P., Kageyama, M., Bartlein, P.J., Masson-Delmotte, V., Abe-Ouchi, A., Otto-Bliesner, B., Zhao, Y., 2012. Evaluation of climate models using paleoclimatic data. Nature Climate Change 2, 417–424.

Cerling, T.E., Quade, J., 1993. Stable carbon and oxygen isotopes in soil carbonates. Climate Change in Continental Isotopic Records: Geophysical Monograph 78, 217–231.

Chamberlain, C.P., Poage, M.A., 2000. Reconstructing the paleotopography of mountain belts from the isotopic composition of authigenic minerals. Geology 28, 115–118.

Chamberlain, C.P., Mix, H.T., Mulch, A., Hren, M.T., Kent-Corson, M.L., Davis, S.J., Horton, T.W., Graham, S.A., 2012. The Cenozoic climatic and topographic evolution of the western North American Cordillera. American Journal of Science 312, 213–262.

Chew, A.E., Oheim, K.B., 2013. Diversity and climate change in the middle-late Wasatchian (early Eocene) Willwood Formation, central Bighorn Basin, Wyoming. Palaeogeography, Palaeoclimatology, Palaeoecology 369, 67–78.

Choat, B., Jansen, S., Brodribb, T.J., Cochard, H., Delzon, S., Bhaskar, R., Bucci, S.J., Feild, T.S., Gleason, S.M., Hacke, U.G., Jacobsen, A.J., Lens, F., Maherali, H., Martinez-Vilalta, J., Mayr, S., Mencuccini, M., Mitchell, P.J., Nardini, A., Pittermann, J., Pratt, R.B., Sperry, J.S., Westoby, M., Wright, I.J., Zanne, A.E., 2012. Global convergence in the vulnerability of forests to drought. Nature 491, 752–755.

Cotton, J.M., Sheldon, N.D., Strömberg, C.A.E., 2012. High-resolution isotopic record of C_4 photosynthesis in a Miocene grassland. Palaeogeography, Palaeoclimatology, Palaeoecology 338, 88–98.

Cotton, J.M., Hyland, E.G., Sheldon, N.D., accepted. Multiproxy paleovegetation reconstruction constrains northwest Argentina uplift history. Earth and Planetary Science Letters.

DeCelles, P.G., Quade, J., Kapp, P., Fan, M.J., Dettman, D.L., Ding, L. 2007. High and dry in central Tibet during the Late Oligocene. Earth and Planetary Science Letters 253, 389–401.

Demicco, R.V., Lowenstein, T.K., Hardie, L.A., 2003. Atmospheric pCO_2 since 60 Ma from records of seawater pH, calcium, and primary carbonate mineralogy. Geology 31, 793–796.

Diefendorf, A.F., Mueller, K.E., Wing, S.L., Koch, P.L., Freeman, K.H., 2010. Global patterns in leaf ^{13}C discrimination and implications for studies of past and future climate. Proceedings of the National Academies of Sciences, USA, 107, 5738–5743.

Driese, S.G., Nordt, L.C., Lynn, W., Stiles, C.A., Mora, C.I., Wilding, L.P., 2005. Distinguishing climate in the soil record using chemical trends in a Vertisol climosequence from the Texas Coastal Prairie, and application to interpreting Paleozoic paleosols in the Appalachian Basin. Journal of Sedimentary Research 75, 340–353.

Dworkin, S.I., Nordt, L.C., Atchley, S., 2005. Determining terrestrial paleotemperature using the oxygen isotopic composition of pedogenic carbonate. Earth and Planetary Science Letters 237, 56–68.

Farquhar, G.D., Ehleringer, J.R., Hubick, K.T., 1989. Carbon isotope discrimination and photosynthesis. Annual Review of Plant Physiology and Plant Molecular Biology 40, 503–537.

Fox, D.L., Koch, P.L., 2004. Carbon and oxygen isotopic variability in Neogene paleosol carbonates: constraints on the evolution of the C_4-grasslands of the Great Plains, USA. Palaeogeography, Palaeoclimatology, Palaeoecology 207, 305–329.

Fox, D.L., Honey, J.G., Martin, R.A., Pelaez-Campomanes, P., 2011. Pedogenic carbonate stable isotope record of environmental change during the Neogene in the southern Great Plains, southwest Kansas, USA: Oxygen isotopes and paleoclimate during the evolution of C_4-dominated grasslands. Geological Society of America Bulletin 124, 431–443.

Fox, D.L., Honey, J.G., Martin, R.A., Pelaez-Campomanes, P., 2011b. Pedogenic carbonate stable isotope record of environmental change during the Neogene in the southern Great Plains, southwest Kansas, USA: Carbon isotopes and the evolution of C_4-dominated grasslands. Geological Society of America Bulletin 124, 444–464.

Gallagher, T.M., Sheldon, N.D., 2013. A new paleothermometer for forest paleosols and its implications for Cenozoic climate. Geology 41, 647–650.

Garcia-Pichel, F., Loza, V., Marusenko, Y., Mateo, P., Potrafka, R.M., 2013. Temperature drives the continental-scale distribution of key microbes in topsoil communities. Science 340, 1574–1577.

Gayo, E., Hinojosa, L.F., Villagran, C., 2005. On the persistence of tropical paleofloras in central Chile during the Early Eocene. Review of Palaeobotany and Palynology 137, 41–50.

Greenwood, D.R., Wing, S.L., 1995. Eocene continental climates and latitudinal temperature gradients. Geology 23, 1044–1048.

Hollis, C.J., Taylor, K.W.R., Handley, L., Pancost, R.D., Huber, M., Creech, J.B., Hines, B.R., Crouch, E.M., Morgans, H.E.G., Crampton, J.S., Gibbs, S., Pearson, P.N., Zachos, J.C., 2012. Early Paleogene temperature history of the Southwest Pacific Ocean: Reconciling proxies and models. Earth and Planetary Science Letters 350, 53–66.

Howells, M., Hermann, S., Welsch, M., Bazilian, M., Segerstrom, R., Alfstad, T., Gielen, D., Rogner, H., Fischer, G., van Velthuizen, H., Wiberg, D., Young, C., Roehrl, A., Mueller, A., Steduto, P., Ramma, I., 2013. Integrated analysis of climate change, land-use, energy, and water strategies. Nature Climate Change 3, 621–626.

Hren, M.T., Pagani, M., Erwin, D.M., Brandon, M., 2010. Biomarker reconstruction of the early Eocene paleotopography and Paleoclimate of the northern Sierra Nevada. Geology 38, 7–10.

Huber, M., Caballero, R., 2011. The early Eocene equable climate problem revisited. Climate of the Past 7, 603–633.

Hyland, E.G., Smith, S.Y., Sheldon, N.D., 2013. Representational bias in phytoliths from modern soils of central North America: Implications for paleovegetation reconstructions. Palaeogeography, Palaeoclimatology, Palaeoecology 374, 338–348.

Hyland, E., Cotton, J.M., Sheldon, N.D., in review. Evidence for orbital forcing in terrestrial Paleocene hyperthermal records. Geology.

Intergovernmental Panel on Climate Change (IPCC), 2014. Fifth Assessment Report: Climate Change (AR5), Geneva, Switzerland, IPCC, 1552 pp.

Jaramillo, C., Rueda, M.J., Mora, G., 2006. Cenozoic plant diversity in the Neotropics. Science 311, 1893–1896.

Kent, D.V., Muttoni, G., 2008. Equatorial convergence of India and early Cenozoic climate trends. Proceedings of the National Academies of Science, USA, 105, 16065–16070.

Kleinart, K., Strecker, M.R., 2001. Climate change in response to orographic barrier uplift: Paleosol and stable isotope evidence from the late Neogene Santa Maria basin, northwestern Argentina. Geological Society of America Bulletin 113, 728–742.
Koch, P.L., 1998. Isotopic reconstruction of past continental environments. Annual Reviews of Earth and Planetary Sciences 26, 573–613.
Kohn, M.J., 2010. Carbon isotope compositions of terrestrial C_3 plants as indicators of (paleo)ecology and (paleo)climate. Proceedings of the National Academies of Science, USA 107, 19691–19695. Kraus, M.J., 1999
Kraus, M.J., Hasiotis, S.T., 2006. Significance of different modes of rhizolith preservation to interpreting paleoenvironmental and paleohydrologic settings: Examples from Paleogene paleosols, Bighorn Basin, Wyoming, USA. Journal of Sedimentary Research 76, 633–646.
Kraus, M.J., Riggins, S., 2007. Transient drying during the Paleocene-Eocene Thermal Maximum (PETM): Analysis of paleosols in the Bighorn Basin, Wyoming. Palaeogeography, Palaeoclimatology, Palaeoecology 245, 444–461.
Krause, J.M., Bellosi, E.S., Raigemborn, M.S., 2010. Lateritized tephric palaeosols from central Patagonia, Argentina: a southern high-latitude archive of Palaeogene global greenhouse conditions. Sedimentology 57, 1721–1749.
Kump, L.R., Arthur, M.A., 1999. Interpreting carbon-isotope excursions: carbonates and organic matter. Chemical Geology 161, 181–198.
Mack, G.H., James, W.C., Monger, H.C., 1993. Classification of paleosols. Geological Society of America Bulletin 105, 129–136.
McInerney, F.A., Wing, S.L., 2011. The Paleocene-Eocene Thermal Maximum: A perturbation of carbon cycle, climate, and biosphere with implications for the future. Annual Reviews in Earth and Planetary Sciences 39, 489–516.
Miller, L.A., Smith, S.Y., Sheldon, N.D., Stromberg, C.A.E., 2012. Eocene vegetation and ecosystem fluctuations inferred from a high-resolution phytolith record. Geological Society of America Bulletin 124, 1577–1589.
National Research Council (NRC), 2011. Understanding Earth's Deep Past: Lessons for Our Climate Future, Washington DC, USA, National Academies Press, 209 pp.
Nordt, L.C., Driese, S.D., 2010. New weathering index improves paleorainfall estimates from Vertisols. Geology 38, 407–410.
PALAEOSENS project, 2012. Making sense of paleoclimate sensitivity. Nature 491, 683–691.
Pearsall, D.M., 2011. Phytoliths in the flora of Ecuador: University of Missouri Online Phytolith Database, http://phytolith.missouri.edu.
Piao, S., Ciais, P., Huang, Y., Shen, Z., Peng, S., Li, J., Zhou, L., Liu, H., Ma, Y., Ding, Y., Friedlingstein, P., Liu, C., Tan, K., Yu, Y., Zhang, T., Fang, J., 2010. The impacts of climate change on water resources and agriculture in China. Nature 467, 43–51.
Piperno, D., 1988. Phytolith analysis, an Archaeological and Geological Perspective. Academic Press, San Diego CA, 280 pp.
Quade, J., Cerling, T.E., Bowman, J.R., 1989. Systematic variations in the carbon and oxygen isotopic composition of pedogenic carbonate along elevation transects in the southern Great Basin, USA. Geological Society of America Bulletin 101, 464–475.
Quade, J., Garzione, C., Eiler, J., 2007. Paleoelevation reconstruction using pedogenic carbonates. Reviews in Mineralogy and Geochemistry 66, 53–87.

Quadrennial Defense Review Report (QDRR), 2010. Crafting a Strategic Approach to Climate. Department of Defense, Washington DC, 128 pp.
Retallack, G.J., 2005. Pedogenic carbonate proxies for amount and seasonality of precipitation in paleosols. Geology 33, 333–336.
Retallack, G.J., 2007. Cenozoic paleoclimate on land in North America. The Journal of Geology 115, 271–294.
Retallack., G.J., 2012. Mallee model for mammal communities of the early Cenozoic and Mesozoic. Palaeogeography, Palaeoclimatology, Palaeoecology 342, 111–129.
Retallack, G.J., Huang, C., 2010. Depth to gypsic horizon as a proxy for paleoprecipitation in paleosols of sedimentary environments. Geology 38, 403–406.
Sewall, J.O., Sloan, L.C., Huber, M., Wing, S.L., 2000. Climate sensitivity to changes in land surface characteristics. Global and Planetary Change 26, 445–465.
Sheldon, N.D., 2009. Non-marine records of climatic change across the Eocene-Oligocene transition. In: Koeberl, C., Montanari, A. (Eds.), The late Eocene Earth- Hothouse, Icehouse, and Impacts: Geological Society of America Special Paper 452, 241–248.
Sheldon, N.D., Retallack, G.J., 2001. Equation for compaction of paleosols due to burial. Geology 29, 247–250.
Sheldon, N.D., Tabor, N.J., 2009. Quantitative paleoenvironmental and paleoclimatic reconstruction using paleosols. Earth-Science Reviews 95, 1–52.
Sheldon, N.D., Retallack, G.J., Tanaka, S., 2002. Geochemical climofunctions from North American soils and application to paleosols across the Eocene-Oligocene Boundary in Oregon. The Journal of Geology 110, 687–696.
Shellito, C.J., Sloan, L.C., Huber, M., 2003. Climate model sensitivity to atmospheric CO_2 levels in early-middle Paleogene. Palaeogeography, Palaeoclimatology, Palaeoecology 193, 113–123.
Sloan, L.C., 1994. Equable climates during the Early Eocene- Significance of regional paleogeography for North American climate. Geology 22, 881–884.
Sluijs, A., Zeebe, R.E., Bijl, P.K., Bohaty, S.M., 2013. A middle Eocene carbon cycle conundrum. Nature Geoscience 6, 429–434.
Smith, M.E., Carroll, A.R., Mueller, E.R., 2008. Elevated weathering rates in the Rocky Mountains during the Early Eocene Climatic Optimum. Nature Geoscience 1, 370–374.
Smith, R.Y., Greenwood, D.R., Basinger, J.F., 2010. Estimating paleoatmospheric pCO_2 during the Early Eocene Climatic Optimum from stomatal frequency of Ginkgo, Okanagan Highlands, British Colombia, Canada. Palaeogeography, Palaeoclimatology, Palaeoecology 293, 120–131.
Strömberg, C.A.E., 2002. The origin and spread of grass-dominated ecosystems in the late Tertiary of North America: preliminary results concerning the evolution of hypsodonty. Palaeogeography, Palaeoclimatology, Palaeoecology 177, 59–75.
Strömberg, C.A.E., 2003. The origin and spread of grass-dominated ecosystems during the Tertiary of North America and how it relates to the evolution of hypsodonty in Equids. University of California Berkeley (PhD Thesis), 779 pp.
Strömberg, C.A.E., 2005. Decoupled taxonomic radiation and ecological expansion of open-habitat grasses in the Cenozoic of North America. Proceedings of the National Academies of Sciences, USA, 102, 11980–11984.
Strömberg, C.A.E., 2011. Evolution of grasses and grassland ecosystems. Annual Reviews of Earth and Planetary Sciences 39, 517–544.

Strömberg, C.A.E., Werdelin, L., Friis, E.M., Sarac, G., 2007. The spread of grass-dominated habitats in Turkey and surrounding areas during the Cenozoic: Phytolith evidence. Palaeogeography, Palaeoclimatology, Palaeoecology 250, 18–49.
Stucky, R., Chew, A., Hailu, M., 2009. Alpha species diversity in early-middle Eocene mammalian communities of the Bighorn, Bridger, and Wind River Basins, Wyoming: High species diversity correlates with global warming during the Early Eocene Climatic Optimum. Journal of Vertebrate Paleontology 29, 187–207.
Thrasher, B.L., Sloan, L.C., 2009. Carbon dioxide and the early Eocene climate of western North America. Geology 37, 807–810.
Thrasher, B.L., Sloan, L.C., 2010. Land cover influences on the regional climate of western North America during the early Eocene. Global and Planetary Change 72, 25–31.
Valdes, P., 2011. Built for stability. Nature Geoscience 4, 414–416.
Wilf, P., Wing, S.L., Greenwood, D.R., Greenwood, C.L., 1998. Using fossil leaves as paleoprecipitation indicators: An Eocene example. Geology 26, 203–206.
Wilf, P., Cuneo, N.R., Johnson, K.R., Hicks, J.F., Wing, S.L., Obradovich, J.D., 2003. High plant diversity in Eocene South America: Evidence from Patagonia. Science 300, 122–125.
Willis, K.J., MacDonald, G.M., 2011. Long-term ecological records and their relevance to climate change predictions for a warmer world. Annual Reviews of Ecology, Evolution, and Systematics 42, 267–287.
Winguth, A., Shellito, C., Shields, C., Winguth, C., 2010. Climate response at the Paleocene-Eocene Thermal Maximum to greenhouse gas forcing- a model study with CCSM3. Journal of Climate 23, 2562–2584.
Woodburne, M.O., Gunnell, G.F., Stucky, R.K., 2009. Climate directly influences Eocene mammal faunal dynamics in North America. Proceedings of the National Academies of Sciences, USA, 106, 12399–12402.
Yapp, C.J., 2008. 18O/16O and D/H in goethite from a North American Oxisol of the Ealy Eocene climatic optimum. Geochimica et Cosmochimica Acta 72, 5838–5851.
Zachos, J.C., Pagani, M., Sloan, L.C., Thomas, E., Billups, K., 2001. Trends, rhythms, and aberrations in clobal climate 65 Ma to Present. Science 292, 686–693.
Zachos, J.C., Dickens, G.R., Zeebe, R.E., 2008. An early Cenozoic perspective on greenhouse warming and carbon-cycle dynamics. Nature 451, 279–283.
Zeebe, R.E., 2011. Where are you heading Earth? Nature Geoscience 4, 416–418.
Zeebe, R.E., 2012. LOSCAR: Long-term ocean-atmosphere-sediment carbon cycle reservoir model v2.0.4. Geoscience Modeling Developments 5, 149–166.
Zonneveld, J.P., Gunnell, G.F., Bartels, W.S., 2000. Early Eocene fossil vertebrates from the southwestern Green River Basin, Lincoln and Uinta Counties, Wyoming. Journal of Vertebrate Paleontology 20, 369–386.

CHAPTER II

Coupled CO_2-climate response during the Early Eocene Climatic Optimum

Official citation:
Hyland, E.G., Sheldon, N.D., 2013. Coupled CO_2-climate response during the Early Eocene Climatic Optimum. Palaeogeography, Palaeoclimatology, Palaeoecology 369, 125–135.

ABSTRACT

The Early Eocene Climatic Optimum (EECO) has been characterized as a prolonged warm event indicated by increased atmospheric pCO_2, temperatures, precipitation, and biological turnover. A new paleoenvironmental reconstruction using integrated pedological, geochemical, and isotopic data from the Green River Basin (Green River/Great Divide region) provides a high-resolution record of environmental and climatic change throughout the EECO. Our reconstruction indicates that this region, and likely much of the margin of paleolake Gosiute, was a stable, fluvially-controlled floodplain environment with evidence of large scale continuous soil development and features comparable with modern Alfisols (temperate forest soils). Regional climate data from multiple proxies indicates that the period was warm-temperate and semi-arid to sub-humid, with a peak interval from about 51.5–50.9 Mya that exhibits significantly warmer (~7˚C) and wetter (~750 mm yr^{-1}) conditions, resulting in major changes to the local weathering regime. Isotopic analyses also indicate a rapid increase to high atmospheric pCO_2 values (~1700 ppmV) and a shift in the $\delta^{13}C$ composition of pedogenic carbonates during this peak interval that appear to define and provide a cause for this significant regional response to global climatic

change. The new data, when combined with foraminiferal $\delta^{13}C$ records, are consistent with CO_2 ventilation from a deep marine reservoir source. This multi-proxy reconstruction suggests that the EECO may have had a superimposed “peak” of climatic and ecological change on land.

2.1 INTRODUCTION

2.1.1 Early Eocene Climatic Optimum

Intracontinental lacustrine basins are important study locations due to their great potential for the preservation of terrestrial climate records across key time intervals such as the Early Eocene Climatic Optimum (EECO). Analyzing the sedimentological features of these types of basins and supplementing that information with paleopedological, geochemical, and isotopic evidence allows for an integrated understanding of the paleoenvironmental factors involved in their evolution. The EECO is a period during the early to middle Eocene (53–50 Mya) that has been shown both with marine (Zachos et al., 2001; Pearson et al., 2001) and terrestrial (Greenwood and Wing, 1995) records to be a long-term global temperature maximum. It is broadly coincident with and has been causally linked to high atmospheric CO_2 levels thought to correspond to increased volcanic emissions and reduced silicate weathering (Zachos et al., 2008), though the extent of these high concentrations is poorly constrained (e.g., Retallack, 2001a; Berner and Kothavala, 2001; Yapp, 2004). Evidence from a variety of localities in western North America indicates that during this period many continental basins experienced extreme changes in regional temperatures, precipitation patterns, and faunal turnover (e.g., Clyde et al., 2001; Sewall and Sloan, 2006). Because changes associated with this event have also been observed globally (e.g., Wilf et al., 2003; Ivany et al., 2008), it is possible to analyze the differential effects of global events on localized basin environments. Herein, we discuss new high-resolution records of paleoclimatic and paleoenvironmental changes from Wyoming during the EECO and assess regional responses to global change.

2.1.2 Geological Setting

Our sites are located in southwestern Wyoming (Figure 2.1), on the northeastern margin of the Green River/Great Divide Basin (bounded to the north by the Wind River Range), which formed along with many other local basins in response to the Laramide Orogeny (Roehler, 1992; 1993). Paleogeographic reconstructions and paleomagnetic data (Scotese, 2000; Clyde et al., 2001) indicate that the basin maintained a latitude of roughly 41° N during the early Eocene, ~1-2° south of its present latitude (~42.3° N). This latitudinal difference likely had little effect on local climatic conditions, as modeled Eocene circulation patterns vary negligibly for this region (Thrasher and Sloan, 2009).

The Wasatch Formation itself is the result of synorogenic alluvial/fluvial sedimentation and volcaniclastic material that tracks changes in the size/shape of endorheic paleolake Gosiute (Smith et al., 2008). Clyde et al. (2001) previously identified paleosols in the Wasatch and Bridger Formations and used oriented hand samples to construct a magnetostratigraphic record wherein these investigation sites correlated to late Chron 23r through early Chron 22n. Work by Smith et al. (2008) confirmed this correlation and combined the data with new radiometric ages from Wasatch Formation sections in other parts of the Green River Basin to indicate that the Formation was deposited during the Early Eocene Climatic Optimum (53–50 Mya). We base our age model on this data and the slight revision of the GPTS time scale by Gradstein et al. (2004), which suggests that this stratigraphic section spans the time period identified by other records (e.g., Zachos et al., 2001) as the EECO.

Clyde et al. (2001) also made preliminary environmental characterizations when they documented anomalously heavy isotopic C values from pedogenic carbonates that suggested either water-stressed conditions or early C_4 vegetation. However, no further quantitative

paleoclimatic or paleobotanical reconstructions exist for these localities, so it was not previously possible to characterize changes in the environmental conditions during the EECO. This work focuses on Clyde et al.'s (2001) distinct but well-correlated buttes exposed along the badlands-type topographic front known as the Honeycomb, roughly 30 km southeast of South Pass City, Wyoming. The sites are contemporaneous and correlated via laterally continuous marker beds, and are henceforth referred to as HB1 (42.2288°N, 108.5307°W; ~86 m of section) and HB2 (42.2179°N, 108.5450°W; ~114 m of section).

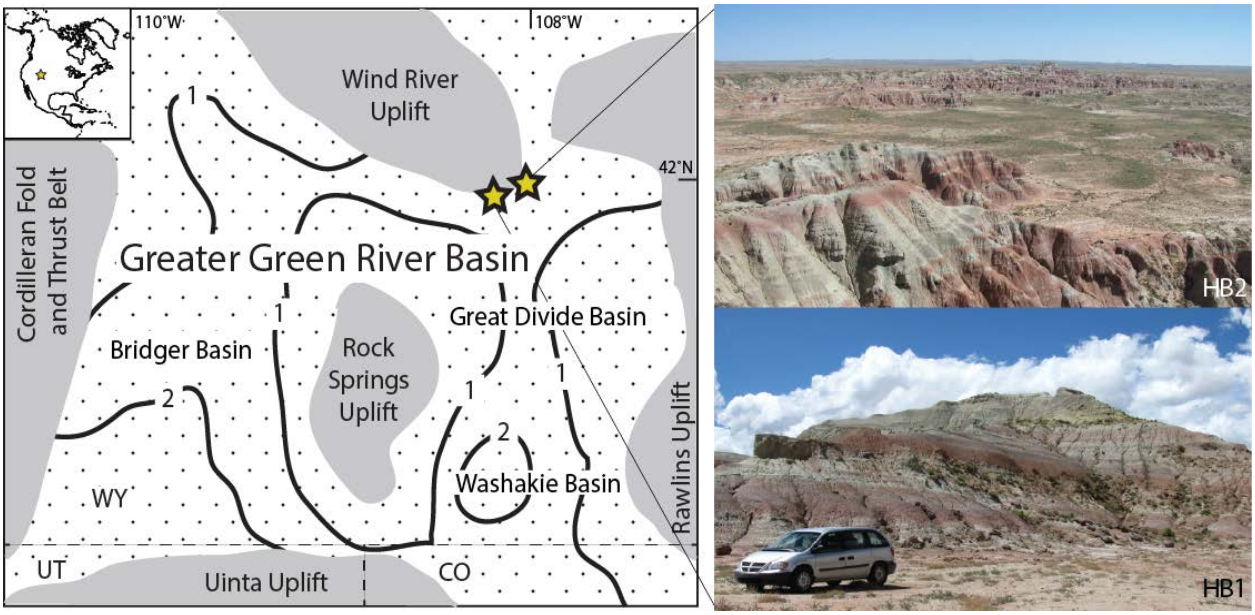

Figure 2.1 General location and field photos of sites within the Green River/Great Divide Basin. Gray color indicates Proterozoic crystalline basement, stippling indicates Paleocene/Eocene sediments. Black lines with numbers are rough sediment thickness isolines (in km; Smith et al., 2008). Stars are approximate locations of sites HB1 and HB2, and both field photos are roughly north-facing.

2.2 METHODS

2.2.1 Physical measurements

This work began with the identification and analysis of paleosol profiles in two different stratigraphic sections (HB1 and HB2) of the Wasatch Formation that were measured and described in stratigraphic context, including characterization of the depositional/sedimentary facies after Mack et al. (1993). These sections were pre-selected to include paleosols that were part of Clyde et al.'s (2001) paleomagnetic record of the Wasatch/Bridger Formations, so that the age of each section is known precisely (52–50.6 ± 0.1 Mya). Geological ages of individual paleosols were determined by linear interpolation based on constant sedimentation rates (107 m Ma^{-1}) between each of the tie points of the magnetostratigraphic succession described by Clyde et al. (2001). The two sections were correlated via horizontal transects along individual paleosols and by magnetostratigraphy (Clyde et al., 2001). Each paleosol profile was identified on the basis of pedogenic features including horizonation, color, and burrowing/root traces (e.g., Kraus, 1999). Paleosols were then trenched to a depth of at least 20 cm to minimize the risk of modern contamination, described, and sampled throughout depth profiles and for significant pedogenic features. Paleoclimatic estimates and soil/environmental characterizations were made from an integrated stratigraphic dataset based on three independent proxies: 1) physical properties, such as depth to Bk (carbonate-bearing) horizon; 2) geochemical properties, such as the degree of chemical weathering; and 3) the isotopic composition of carbon ($\delta^{13}C$) and oxygen ($\delta^{18}O$) from pedogenic carbonates and carbonate-occluded organic matter.

Physical measurements were recorded from 107 individual paleosols throughout the two stratigraphic sections and combined to form a comprehensive record. This includes Bk horizon depth (e.g., Retallack, 1994), which is measured from the top of the paleosol profile and

corrected for dip and compaction (Sheldon and Retallack, 2001). This method was criticized by Royer (1999), who used an expanded database relative to Retallack's (1994) original work and found very little relationship between Bk horizon depth and MAP, and by Driese and Ober (2005), who noted that the relationship performed poorly when applied to Vertisols. However, there are no Vertisols at our site (Table 2.1), and as Retallack (2000) noted, many of the soils in Royer's (2000) compilation either lacked any carbonate at all or were otherwise unsuitable on the basis of the constraints in the original paper (e.g., inclusion of hill-slope soils). Retallack (2005) refined the method, integrating many of Royer's (1999) criticisms, and we apply the revised version here. In particular, the results are compared with geochemistry-derived estimates (see Results*;* Sheldon and Retallack, 2004; Retallack, 2007), and where available, to paleobotanical results as a check on their validity. The revised climofunction for mean annual precipitation (MAP) uses Bk depth (*D*, in cm) as follows:

$$\text{MAP (mm yr}^{-1}) = -0.013D^2+6.45D+137.2$$

(SE = ±147 mm yr^{-1}, R^2 = 0.52; Retallack, 2005), (2.1)

These calculated values provide a minimum estimate for mean annual precipitation, as truncation of profiles can decrease the measured depth to Bk horizon (Sheldon and Tabor, 2009).

Table 2.1 Classification of pedotypes.

Pedotype	Soil type[a]	Paleosol type[b]	Diagnosis	Age (yrs)	HB1[c]	HB2[c]
Killpecker	Inceptisol	Protosol	Colored (Bw) horizon, some root traces	~10^3	15	13
Buffalo Hump	Entisol	Protosol	Same as above, with relict primary structure (laminations)	~10^2	9	4
Honeycomb	Alfisol	calcic Argillisol	Root traces, argillic (Bt) horizon, carbonate-bearing (Bk) horizon	~10^4	9	14
Point of Rocks	Alfisol	Argillisol	Same as above, without Bk horizon	~10^4	5	14
Sweetwater	Alfisol	Gleysol	Root traces, argillic (Bt) horizon with mottling and redoximorphic features	~10^5	6	10
North Fork	Alfisol	calcic Gleysol	Same as above, with carbonate nodules (Bk)	~10^5	3	5
				Total	47	60

a Soil Survey Staff (1999)
b Mack et al. (1993)
c Number of soils of each type logged at this site location.

2.2.2 Geochemistry

Geochemical proxies were applied to major element compositions obtained from X-ray fluorescence (XRF) whole rock analyses (n = 75) of selected paleosol depth profiles (primarily Bt horizons of well-developed soils). Samples were run at ALS Chemex Lab in Vancouver (BC) Canada, where average analytical uncertainty from XRF analyses is 0.001%, and duplicate analyses had a mean standard deviation of 0.015%. Climofunctions used here include estimates of precipitation, long-term weathering, and temperature. Modern soils that receive higher mean annual precipitation display greater degrees of chemical weathering, and this relationship has been widely applied to soils of varying type and age (e.g., Driese and Ober, 2005; Sheldon, 2005; Hamer et al., 2007; Kraus and Riggins, 2007) and compared to other independent precipitation proxies (e.g., paleobotanical estimates; Sheldon et al., 2002; Retallack, 2007) with consistent results. A transfer function relating the chemical index of alteration without potassium (*CIA-K*; Maynard, 1992) to mean annual precipitation is given by the following:

$$\text{MAP (mm yr}^{-1}) = 221.1e^{0.0197(CIA\text{-}K)}$$

(SE = ±182 mm yr^{-1}, $R^2 = 0.72$; Sheldon et al., 2002). (2.2)

As previously noted (Sheldon et al., 2002; Sheldon and Tabor, 2009), the proxy cannot be applied to hill-slope paleosols, paleosols with inherited carbonate (e.g., limestone parent material), or to lateritic paleosols, and Nordt and Driese (2010) recently improved performance for Vertisols by deriving a new paleoprecipitation proxy for that soil order. There are no Vertisols at our site (Table 2.1), nor any evidence of hill-slopes, inherited carbonate, or laterites, so equation (2) is appropriate in this case.

Trends in long-term chemical weathering are also tied to factors like changes in precipitation and seasonality affecting rates of pedogenesis (e.g., Sheldon, 2009), and were

reconstructed using a three-point running average of the deviation in weathering between individual paleosols (CIA_x) and mean weathering for the entire sequence (μCIA):

$$\Delta W = CIA_x - \mu CIA$$

(Sheldon and Tabor, 2009; Sheldon et al., 2012). (2.3)

Paleotemperature can also be estimated from the degree of chemical weathering present in the Bt horizon, using a climatic function relating mean annual temperature (MAT) to the degree of salinization; soils that accumulate salts (K, Na) tend to be in regions with low mean annual temperatures, so the ratio of potash and soda to alumina (*S*) provides an estimate of MAT (Sheldon et al., 2002). However, while this index can be used to quantify paleotemperature values, we interpret it as an indicator of the vector of change rather than as a quantitative proxy, as recent work (e.g., Sheldon, 2009) has shown that in some cases the reconstructed values are difficult to reconcile with other lines of evidence (paleobotanical assemblages and evaporitic deposits), but that *S* itself closely follows directional temperature trends. We choose to include this vector-of-change estimate in our results because for an integrated climatic description, the use of multiple proxies is crucial for confirming the accuracy of individual datasets.

2.2.3 Isotopic proxies

For isotopic studies, multiple pedogenic carbonate nodules were collected from Bk horizons (n = 29) throughout both stratigraphic sections at a depth of >30 cm below the paleosol surface so that diffusive enrichment by atmospheric CO_2 could be discounted (Koch, 1998). Nodules were sawn in half and thin-sectioned to identify micritic calcite for spot sampling using a microdrill to avoid sparry or diagenetically altered calcite. Calcite samples were analyzed using a ThermoFinnigan MAT 253 isotope ratio mass spectrometer with KielIV autosampler at the University of Michigan, and results are reported in per mil units relative to the Vienna Pee Dee

Belemnite (VPDB). NBS 18 and 19 were used as internal standards to normalize values to VPDB, and analytical error is maintained at less than 0.1‰ for both carbon ($\delta^{13}C_{carb}$) and oxygen ($\delta^{18}O_{carb}$) compositions.

For $\delta^{13}C_{org}$ analyses, carbonate nodules and organic root traces (n = 39) from the same stratigraphic levels were cleaned in methanol to remove modern carbon and the carbonates were dissolved in dilute (7%) HCl to extract and isolate occluded organic matter. Organic root trace samples were also treated with dilute (7%) HCl to remove detrital carbonate, and both types of samples were powdered with a mortar and pestle and weighed into tin capsules. Samples were then analyzed using a Costech elemental analyzer attached to a Finnigan Delta V+ isotope ratio mass spectrometer at the University of Michigan, and results are also reported in units per mil (‰) relative to the Vienne PeeDee Belemnite (VPDB). IAEA sucrose and caffeine standards were used for the organic carbon analyses, and analytical error for those measurements is also maintained at less than 0.1‰.

The isotopic data were used in estimates of paleotemperature and atmospheric pCO_2 concentrations. Based on the empirical relationship between temperature and water/calcite in modern soils (Cerling and Quade, 1993) and calibrations for paleosol $\delta^{18}O$ values (‰ VPDB; e.g., Nordt et al., 2003; Prochnow et al., 2006), a temperature (*T*, in °C) relationship can be derived from paleosol carbonates:

$$T = 1.1415(\delta^{18}O) + 20.805$$

(SE = ±0.5°C, R^2 = 0.57; modified from Dworkin et al., 2005). (2.4)

This method does have some issues with error estimation due to $\delta^{18}O$ heterogeneity within nodules. For example, the calculated error function of Dworkin et al. (2005) includes only potential error from the analytical uncertainty of $\delta^{18}O$ values and not inter- and intra-nodule

variability. Important factors like the variable composition of rainfall (i.e., meteoric $\delta^{18}O$) and soil water values (due to evaporation) between isothermal sites are unaccounted for in the additional calibration (Sheldon and Tabor, 2009), so external verification of estimates (via alternate proxies like paleosol salinization) is important, and the "true" uncertainty in the paleotemperature estimates is higher than Dworkin et al. (2005) reported, on the order of a standard error of ±4.1 °C. We have applied this more conservative error throughout, which we calculated by replotting original modern soil carbonate $\delta^{18}O$ values (Cerling and Quade, 1993) and calculating standard error on the relationship, which accounts for both the quoted analytical error (Dworkin et al., 2005) as well as sources like inter-nodule and meteoric water variability. Recalibrating this error function to accommodate $\delta^{18}O$ variability, as well as comparing these values with other independent temperature proxies like Bt horizon salinization (as above), is crucial for verifying their accuracy in estimating paleotemperatures as other work (Fox and Koch, 2004) has demonstrated for periods of rapid climate change.

Estimates of atmospheric pCO_2 are also complicated and can be poorly constrained for some parts of the paleorecord (e.g., Paleozoic). However, useful approximations can be made via refinements of the relationship to the paleosol pedogenic carbonate paleobarometer discussed at length by Cerling (1992) and Ekart et al. (1999):

$$pCO_2 \text{ (ppmv)} = Sz\ ((\delta^{13}Cs - 1.0044 * \delta^{13}Cr - 4.4)/(\delta^{13}Ca - \delta^{13}Cs)) \qquad (2.5)$$

The basis for the variables within this equation are described in detail and refined to fit observations of modern soils, but generally: S_z is the concentration of soil respired CO_2, which is calculated for each included paleosol via the empirically derived soil CO_2-precipitation equations of Cotton and Sheldon (2012), and is based on our MAP proxy estimates; $\delta^{13}C_s$ is the carbon isotopic composition of pedogenic calcite corrected for temperature fractionation effects, which

is calculated for each paleosol by inputting our $\delta^{18}O$ paleothermometry results into the transfer function of Romanek et al. (1992); $\delta^{13}C_r$ is the carbon isotopic composition of preserved organic matter recovered both from dissolved carbonate nodules and directly from the paleosol (e.g., Retallack, 2009); and $\delta^{13}C_a$ is the estimated atmospheric carbon isotopic composition for the time period, including modeled shifts in the $\delta^{13}C$ composition, from Tipple et al. (2010). Numerical values in the equation are empirically derived constants for fractionation resulting from the differential diffusion of CO_2 containing different carbon species (1.0044; Cerling, 1991), and the constant diffusive enrichment of soil CO_2 relative to respired CO_2 (4.4‰; Cerling, 1991). Error for this function is calculated as a summation of Gaussian error propagation for each involved term as in Retallack (2009).

It should be noted that multiple modifications have been suggested for improving the pCO_2 paleobarometer by including better estimates of soil respired CO_2 (S_z). The work of Breecker et al. (2009, 2010) suggests the use of a standard value (2500 ppmV) for paleo-reconstructions; however, measurements of modern S_z values suggest that this value can be highly variable (Retallack, 2009; Breecker, 2010; Cotton and Sheldon, 2012) and, due to its importance in pCO_2 paleobarometer calculations, should be accounted for in any pCO_2 estimates (Retallack, 2009). Therefore, we have chosen to estimate S_z for each individual paleosol based on the relationship shown by Cotton and Sheldon (2012), instead of standardizing across different paleosol types as suggested by the work of Breecker et al. (2009, 2010).

2.3 RESULTS

2.3.1 Pedotype description

Pedogenic alteration and subsequent burial of fluvial sediments from the margin of the Green River/Great Divide Basin has resulted in the preservation of many distinctive paleosol characteristics, including horizonation and color changes, organic root traces, rhizoliths, rhizohaloes, carbonate nodules, ped structures, and ichnofossils (Figure 2.2). In both stratigraphic sections, the same six pedotypes (Table 2.1) were identified based on these specific criteria (e.g. Kraus, 1999), and the features were conserved as a definable assemblage through time.

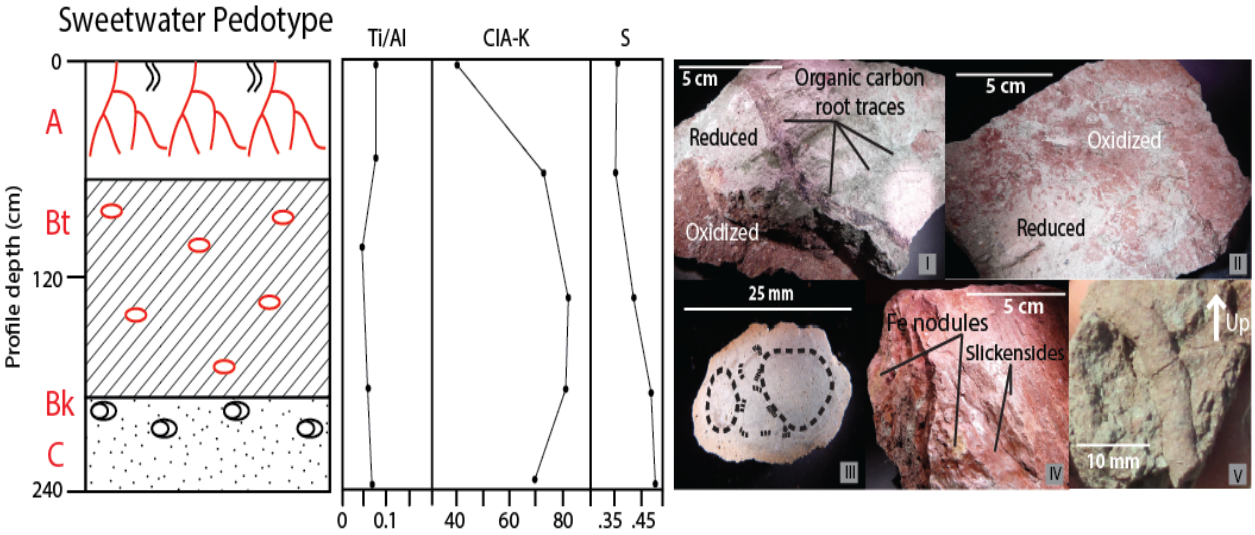

Figure 2.2 Sweetwater pedotype exemplar profile depicts stylized features seen in samples from different paleosols of this pedotype: I. carbonaceous and chemically reduced root traces, II. redoximorphic mottling, III. composite carbonate nodule, IV. ped boundary slickensides and reduced iron nodules, and V. vertical burrows. This pedotype is an Alfisol-type soil with a Bt horizon enriched in clays and bases (CIA-K and S). These sections also contain deep carbonate-bearing horizons in some cases, and all analyzed profiles exhibit a stable source of clastic material (Ti/Al ratio).

These pedotypes can be further collapsed into three principal paleosol types based on the taxonomic classification schemes of the USDA (Soil Survey Staff, 1999) and the paleosol-specific scheme of Mack et al. (1993): the Honeycomb pedotype, an Alfisol (calcisol) defined by

moderate development and the presence of calcic horizons (Bk); the Sweetwater pedotype, an Alfisol (argillisol) defined by significant development and gleyed features; and the Killpecker pedotype, an Inceptisol (protosol) defined by minimal development but also by a lack of original sedimentary features that would be found in an Entisol (c.f., Retallack, 2012). The name of each pedotype has been chosen based on local landmark names. While all of the principal paleosol types were represented throughout both sections, their distribution is neither proportional between sections nor constant through time (Table 2.1). The Killpecker pedotype is significantly more common at site HB1, indicating that the section is more proximal to a fluvial distributary system (Kraus, 1999; Hamer et al., 2007), an interpretation that is confirmed by the presence of more common channel deposits at this site as well (Figure 2.3). The other two principal types are roughly consistent between sites HB1 and HB2, but the Sweetwater pedotype is significantly more common during the central interval of both stratigraphic sections (Figure 2.3).

2.3.2 Pedogenesis

Material in these stratigraphic sections was sourced entirely from fluvial processes, as exhibited by common coarse-grained channel and crevasse splay sandstone deposits and stratigraphically adjacent distal fluvial deposits composed of siltstones and mudstones. Channels and splays were indicated by significant and laterally discontinuous erosive surfaces (0.2–5 m) filled with coarse sand and depositional features like progressive lateral point bar deposition and trough cross-bedding. These deposits show little to no evidence of pedogenesis, while nearly all distal siltstone and mudstone deposits show at least minor pedogenic alteration. Pedogenic alteration of these distal sediments is evident in both field observations (color, bioturbation, textural variation/horizonation, ped structures) and in geochemical analyses (authigenic clays, elemental profiles; Figure 2.2).

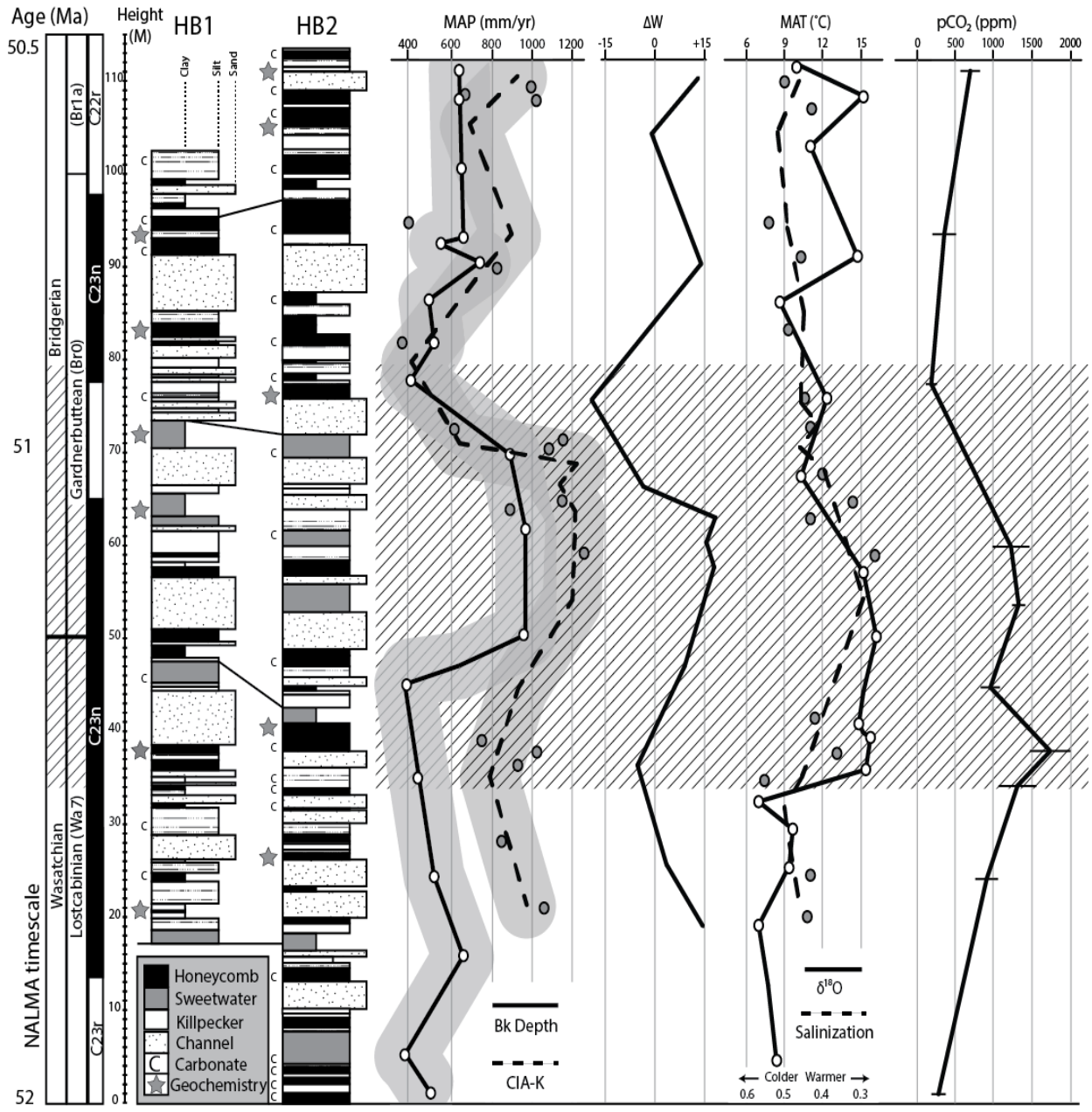

Figure 2.3 Integrated stratigraphic data from sites HB1 and HB2 tied to the GPTS and NALMA timescales as in Clyde et al. (2001) and Smith et al. (2008). Climatic proxies include samples from both sites, indicated by "Carbonate" and "Geochemistry" markers. ΔW is a proxy for weathering rate over time, where positive numbers indicate and increase in weathering rate. Envelopes around MAP curves indicate associated error, horizontal bars on pCO_2 indicate error for individual estimates, and error for MAT estimate is not shown (see text). Shaded box delineates our "peak interval" associated with the EECO.

The major defining pedogenic features of these sediments are root traces, carbonate nodules, and mottling/gleyed zones. Root traces are preserved as drab haloes (rhizohaloes) and carbonaceous traces, and are predominantly fine (5–10 mm) and both shallowly and deeply penetrating, indicating variable soil development and probably, a fluctuating water table (e.g., Kraus and Hasiotis, 2006). The depth to the Bt horizon in the more developed Alfisol-like pedotypes (Honeycomb and Sweetwater) is closely related to the point of maximum depth of rooting, which agrees with work indicating deeper Bt horizons forming under forest vegetation (Runge, 1973). Carbonate is discretely preserved in 0.5–4.5 cm diameter nodules, and forms distinct and continuous horizons (Bk) at depths from 35–230 cm (average depth of 85 cm) below the surface in many paleosols, and particularly in the Honeycomb pedotype. Most Bk horizons are between 10 and 60 cm thick (average thickness of 30 cm), and depth measurements are taken from the top of the rooting horizon, making them a minimum estimate due to the potential for erosive truncation of the profile. Paleosols that had clear evidence for erosive truncation were excluded. Mottling or gleying of the Bt horizon is common in the Sweetwater pedotype, and often occurred along with concretions of reduced iron, indicating poor drainage and/or significant floodplain saturation (c.f., Sheldon, 2005).

The characteristics and degree of alteration allow for the division of pedotypes and construction of a theoretical paleoenvironment (Table 2.1). The variability in sedimentary facies (channel proximal to distal) across the paleocatena results in slight changes in pedotype on lateral transects, however in most cases pedotype and pedogenic features are conserved across significant distances (~km scale), including between sections. This, in addition to the frequency of well-developed forest paleosols (Honeycomb and Sweetwater Alfisol pedotypes), indicates a stable floodplain environment (Kraus, 1999; Hamer et al., 2007). The stability of the

environment can also be confirmed by an empirically derived soil age function (T_f, in years) based upon the thickness (cm) of eluvial horizons (T_{Bt}):

$$T_f = 17.07(T_{Bt})^2 + 645.8(T_{Bt})$$

(No error function, $R^2 = 0.87$; Sheldon, 2003). (2.6)

The thickness of argillic/eluvial horizons can be affected by factors related both to climate and parent material, and this function has unknown error parameters due to the potential for the erosive truncation of paleosols on long timescales. Nonetheless, results indicate long formation times for both major Alfisol pedotypes (Table 2.1), especially the Sweetwater pedotype, which confirms the long-term stability of environmental conditions. In addition, lateral sampling of paleosols throughout the HB sections (Appendix A2) shows similar degrees of development and stable geochemical conditions through individual soil horizons, indicating that paleosol-based measurements are internally consistent and robust for environmental reconstruction purposes.

2.3.3 Paleosol diagenesis and complications

The primary complication to paleosol proxy interpretations is burial compaction. Based on local structural and stratigraphic relationships (Roehler, 1992; Smith 2008), the overlying sediment load on these paleosols is generally less than 1.2 km, which is minimal in terms of potential paleosol compaction. Ichnofossils display little evidence of compaction (Figure 2.2), and any changes in horizon depths and thicknesses caused by this loading have been accounted for by using the decompaction equations of Sheldon and Retallack (2001). While physical and chemical diagenesis can often be of concern for interpreting paleosols, our sections show little evidence of alteration. Many of the paleosols contain well-preserved original carbonaceous material like (sometimes branching) root traces and charcoal, indicating a lack of post-burial oxidation (Retallack, 2001b). Diagenetic alteration of the paleosols is also minimal, as indicated

by a dearth of post-burial salt precipitation or other diagenetic minerals, as well as geochemical depth profiles comparable to modern soils (Maynard, 1992). Comparisons of provenance were conducted both through time (throughout the stratigraphic section) and across the paleocatena (horizontal transects) using the Ti/Al ratios of Bt horizons (n = 16). This is based on the conservative nature of both elements within a paleosol profile (Sheldon, 2006), and the fact that Ti content is highly variable between sources, while Al content is relatively constant (Li, 2000). Our data indicate a single constant source of clastic material on both temporal and spatial timescales, and show no evidence of the chemical or physical removal of Ti or Al (Figure 2.2; e.g., Sheldon, 2006).

2.3.4 Weathering

Relative changes in chemical weathering, as indicated by ΔW, ranged from -41 to 15 (average value = 0 by definition, $\sigma = 16$). After smoothing from a three-point running average, they display the distinct trend of a rapid shift to higher values (relative increase in overall chemical weathering) followed by a gradual and fluctuating decline (relative decrease in overall chemical weathering). This change in weathering regime to a period of increased chemical weathering occurs at ~51.4 Mya, remaining elevated for about 0.5 Ma before transitioning to relatively lower rates of weathering for the rest of the studied section (Figure 2.3).

2.3.5 Paleoprecipitation

Paleoprecipitation was estimated both from depth to carbonate-bearing (Bk) horizons and from geochemical climofunctions derived from elemental ratios in the eluvial (Bt) horizons of paleosols (e.g., Sheldon and Tabor, 2009). Our data indicate a close correlation between these two proxies, with mean annual precipitation (MAP) values for this time period between 362–1105 mm yr^{-1}, which falls within the range of a semi-arid to sub-humid precipitation regime

(mean = 853 mm yr^{-1}, σ = 232 mm yr^{-1}). Ample physical evidence for both ends of this range in mean annual precipitation exist in the section, with thin paleosols and significant shallow carbonate deposition in some profiles (low MAP), and thick eluvial horizons and saturation features like iron nodules in others (high MAP). Despite the wide range in MAP values throughout the section, the values show very consistent trends in both proxy systems, which was tested by analyzing the linear relationship between residuals for each trend (R^2 = 0.79). The trends show a rapid increase to high MAP values (>1000 mm yr^{-1}) over a peak interval from 51.4–50.9 Mya, and a gradual decline back toward original semi-arid conditions (Figure 2.3). This peak interval of precipitation is also coincident with the significant increase in relative long-term weathering values (ΔW; Figure 2.3).

2.3.6 Paleotemperature

Temperature estimates from $\delta^{18}O$ values have a range between ~8-16°C, and a mean of 12.0°C (σ= 3.1°C). Salinization values range from 0.32 to 0.54, with a mean of 0.42 (σ= 0.06), and were trend-fit to a temperature scale with warm-cool axes (Figure 2.3). When plotted together, results for both MAT proxy trends exhibit the same basic shape as MAP, despite a somewhat weaker statistical relationship (R^2 = 0.55): stable initial temperatures are interrupted by a rapid warming event (~7–8°C in the $\delta^{18}O$ record) between 51.5 and 50.9 Mya, or slightly preceding the rapid trend evident in MAP values (Figure 2.3), followed by a gradual decline to original values. Though uncertainty in both temperature proxies makes exact temperature ranges like those quoted above ambiguous, the consistency between our datasets and the demonstrated applicability of both of these proxy techniques as trending tools indicates that throughout these integrated stratigraphic sections there existed a temperate climate regime that was interrupted by a significant and short-term hyperthermal event.

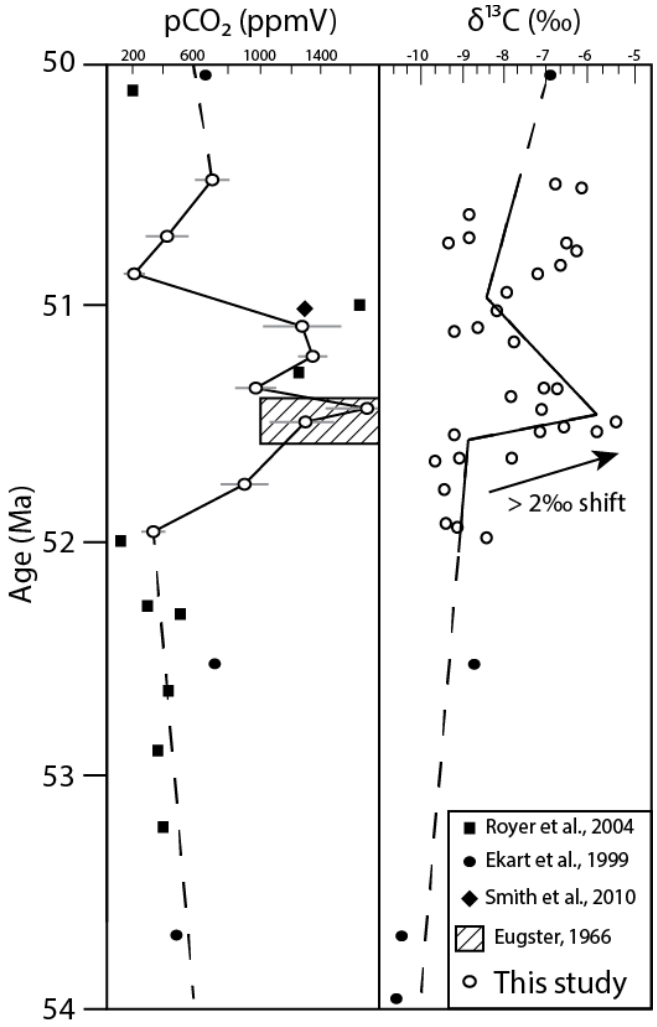

Figure 2.4 pCO_2 and $\delta^{13}C_{carb}$ records of the EECO. Horizontal gray bars indicate error associated with pCO_2 estimates from this study. Dashed lines are extrapolated curves between our data and published datasets cited above.

2.3.7 Paleobarometry

Our pCO_2 estimates range from 198–1696 ppmV, with a mean value of 878 ppmV (σ = 495 ppmV). Error for these calculated values ranged from 58–284 ppmV, with a mean error of 155 ppmV, and neither calculated pCO_2 values nor $\delta^{13}C$ composition was correlated with sample $CaCO_3$ content. These data show a rapid increase (roughly 3–5×) coincident with the increase in MAT around 51.5 Mya (Figure 2.3). This was followed by a period of stable higher values (≥1200 ppmV) that lasted for ~0.5 Ma before a rapid halving and stabilization above original

pCO_2 values (near double Present pCO_2 concentrations). This period of high pCO_2 values is broadly contemporaneous with the interval of high MAT and MAP, and its initiation is also marked by a rapid increase of ~3‰ in the $\delta^{13}C$ composition of the analyzed pedogenic carbonates (Figure 2.4). Overall, $\delta^{13}C_{carb}$ composition ranged from -5.43‰ to -9.34‰, with a mean value of -7.66‰ (σ= 1.17‰), and except for the major excursion at 51.5 Mya, was generally stable with a slight trend toward more positive values over time.

2.3.8 Organic material

$\delta^{13}C_{org}$ values from occluded or preserved organic matter ranged from -10.22‰ to -25.62‰ with a mean value of -22.33‰ (σ= 2.6‰). $\Delta^{13}C$ values ($\delta^{13}C_{org} - \delta^{13}C_{carb}$) ranged from 4.93 to 17.93, with a mean value of 14.96 (σ= 2.9). Major outliers (i.e., isotopically heavy values inconsistent with C_3 photosynthesis) were reproducible and confined to a limited number of paleosol profiles, and are considered further below. The $\Delta^{13}C$ data display no trends through time (Figure 2.5), indicating a stable relationship between the $\delta^{13}C$ composition of organic matter and pedogenic carbonates in the same soil profile.

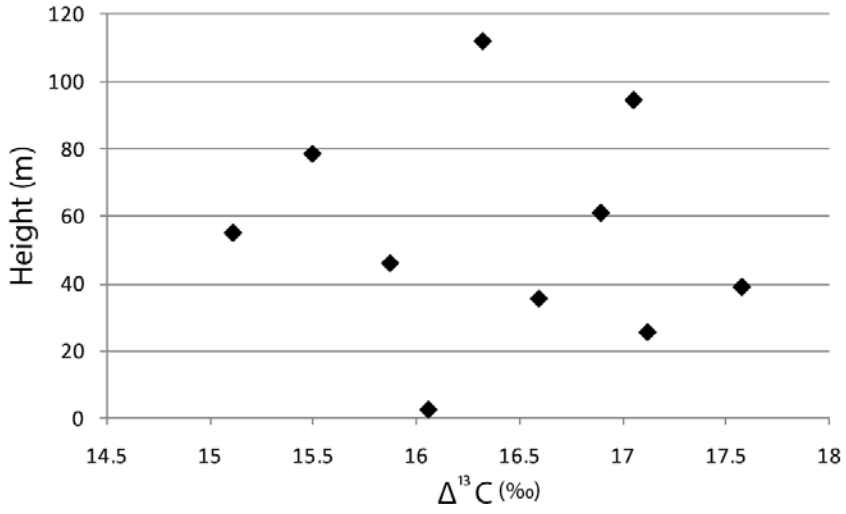

Figure 2.5 $\Delta^{13}C$ ($\delta^{13}C_{org} - \delta^{13}C_{carb}$) for samples used in atmospheric pCO_2 reconstructions plotted by stratigraphic height in combined sections HB1 and HB2.

2.4 DISCUSSION

2.4.1 EECO

2.4.1.1 Record synchroneity

Previous work on the Early Eocene Climatic Optimum has described the period as a gradual trend of increasing atmospheric pCO_2 with consequent rises in global mean annual temperature (~ 4°C) and mean annual precipitation (e.g., Zachos et al., 2008). Overall, the integrated regional dataset from the Green River/Great Divide Basin is in agreement with the magnitudes and types of change previously defined within the EECO. This environmental reconstruction, which interprets the area as a fluvial, basin-margin system dominated by Alfisol-type forest soils, is significantly different from the modern environment of the basin (Aridisol-dominated, and primarily non-vegetated), but is consistent with other environmental interpretations of this region (Clyde et al., 2001) and surrounding basins (e.g., Roehler, 1993) during the Eocene. The data also indicates consistency across the landscape in terms of the both the fluvial sedimentary processes and the pedogenic conditions that prevailed at any given time. The distinct change in soil-forming processes through the peak interval, as demonstrated by the increased frequency in the Sweetwater pedotype and rapid increase in long-term weathering trends, is indicative of environmental response to a major climatic change like rapid increases in MAT and MAP (Jenny, 1941; Kraus, 1999).

Many of these paleoclimatic records come from multiple-proxy systems, so reconciling their differences internally using residuals analysis on trended data and comparing them to external records is an important aspect of understanding their implications. The robustness of trends from multiple-proxy systems was confirmed by residuals analysis (Figure 2.6), which involved calculating the residual value of each individual estimate (e.g., MAT, MAP) relative to

the mean value for all estimates from that proxy system, and plotting the residuals from each system versus one another (Figure 2.6). Residuals from both MAT and MAP trends exhibited strong correlations ($R^2 = 0.55$, $R^2 = 0.79$, respectively), indicating that the multiple-proxy systems are internally consistent and that the trends through time are robust. The synchroneity of changes between different types of climatic records was also tested, which confirms the link between increasing atmospheric pCO_2 and temperature ($R^2 = 0.56$; Figure 2.6) and indicates that within the resolution of this record, changes are broadly synchronous.

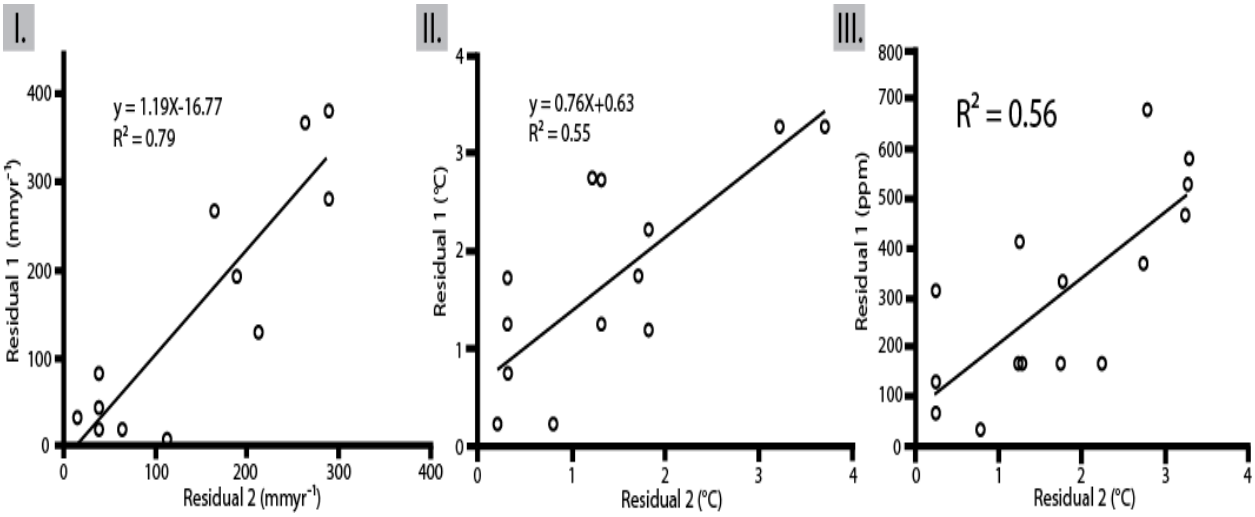

Figure 2.6 Plots of residuals analyses on data trends for: I. depth to Bk horizon and CIA-K mean annual precipitation proxies (MAP; mmyr-1), II. salinization and $\delta^{18}O$ mean annual temperature proxies (MAT; °C), and III. atmospheric pCO2 (ppmV) and MAT proxies. Note the relationships in plots I. and II. are nearly 1:1 and have strong correlations, as do CO_2 and temperature in plot III.

2.4.1.2 Paleotemperature

Based on the work of Sheldon (2009), it was assumed that temperature estimates from geochemical climofunctions (*S*) provide a vector of change, as the higher precipitation values and longer formation times of soils from our sections likely decrease total soil salinization, resulting in temperature estimates that are lower than actual MAT values but are still comparable

relative to each other. Therefore, trends from these data rather than calculated temperatures (e.g., Sheldon et al., 2002) were used as an internal check on temperature estimates from $\delta^{18}O$ thermometry functions, which are more likely accurate in terms of a quantitative value, but are susceptible to trend exaggeration from changes in soil moisture sources (Sheldon and Tabor, 2009). Both temperature estimates indicate similar trends and values as confirmed by residuals analysis ($R^2 = 0.55$), allowing for the construction of a combined record that is representative of the EECO (Figure 2.3).

Local records from elsewhere in the Green River Basin (Greenwood and Wing, 1995; MAT = 14–16˚C) are in agreement with this isotopic temperature record of the EECO, as are records of global sea-surface-temperature (Ivany et al., 2008). Despite agreement between all of these records on the range of EECO temperatures, other reconstructions do not show the same rapidity or magnitude of rise in MAT that the Green River Basin record does. Modeling estimates based on CO_2 reconstructions and regional climate model (RCM) parameters provide similarly paced rises, but also result in significantly higher mean annual temperature estimates (Thrasher and Sloan, 2009). Given that this record is higher-resolution than other empirical studies of regional paleotemperature in the basin, it is likely that these values are the best representation of the timescale involved in this shift to higher MAT during the EECO in continental settings. Marine records also show differences in terms of the magnitude of temperature shifts through the EECO (~4°C rise), though this can most likely be attributed to variation between marine and continental system responses. Terrestrial records typically exhibit larger-magnitude temperature responses to climatic change than marine records due to the effect of continentality (Retallack, 2007) and tectonically-controlled differences in atmospheric circulation patterns (Sheldon and Retallack, 2004).

2.4.1.3 Paleoprecipitation

Precipitation estimates were also based on multiple proxies: depth to Bk horizon, and geochemical climofunctions (*CIA-K*). As was the case with temperature estimates, one of the proxies (depth to Bk horizon) is used as a minimum value (due to possible profile truncation and unaccounted-for compaction), and compared to the other for pattern matching purposes. As shown in Figure 2.6, both precipitation estimates display a consistent trend and roughly similar values ($R^2 = 0.79$; Figure 2.6), both of which are in agreement with estimated MAP from EECO sites at similar paleolatitudes (Krause et al., 2010), and with modeling predictions from RCMs of western North America (Thrasher and Sloan, 2010). This shift is evident slightly after (≤0.1 Ma) the rise in MAT, which follows logically from the feedback between increased temperatures, resulting in increased evaporation in a large endorheic system like Lake Gosiute, and increases in regional precipitation (e.g., Thrasher and Sloan, 2010).

2.4.1.4 Paleobarometry

Estimates of atmospheric pCO_2 for the EECO itself are scarce, as major records from pedogenic carbonates (Ekart et al., 1999), stomatal indices (Royer et al., 2004), and combined proxy records (Zachos et al., 2008; Beerling and Royer, 2011) provide broad trends across the Eocene without measurements directly from the EECO event. Other studies contain limited or highly volatile EECO datasets from evaporate minerals like nahcolite (Eugster, 1966), marine boron (DeMicco et al., 2003), and stomatal indices (Smith et al., 2010) that indicate elevated pCO_2 spikes, but no full reconstructions exist of CO_2 concentrations throughout the event. The data presented here have important implications for both types of reconstructions, as the results appear to connect these records in a coherent fashion. Low pCO_2 values (<500 ppmV) from before the peak interval correspond well to the “near-present” levels reported by DeMicco et al.

(2003) and Royer et al. (2004) for the pre-EECO early Eocene. Additionally, values from within the peak interval, which are contemporaneous with sites discussed in Eugster (1966), Royer et al. (2004), and Smith et al. (2010), also correspond well to these reported high values (≥1200 ppmV) for that time period (Figure 2.4). While the magnitudes of change and the overall trends (increase to roughly 3–5× pCO_2 during the EECO and significant decrease afterward) seen in combined records like Zachos et al. (2008) and Beerling and Royer (2011) fit well with these reported values, the reported timescale of this change displays a distinct contrast. Instead of the gradual change in concentration interpreted in temporally coarser records (e.g., Ekart et al., 1999; Zachos et al., 2008), we show with high-resolution sampling that the increase in atmospheric pCO_2 during the EECO occurred rapidly in concert with increasing MAT (Figure 2.5), and remained at stable high values (≥1200 ppmV) for a limited period of time (~0.5 Ma).

2.4.2 Carbon sources and magnitude of change

The rapid increase in atmospheric pCO_2 also corresponds to the timing of a >2‰ shift in $\delta^{13}C$ in the pedogenic carbonate records (Figure 2.4), which is consistent with other pedogenic carbonate records for the period (Ekart et al., 1999), but disagrees with broad marine trends for the same period (Zachos et al., 2001). Non-phase shifts of this kind have been attributed to major drying events in the pedogenic carbonate record (e.g., Kraus and Riggins, 2006), but in this case we interpret the signal as being due to changes in pCO_2 because of the contemporaneous shift to a wetter precipitation regime recorded by multiple proxies (which should have an effect on $\delta^{13}C$ compositions that is opposite of the observed trend). Marine records from other major climatic events like the PETM (Zachos et al., 2003), ETM 1 and 2 (Stap et al., 2010), and later Eocene events (Sexton et al., 2011) show negative isotopic excursions coincident with high atmospheric

pCO_2 values, but in each case these are tied to major oceanic/atmospheric inputs from sources of highly depleted carbon (e.g., methane hydrates, -60‰; terrestrial carbon, -27‰).

The reported positive shift in the terrestrial record of $\delta^{13}C$ (Figure 2.4) simply indicates a different carbon source, and this decoupling of the terrestrial and marine records can be explained by the basic observation that these two records inherently respond to different conditions. The marine $\delta^{13}C$ record is controlled primarily by carbon burial in the ocean, so a negative excursion indicates a decrease in the burial of organic carbon in the ocean (Zachos et al., 2001). Alternatively, the terrestrial $\delta^{13}C$ record responds to either changes in vegetation type (post-Oligocene; Fox and Koch, 2004), or to changes in atmospheric pCO_2 or atmospheric $\delta^{13}C$ composition (Ekart et al., 1999). Based upon benthic foraminifera, Tipple et al. (2010) found a minor shift (+0.5‰) in the $\delta^{13}C_{atm}$ value atmospheric composition from 52–50 Mya. At the same time, this record shows essentially constant $\Delta^{13}C$ values throughout the interval (Figure 2.5), which indicates no significant change in the source of the carbon being utilized by plants (i.e., not isotopically light CO_2 derived from methane hydrates), nor any post-burial alteration, which could also change the $\delta^{13}C_{carb}$ versus $\delta^{13}C_{org}$ relationship. Instead, these data indicate that the positive shift in the terrestrial record is due to increased atmospheric pCO_2 (Cerling, 1992), a conclusion that is consistent with decreased carbon burial in oceanic reservoirs causing negative excursions in the marine record (see below).

All of these data indicate a peak interval of major climatic and environmental change between roughly 51.5 and 50.9 Mya that is consistent with descriptions of Early Eocene Climatic Optimum maxima. As detailed in Figure 2.3, these interpretations match other major records (e.g., Zachos et al., 2001; 2008) in terms of the magnitude and types of global climatic change in response to increased atmospheric pCO_2, but highlight a previously undocumented peak interval

of terrestrial changes during the broader scale EECO event. Based on the peak interval, local changes in MAT and MAP within the EECO appear to be analogous to those of transient events like the Paleocene-Eocene Thermal Maximum (PETM) or other Eocene hyperthermals, in that the events are of similar magnitude and appear to initiate rapidly (<0.1 Ma), with a relatively short (~0.5 Ma) recovery period (e.g., Zachos et al., 2008; Sexton et al., 2011). This has significant implications for understanding the causes of the high CO_2 levels that led to these major climatic changes, as the long-term forcings ascribed to current records of the EECO, such as variations in silicate weathering (Zachos et al., 2008), are likely inconsistent with the rapid timescales of terrestrial change exhibited in our integrated reconstruction of EECO maxima.

The trends of a rapid increase in atmospheric pCO_2 and a concurrent positive shift in $\delta^{13}C_{atm}$ and $\delta^{13}C_{carb}$ compositions, both supported by independent relationships, instead suggest a sizable (non-depleted) source of carbon entering the atmosphere on a relatively short timescale. This is easily accommodated by the above description of the marine carbon record; increased atmospheric pCO_2 across this interval (Figures 2.3 and 2.4) likely resulted from the oxidation of a portion of the marine carbon reservoir, leading to decreased carbon burial in the ocean. A recently published explanation of later Eocene hyperthermal events is consistent with this possibility; Sexton et al. (2011) suggest that increased ventilation of the deep ocean would provide the significant addition of a heavy (~0‰) source of carbon (CO_2) to the atmosphere. Removal of relatively heavy carbon from the ocean via deep ocean ventilation would result in more depleted foraminiferal values (negative $\delta^{13}C$; Zachos et al., 2001) because the remaining marine reservoir would be depleted relative to its initial composition, while simultaneously resulting in a slightly heavier atmospheric $\delta^{13}C$ value and isotopically heavier paleosol carbonates, because the starting composition of the atmospheric $\delta^{13}C$ reservoir would have been

light (~-6‰; Tipple and Pagani, 2010) relative to the new carbon ventilated from the deep ocean (~0‰). In order to produce such a change in the marine and terrestrial carbon $\delta^{13}C$ records, the oxidation of dissolved carbon on the order of ~1000–2000 Gt would be necessary (c.f., Sexton et al., 2011), which concurs with the magnitude of change for the modeled increase in atmospheric pCO_2 (Figures 2.3 and 2.4). Therefore, the marine and continental isotopic records are complementary rather than in opposition, and support the same mechanism of change.

Additionally, this integrated high-resolution temperature and atmospheric pCO_2 record allows for important conclusions about temperature-CO_2 sensitivities. The sensitivity demonstrated by this record, a maximum MAT increase of roughly 2.8°C per doubling of atmospheric pCO_2, fits the moderate projections made by the IPCC (2007). This is a maximum value for sensitivity, as changes in $\delta^{18}O$ value associated with temperature may be exaggerated by changes in $\delta^{18}O$ source values as a response to orography; nonetheless, these calculations fit predictions for modern temperature-CO_2 sensitivities. This has significant implications for estimating future climate change, as it suggests that high-resolution records from paleosols that couple temperature and pCO_2 measurements are an excellent tool for constraining the potential range of temperatures we may face in coming centuries as a result of continued increases in atmospheric pCO_2.

The timing of the peak interval also has important ecological implications; in contrast with other records of the EECO (e.g., Zachos et al., 2008), the initiation of major climatic and environmental changes associated with the peak interval corresponds to a major faunal boundary in the North American Land Mammal Age (NALMA) timescale. The transition from the Wasatchian to the Bridgerian faunas is one of the most significant turnover events of the Cenozoic, and occurs at 51.3 Mya (Alroy, 2000; Zonneveld et al., 2000), slightly after the

beginning of the peak interval we have defined within the broader EECO (Figure 2.3). The turnover event duration also fits well with the peak interval, as faunal changes are mostly restricted to a period of <0.5 Ma (Alroy, 2000). The close relationship between independently verified terrestrial climatic change and terrestrial ecological turnover and their temporal decoupling from published marine records lends support to the idea that terrestrial changes during the EECO event may be characterized by a more rapid, transient maximum.

2.4.3 Further work

This new terrestrial record of the EECO is crucial for both describing the event itself and linking the potential causes and feedbacks involved in its evolution. Terrestrial records are a more direct source for climatic and environmental information; however, few high-resolution climatic records of the EECO exist beyond this work. To improve our understanding of the EECO in its entirety and allow for regional comparisons of responses to the event, a more robust global record is needed from paleosols on multiple continents. Generating higher resolution climatic data will also be important to this understanding, as current data for the EECO is limited to resolution on a ~10^5 timescale, whereas similar records from the PETM have been resolved to a much finer degree.

Paleosols can also directly provide a basic record of ecological changes as a result of climatic events like the EECO, and in some cases can record high-resolution changes via the preservation of organic carbon ($\delta^{13}C$ composition) and phytoliths from bulk samples. Two heavy $\delta^{13}C$ isotopic values (average ≈ -10.6‰) were reproduced in triplicate from organic samples within limited paleosol profiles from our sections, and correspond to similarly heavy isotopic values from pedogenic carbonates reported by Clyde et al. (2001), which indicates the possibility of fractionation caused by the presence of C_4 vegetation. In this case, because C_4 grasses had not

yet evolved (Edwards et al., 2010), C_4 sedges or herbaceous dicots at a stream or lake margin are more likely to be responsible for the anomalous isotopic results (Sage, 2004). However, both the anomalous heavy $\delta^{13}C_{org}$ and $\delta^{13}C_{carb}$ datasets are incompatible with our overall $\delta^{13}C_{org}$ record and with preliminary phytolith results (i.e., no diagnostic phytoliths from C_4 plants; Hyland, unpublished data), which are primarily consistent with either "normal" ($\delta^{13}C_{org}$ from -22‰ to -34‰) or water-stressed C_3 photosynthesis (+2–3‰ relative to "normal" values) ranges, as reconstructed from estimates of Eocene atmospheric $\delta^{13}C$ values (i.e., Tipple et al., 2010). Thus, two possible explanations arise: 1) modern contamination, 2) transient C_4 vegetation patchiness. The first possibility can be discounted because while pedogenic carbonates are relatively easy to diagenetically alter, organic matter is not, requiring much higher temperatures (e.g., Sheldon and Tabor, 2009) for which there is no other evidence in our records. Further work is needed to verify explanation (2), such as finding similar results at other penecontemporaneous localities in Wyoming or elsewhere, but we tentatively accept the conclusion of Clyde et al. (2001) that plants using C_4 photosynthesis were likely present in limited amounts during the EECO in Wyoming on the basis of two types of carbon isotopic data.

2.5 CONCLUSIONS

During the early Eocene, including the EECO, the Green River/Great Divide region and likely much of the margin of paleolake Gosiute was a stable, fluvially-controlled floodplain environment. These floodplains show evidence of large scale continuous soil development, distinct horizonation, and features comparable primarily to modern Alfisols. Individual paleosols exhibit some spatial heterogeneity in terms of pedological features; however, paleosol types appear to conserve broadly both physical and geochemical characteristics over space and

time. Regional climate during this time period can be characterized as warm-temperate and semi-arid to sub-humid, with a peak interval of about 0.5 Ma that exhibits warmer (~7˚C) and significantly wetter (~750 mm yr^{-1}) conditions and that resulted in major changes in the local weathering regime. A rapid 3–5× increase to high atmospheric pCO_2 values (>1500 ppmV), and a shift in the $\delta^{13}C$ composition of pedogenic carbonates while $\Delta^{13}C$ values remained constant, appears to define and provide a cause for this peak interval of major regional climatic change, suggesting that the broad-scale EECO may contain a shorter-term and more aberrant hyperthermal "maximum" than previously documented in marine records, which reconstruct a ~4°C temperature change over 2 Ma. More work should and will be done to constrain further the environmental, climatic, and ecological conditions of the Early Eocene Climatic Optimum and the dynamics of basin-margin systems like the Green River/Great Divide region. Additional records of this sort may help constrain the dynamics of future climate change by providing examples of somewhat poorly understood climatic factors such as temperature-CO_2 sensitivities.

REFERENCES CITED

Alroy, J., 2000. New methods for quantifying macroevolutionary patterns and processes. Paleobiology 26, 707–733.

Beerling, D.J., Royer, D.L., 2011. Convergent Cenozoic CO_2 history. Nature Geoscience 4, 418–420.

Berner, R.A., Kothavala, Z., 2001. GEOCARB III: A revised model of atmospheric CO_2 over Phanerozoic time. American Journal of Science 310, 182–204.

Breecker, D.O., Sharp, Z.D., McFadden, L.D., 2009. Seasonal bias in the formation and stable isotopic composition of pedogenic carbonate in modern soils from central New Mexico, USA. Geological Society of America Bulletin 121, 630–640.

Breecker, D.O., Sharp, Z.D., McFadden, L.D., 2010. Atmospheric CO_2 concentrations during ancient greenhouse climates were similar to those predicted for A.D. 2100. Proceedings of the National Academy of Sciences of the United States of America 107, 576–580.

Cerling, T.E., 1991. Carbon dioxide in the atmosphere: Evidence from Cenozoic and Mesozoic paleosols. American Journal of Science 291, 377–400.

Cerling, T.E., 1992. Use of carbon isotopes in paleosols as an indicator of the pCO_2 of the paleoatmosphere. Global Biogeochemical Cycles 6, 307–314.

Cerling, T.E., Quade, J., 1993. Stable carbon and oxygen isotopes in soil carbonates. In: McKenzie, J.A., Savin, S. (Eds), Climate Change in Continental Isotopic Records. Geophysics Monograph, American Geophysical Union, Washington DC, 217–231.

Clyde, W.C., Sheldon, N.D., Koch, P.L., Gunnell, G.F., Bartels, W.S., 2001. Linking the Wasatchian/Bridgerian boundary to the Cenozoic Global Climate Optimum: new magnetostratigraphic and isotopic results from South Pass, Wyoming. Palaeogeography, Palaeoclimatology, Palaeoecology 167, 175–199.

Cotton, J.M., Sheldon, N.D., 2012. New constraints on using paleosols to reconstruct atmospheric pCO_2. Geological Society of America Bulletin 124, 1411–1423.

DeMicco, R.V., Lowenstein, T.K., Hardie, L.A., 2003. Atmospheric pCO_2 since 60 Ma from records of seawater pH, calcium, and primary carbonate mineralogy. Geology 31, 793–796.

Driese, S.G., Ober, E.G., 2005. Paleopedologic and paleohydrologic records Precipitation Seasonality from Early Pennsylvanian “Underclay” paleosols, U.S.A. Journal of Sedimentary Research 75, 997–1010.

Dworkin, S.I., Nordt, L., Atchley, S., 2005. Determining terrestrial paleotemperatures using the oxygen isotopic composition of pedogenic carbonate. Earth and Planetary Science Letters 237, 56–68.

Edwards, E.J., Osborne, C.P., Strömberg, C.A.E., Smith, S.A., C_4 Grasses Consortium, 2010. The origin of C_4 grasslands: integrating evolutionary and ecosystem science. Science 328, 587–591.

Ekart, D.D., Cerling, T.E., Montanez, I.P., Tabor, N.J., 1999. A 400 million year carbon isotope record of pedogenic carbonate: Implications for paleoatmospheric carbon dioxide. American Journal of Science 299, 805–827.

Eugster, H.P., 1966. Sodium carbonate-bicarbonate minerals as indicators of pCO_2. Journal of Geophysical Research 71, 3369–3377.

Fox, D.L., Koch, P.L., 2004. Carbon and oxygen isotopic variability in Neogene paleosol carbonates: constraints on the evolution of the C_4 grasslands of the Great Plains, USA. Palaeogeography, Palaeoclimatology, Palaeoecology 207, 305–329.
Gradstein, F.M., Ogg, J.G., Smith, A.G., 2004. A Geologic Time Scale 2004. Cambridge University Press, Cambridge (UK), 610 pp.
Greenwood, D.R., Wing, S.L., 1995. Eocene continental climates and latitudinal temperature gradients. Geology 23, 1044–1048.
Hamer, J.M.M., Sheldon, N.D., Nichols, G.J., Collinson, M.E., 2007. Late Oligocene-Early Miocene paleosols of distal fluvial systems, Ebro Basin, Spain. Palaeogeography, Palaeoclimatology, Palaeoecology 247, 220–235.
Intergovernmental Panel on Climate Change, 2007. Fourth Assessment Report: Climate Change (AR4). Pachuari, R.K., and Reisinger, A. (Eds.), IPCC, Geneva, Switzerland, 104 pp.
Ivany, L.C., Lohmann, K.C., Hasiuk, F., Blake, D.B., Glass, A., Aronson, R.B., Moody, R.M, 2008. Eocene climate record of a high southern latitude continental shelf: Seymour Island, Antarctica. Geological Society of America Bulletin 120, 659–678.
Jenny, H., 1941. Factors of Soil Formation: A system of quantitative pedology. General Publishing Company, Toronto (ON), Canada, 191 pp.
Koch, P.L., 1998. Isotopic reconstruction of past continental environments. Annual Reviews of Earth and Planetary Sciences 26, 573–612.
Kraus, M.J., 1999. Paleosols in clastic sedimentary rocks: their geologic applications. Earth-Science Reviews 47, 41–70.
Kraus, M.J., Hasiotis, S.T., 2006. Significance of different modes of rhizolith preservation to interpreting paleoenvironmental and paleohydrologic settings: Examples from Paleogene paleosols, Bighorn Basin, Wyoming, USA. Journal of Sedimentary Research 76, 633–646.
Kraus, M.J., Riggins, S., 2007. Transient drying during the Paleocene–Eocene Thermal Maximum (PETM): analysis of paleosols in the Bighorn Basin, Wyoming. Palaeogeography, Palaeoclimatology, Palaeoecology 245, 444–461.
Krause, J.M., Bellosi, E.S., Raigemborn, M.S., 2010. Lateritized tephric paleosols from Central Patagonia, Argentina: a southern high-latitude archive of Paleogene global greenhouse conditions. Sedimentology 57, 1721–1749.
Li, Y.H., 2000. A Compendium of Geochemistry. Princeton University Press, Princeton (RI), 475 pp.
Mack, G.H., James, W.C., Monger, H.C., 1993. Classification of paleosols. Geological Society of America Bulletin 105, 129–136.
Maynard, J.B., 1992. Chemistry of modern soils as a guide to interpreting Precambrian paleosols. Journal of Geology 100, 279–289.
Nordt, L.C., Atchley, S., Dworkin, S.I., 2003. Terrestrial evidence for two greenhouse events in the latest Cretaceous. Geological Society of America Today 13, 4–9.
Nordt, L.C., Driese, S.D., 2010. New weathering index improves paleorainfall estimates from Vertisols. Geology 38, 407–410.
Pearson, P.N., Ditchfield, P.W., Singano, J., Harcourt-Brown, K.G., Nicholas, C.J., Olsson, R.K., Shackleton N.J., Hall, M.A., 2001. Warm tropical sea surface temperatures in the Late Cretaceous and Eocene epochs. Nature 413, 481–487.

Prochnow, S.J., Nordt, L., Atchley, S.C., Hudec, M.R., 2006. Multi-proxy paleosol evidence for middle and late Triassic climate trends in eastern Utah. Palaeogeography, Palaeoclimatology, Palaeoecology 232, 53–72.
Retallack, G.J., 1994. The environmental factor function approach to the interpretation of paleosols. In: Amundson, R., et al. (Eds.), Factors of Soil Formation: A fiftieth anniversary retrospective: Soil Science Society of America Publication 33, 31–64.
Retallack, G.J., 2000. Comment on Depth to pedogenic carbonate horizon as a paleoprecipitation indicator? Geology 28, 572.
Retallack, G.J., 2001a. A 300-million-year record of atmospheric carbon dioxide from fossil plant cuticle. Nature 411, 287–290.
Retallack, G.J., 2001b. Soils of the Past- An Introduction to Paleopedology. Blackwell Science Ltd., Oxford, UK, 404 pp.
Retallack, G.J., 2005. Pedogenic carbonate proxies for amount and seasonality of precipitation in paleosols. Geology 33, 333–336.
Retallack, G.J., 2007. Cenozoic paleoclimate on land in North America. Journal of Geology 115, 271–294.
Retallack, G.J., 2009. Refining a pedogenic-carbonate CO_2 paleobarometer to quantify a middle Miocene greenhouse spike. Palaeogeography, Palaeoclimatology, Palaeoecology 281, 57–65.
Retallack, G.J., 2012. Mallee model for mammal communities of the early Cenozoic and Mesozoic. Palaeogeography, Palaeoclimatology, Palaeoecology 342, 111–129.
Roehler, H.W., 1992. Introduction to greater Green River Basin geology, physiography, and history of investigations. U.S. Geological Survey Professional Paper 1506-A, 16 pp.
Roehler, H.W., 1993. Eocene climates, depositional environments, and geography, greater Green River Basin, Wyoming, Utah, and Colorado. U.S. Geological Survey Professional Paper 1506-F, 75 pp.
Romanek, C.S., Grossman, E.L., Morse, J.W., 1992. Carbon isotopic fractionation in synthetic aragonite and calcite: Effects of temperature and precipitation rate. Geochimica et Cosmochimica Acta 56, 419–430.
Royer, D.L., 1999. Depth to pedogenic carbonate horizon as a paleoprecipitation indicator? Geology 27, 1123–1126.
Royer, D.L., Berner, R.A., Montañez, I.A., Tabor, N.J., Beerling, D.J., 2004. CO_2 as a primary driver of Phanerozoic climate. GSA Today 14, 4–10.
Runge, E.C., 1973. Soil development sequences and energy models. Soil Science 115, 183–193.
Sage, R.F., 2004. The evolution of C_4 photosynthesis. New Phytologist 161, 341–370.
Scotese, C.R., 2000. Earth System History Geographic Information System, ArcView 3.2 v. 2.0C.
Sewall, J.O., Sloan, L.C., 2006. Come a little bit closer: A high-resolution climate study of the early Paleogene Laramide foreland. Geology 34, 81–84.
Sexton, P.F., Norris, R.D., Wilson, P.A., Palike, H., Westerhold, T., Rohl, U., Bolton, C.T., Gibbs, S., 2011. Eocene global warming events driven by ventilation of oceanic dissolved organic carbon. Nature 471, 349-353.
Sheldon, N.D., 2003. Pedogenesis and geochemical alteration of the Picture Gorge subgroup, Columbia River Basalt, Oregon. Geological Society of America Bulletin 115, 1377–1387.

Sheldon, N.D., 2005. Do red beds indicate paleoclimatic conditions? A Permian case study. Palaeogeography, Palaeoclimatology, Palaeoecology 228, 305–319.
Sheldon, N.D., 2006. Abrupt chemical weathering increase across the Permian-Triassic boundary. Palaeogeography, Palaeoclimatology, Palaeoecology 231, 315–321.
Sheldon, N.D., 2009. Non-marine records of climate change across the Eocene-Oligocene transition. In: Koeberl, C., Montanari, A. (Eds.), The Late Eocene Earth- Hothouse, Icehouse, and Impacts: Geological Society of America Special Paper 452, 241–248.
Sheldon, N.D., Retallack, G.J., 2001. Equation for compaction of paleosols due to burial. Geology 29, 247–250.
Sheldon, N.D., Retallack, G.J., 2004. Regional paleoprecipitation records from the Late Eocene and Oligocene of North America. Journal of Geology 112, 487–494.
Sheldon, N.D., Tabor, N.J., 2009. Quantitative paleoenvironmental and paleoclimatic reconstruction using paleosols. Earth-Science Reviews 95, 1–52.
Sheldon, N.D., Retallack, G.J., Tanaka, S., 2002. Geochemical climofunctions from North American soils and applications to paleosols across the Eocene-Oligocene boundary in Oregon. Journal of Geology 110, 687–696.
Sheldon, N.D., Costa, E., Cabrera, L., Garcés, M., 2012. Continental climatic and weathering response to the Eocene-Oligocene transition. Journal of Geology 120, 227–236.
Smith, M.E., Carroll, A.R., Singer, B.S., 2008. Synoptic reconstruction of a major ancient lake system: Eocene Green River, western United States. Geological Society of America Bulletin 120, 54–84.
Smith, R.Y., Greenwood, D.R., Basinger, J.F., 2010. Estimating paleoatmospheric pCO_2 during the EECO from stomatal frequency of Ginkgo, Okanagan Highlands, British Columbia, Canada. Palaeogeography, Palaeoclimatology, Palaeoecology 293, 120–131.
Soil Survey Staff, 1999. Keys to Soil Taxonomy: 8th Edition. Pocahontas Press, Blacksburg (VA), 600 pp.
Stap, L., Lourens, L.J., Thomas, E., Sluijs, A., Bohaty, S., and Zachos, J.C., 2010. High-resolution deep-sea carbon and oxygen isotope records of Eocene Thermal Maximum 2 and H2. Geology 38, 607–610.
Thrasher, B.L., Sloan, L.C., 2009. Carbon dioxide and the early Eocene climate of western North America. Geology 37, 807–810.
Thrasher, B.L., Sloan, L.C., 2010. Land cover influences on the regional climate of western North America during the early Eocene. Global and Planetary Change 72, 25–31.
Tipple, B.J., Meyers, S.R., Pagani, M., 2010. Carbon isotope ratio of Cenozoic CO_2: A comparative evaluation of available geochemical proxies. Paleoceanography 25, PA3202.
Wilf, P., Cuneo, N.R., Johnson, K.R., Hicks, J.F., Wing, S.L., Obradovich, J.D., 2003. High plant diversity in Eocene South America: Evidence from Patagonia. Science 300, 122–125.
Wolfe, J.A., 1994. Tertiary climatic changes at middle latitudes of western North America. Palaeogeography, Palaeoclimatology, Palaeoecology 108, 195–205.
Yapp, C.J., 2004. Fe (CO_3) OH in goethite from a mid-latitude North American Oxisol: Estimate of atmospheric CO_2 concentration in the early Eocene 'climatic optimum'. Geochimica et Cosmochimica Acta 68, 935–947.
Zachos, J., Pagani, M., Sloan, L., Thomas, E., Billups, K., 2001. Trends, rhythms, and aberrations in global climate 65 Ma to Present. Science 292, 686–693.

Zachos, J.C., Wara, M.W., Bohaty, S., Delaney, M.L., Petrizzo, M.R., Brill, A., Bralower, T.J., Premoli-Silva, I., 2003. A transient rise in tropical sea surface temperature during the Paleocene-Eocene Thermal Maximum. Science 302, 1551–1554.

Zachos, J., Dickens, G.R., Zeebe, R.E., 2008. An early Cenozoic perspective on greenhouse warming and carbon-cycle dynamics. Nature 451, 279–283.

Zonneveld, J.P., Gunnell, G.F., Bartels, W.S., 2000. Early Eocene fossil vertebrates from the southwestern Green River Basin, Lincoln and Uinta counties, Wyoming. Journal of Vertebrate Paleontology 20, 369–386.

CHAPTER III

A new paleoprecipitation proxy based on soil magnetic properties: Implications for expanding paleoclimate reconstructions during the EECO

Official citation:
Hyland, E.G., Sheldon, N.D., Van der Voo, R., Badgley, C.E., Abrajevitch, A., *in preparation*. A new paleoprecipitation proxy based on soil magnetic properties: Implications for expanding paleoclimate reconstructions.

ABSTRACT

Describing precipitation patterns and changes in the hydrological cycle during periods of past global change is crucial for providing an understanding of terrestrial climate systems and for predicting impacts of future climate change, such as shifting water availability. While a number of proxies and climofunctions exist for reconstructing paleoprecipitation using paleosols, all of the available tools for predicting paleoprecipitation are either limited to certain precipitation ranges (effective only for low-precipitation regimes; e.g., depth to Bk, CIA-K), or are relevant only to a limited range of paleosols (single-pedotype relationships; e.g., CALMAG). Here we measure the acquisition of isothermal remanent magnetization in modern soils to quantify the ratio of pedogenic magnetic minerals goethite and hematite, and use the relationship between these soil magnetic properties and measured climatic variables at each soil site to describe a new quantitative proxy for precipitation. By compiling both literature-derived and measured goethite-hematite (G/H) ratios and mean annual precipitation estimates for a global suite of modern soils ($n = 70$), we describe a strong ($R^2 = 0.96$) linear relationship between the G/H ratios of soil B-

horizons and mean annual precipitation that can be used to estimate paleoprecipitation values for a wide range of climatic regimes (100–3300 mm yr^{-1}) and soil types (Inceptisols, Alfisols, Ultisols, Oxisols, Mollisols, Aridisols, Spodosols). The new climofunction is verified using paleosols from the early Eocene of Wyoming, which show that estimates based on G/H ratios compare favorably to previously published estimates based on paleosols and paleobotany.

3.1 INTRODUCTION

Paleoprecipitation reconstructions are essential for predicting impacts of future climate change and for preparing for potential changes in terrestrial environmental conditions such as shifting regional rainfall amounts, which in turn will impact water resource availability and crop growth patterns (Piao et al., 2010; Choat et al., 2012). As a result, reliable proxy records of paleoprecipitation, especially from past warm periods, are a valuable tool for assessing and modeling future soil and plant moisture and local water availability (Piao et al., 2010; Valdes, 2011). Because soil formation is widespread and controlled primarily by climatic factors (Jenny, 1941), paleosol-based proxies provide an important archive of terrestrial climate that is applicable on significantly longer timescales than records from ice cores, and which give greater spatial coverage than local records from sources like lake cores or botanical (pollen) records (e.g., Retallack, 2001).

A number of paleoprecipitation proxies (mean annual precipitation; MAP) have been derived for paleosols, and these proxies have been useful in describing hydrological changes during periods of global climate change at multiple points during the Cenozoic (e.g., Retallack, 2005; Hyland and Sheldon, 2013), and in older paleosol successions (e.g., Retallack et al., 2011; De la Horra et al., 2012). However, each of the available proxies is limited in terms of its applications: the chemical index of alteration (CIA-K) proxy of Sheldon et al. (2002) is limited to MAP < 1600 mm yr^{-1} and is therefore only applicable to arid-humid environments; the depth to Bk horizon proxy of Retallack (2005) applies only to pedogenic carbonate-bearing soils, which generally receive MAP of < 750 mm yr^{-1}, and so is limited to arid to semi-arid environments; and the CALMAG weathering index of Nordt and Driese (2010) applies only to Vertisols, which represent a minor fraction (ca. 7%) of global soils. Therefore, a critical gap

exists between the range of potential global paleoenvironments and the applicable zones of available proxies for paleoprecipitation.

In order to address better the full range of potential paleoenvironments, we use the magnetic properties of modern soils to assess their average hydration state, and relate that to mean annual precipitation for the environment. Magnetic properties such as bulk susceptibility have been extensively researched as climatic descriptors (e.g., Maher and Thompson, 1995; Balsam et al., 2011), but due to the limited availability (i.e., loess sequences are not temporally or spatially ubiquitous) and preservation potential of susceptibility signals in pre-Quaternary loessic profiles (e.g., Retallack et al., 2003), and due to the limited climatic range (MAP < 1000 mm yr^{-1}) of precipitation relationships with susceptibility (Balsam et al., 2011), we instead investigate the relationship between precipitation and the abundance of magnetic minerals goethite and hematite in soils.

Previous work on the magnetic properties of sediments and other magnetic materials has shown that the relative proportion of the magnetic minerals goethite and hematite depends on the hydration state of the material, with higher proportions of goethite (FeO[OH]) versus hematite (Fe_2O_3) in materials with a hydrated (or wetter) average state (Cornell and Schwertmann, 2003; Abrajevitch et al., 2009). As a result, a simple ratio of goethite to hematite (G/H) can be used to describe the hydration state of a given sample (e.g., Abrajevitch et al., 2009). Both goethite and hematite are formed in large quantities during pedogenesis, where their relative abundance has been shown to be directly related to moisture availability during soil formation (e.g., Yapp, 2001; Cornell and Schwertmann, 2003), and does not depend on the composition of soil parent material (e.g., Tardy and Roquin, 1992; Sangode and Bloemendal, 2004). The highly sensitive relationship between G/H ratios and climatic conditions (specifically precipitation regime) has

been noted on small spatial scales for decades (e.g., Schwertmann and Kampf, 1985; Singh and Gilkes, 1992), but no quantitative assessment of the relationship between the abundance of pedogenic magnetic minerals (goethite and hematite) and climatic variables has been previously published. Therefore, we compiled a database of both literature-derived and newly measured G/H ratios from a wide variety of soil types and climatic zones in order to derive a novel and potentially widely applicable paleoprecipitation proxy.

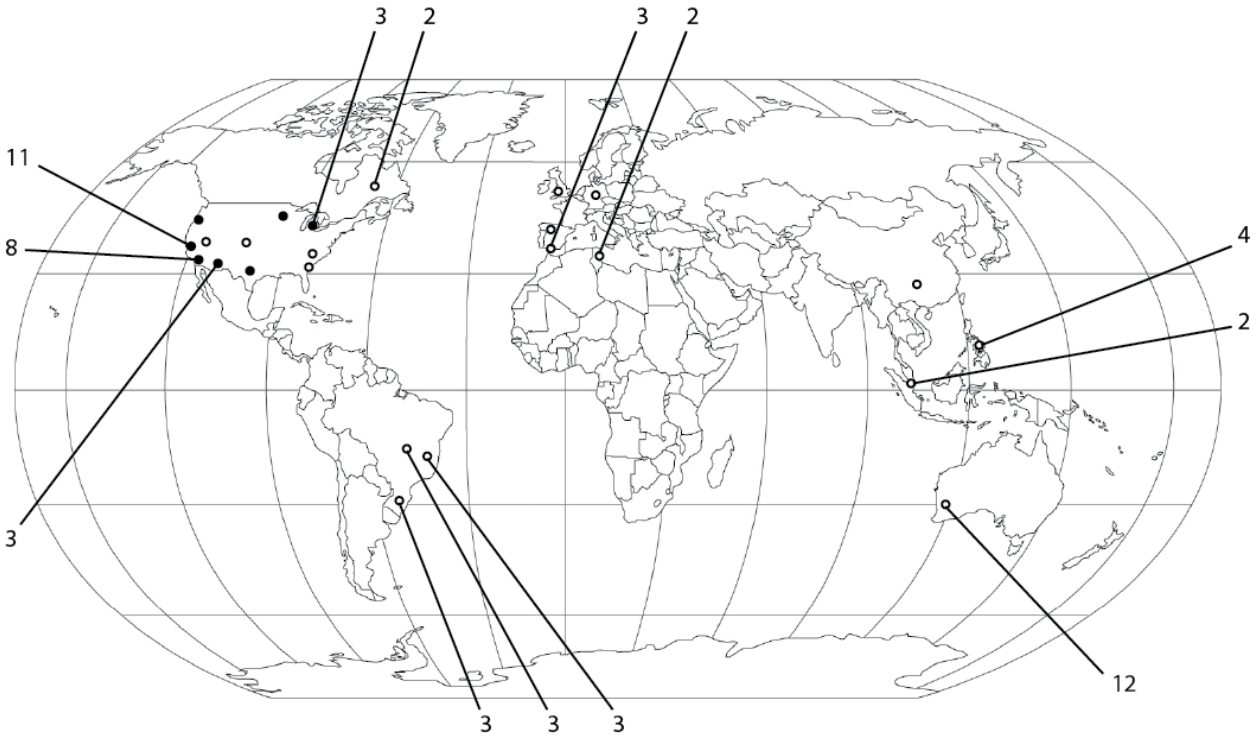

Figure 3.1 Location map of modern soils sampled or compiled for this study (n = 70). Closed symbols mark soil sample locations from this work, and open symbols indicate literature-derived soil sample locations (see Appendix B1 for exact locations). Numerical tags indicate the number of soils sampled in a particular region, and those without tags are for individual localities.

3.2 METHODS

Soil magnetic data (G/H ratios) were compiled from thirteen different studies of modern soils throughout the world (Figure 3.1; Appendix B1). In order to standardize magnetic data from these 42 soils, we used mean goethite and hematite values of B-horizon samples and have converted all data to simple ratios of goethite–hematite (G/H). B-horizon sample data were used because the long formation time necessary for horizonation to develop allows for the equilibration or time-averaging of the soil hydration state, thus avoiding year-to-year variability or short-term climatic events (Sheldon and Tabor, 2009). Due to the limitations of location specificity in the literature, available climate data for sampling locations, and soil profile descriptions (B-horizons) for locations, only G/H data from sites with detailed information about geographic location and soil profile descriptions in the selected literature were used in the modern soil compilation.

In order to expand the available dataset of goethite–hematite ratios from modern soils in a range of climatic zones, B-horizon samples were collected from 28 different soil series in the central and western United States (Figure 3.1) that were archived by the USDA (Lincoln, NE) and at the University of Michigan (Ann Arbor, MI). This dataset includes B-horizon samples from modern Alfisols, Aridisols, Inceptisols, Mollisols, Oxisols, Spodosols, and Ultisols, and spans a wide range of mean annual precipitation and temperature regimes (Appendix B1). Climate data were either reported in the selected literature or were sourced from National Oceanic and Atmospheric Administration (NOAA) and United Nations' World Meteorological Organization (WMO) climate normals for the nearest weather station (National Climatic Data Center, 2002; WMO, 2010).

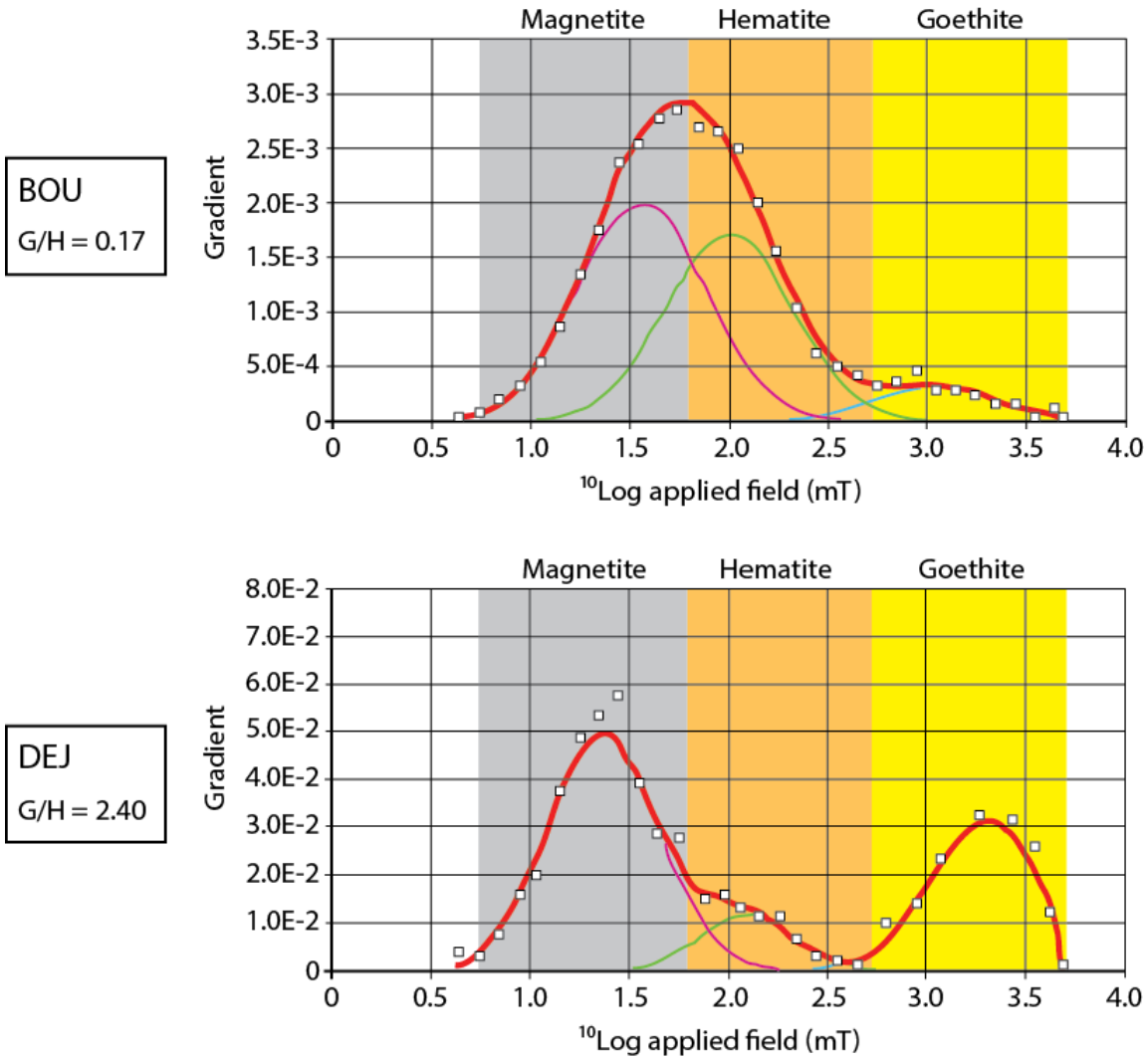

Figure 3.2 Example gradient acquisition plots showing coercivity curves (red line) and magnetic carrier parameters (other colored lines) for exemplar samples with low (BOU) and high (DEJ) goethite–hematite ratios.

Differences in coercivity were used in order to identify relative proportions of these magnetic minerals (goethite, hematite) in the modern soil samples. Analyzed samples from paleosol B-horizons were pulverized and homogenized. We analyzed isothermal remanent magnetization (IRM) acquisition curves that resulted from the stepwise impulse magnetization of these samples from 0–4.7T by inputting these data into the IRM cumulative log-Gaussian fitting program of Kruiver et al. (2001). Based on the distribution parameters of these IRM acquisition curves, including saturation IRM (SIRM), the mean coercivity (field at which half of the SIRM

is acquired), and the width or dispersion of the IRM distribution, it is possible to distinguish individual magnetic carriers and their relative abundance within a given soil sample even at very low (< 0.05 wt%) total concentrations (Figure 3.2; e.g., Kruiver et al., 2001; Heslop and Dillon, 2007). These abundances were then converted to a goethite–hematite ratio (G/H) in order to compare these measurements to all literature-derived data (Appendix B1). This combined dataset therefore includes both mass-based (from the literature) and magnetically-derived measurements, which are considered equally viable for determining G/H ratios due to their 1:1 relationship in a range of modern soils that were measured for comparison via X-ray diffraction (Figure 3.3).

3.3 PRECIPITATION PROXY

The 70 modern soils sampled produced B-horizon goethite–hematite ratios (G/H) between 0.05 and 2.75, and were measured from soils with a range of mean annual precipitation values between 100 and 3300 mm yr^{-1} (see Appendix B1). The relationship between G/H and mean annual precipitation (MAP) values in soils is based on the fact that goethite and hematite are both formed pedogenically (*in situ*) as a function of moisture availability during soil development (e.g., Yapp, 2001; Cornell and Schwertmann, 2003). While surface moisture availability in soils can be highly variable due to evapotranspiration and vegetation type or abundance (e.g., Waddell and Weil, 1996), most soils (see below for exceptions) exhibit stable long-term average hydration conditions in B-horizons related to climatic conditions such as local precipitation (e.g., Schwertmann and Kampf, 1985; Singh and Gilkes, 1992; Bartlett and James, 1993).

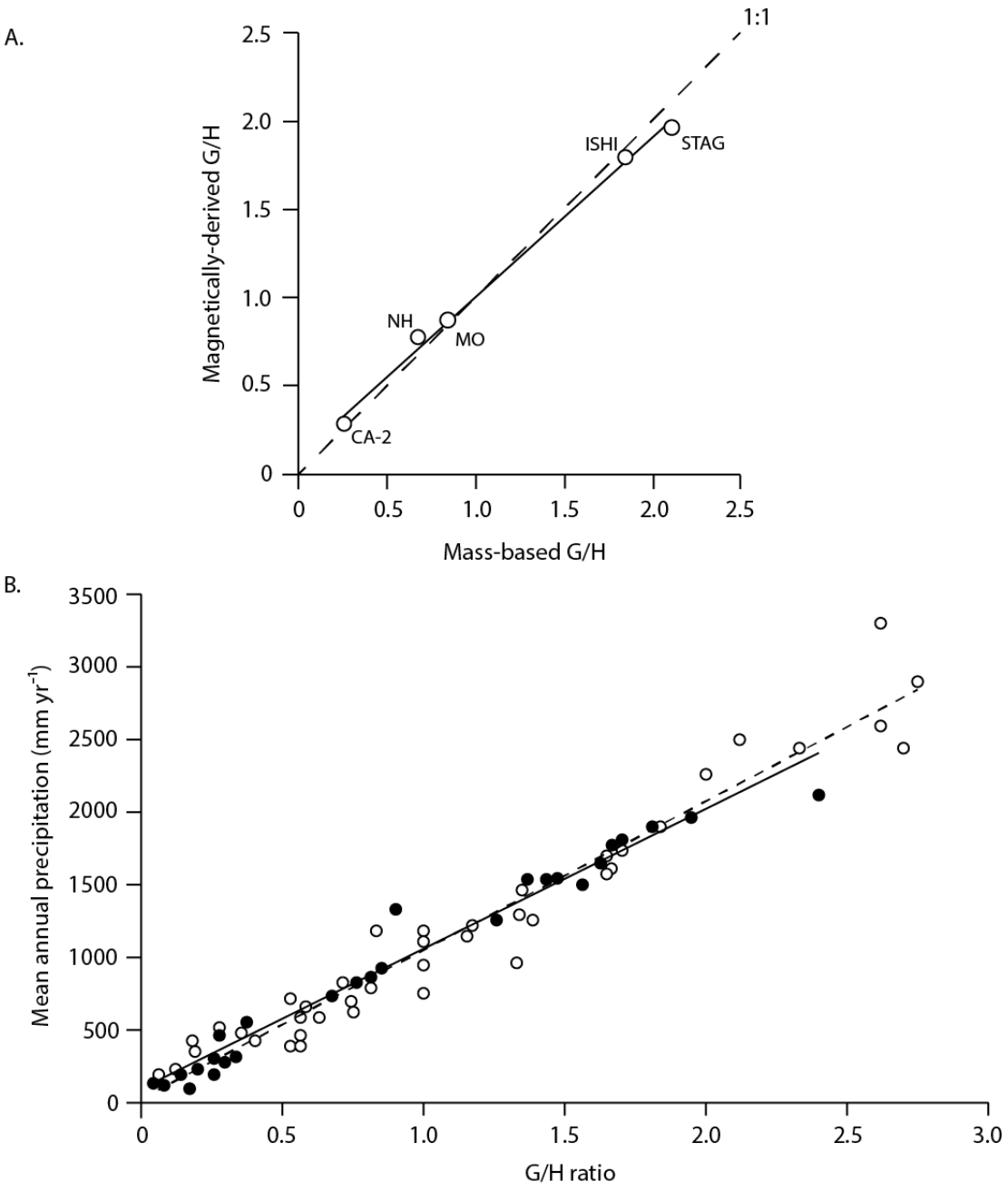

Figure 3.3 A) Comparison of G/H ratios from mass-based (XRD analysis via Scintag X1 XRD at the University of Michigan using a Cu radiation source set at 1.2 kW, with WildFire curve-fitting analysis; e.g., Reynolds, 1993; Downs, 2006) and magnetically-based (IRM acquisition with curve fitting; e.g., Kruiver et al., 2001) methods. Note that estimates show a strong and nearly 1:1 relationship for modern soils, and that this relationship is likely conserved in paleosol material (Carter-Stiglitz et al., 2006). B) Replotting of full dataset with data divided into mass-based (open) and magnetically-based (closed) categories. Note that the slope and intercept of trendlines for each subset (dashed = open; solid = closed) is nearly identical.

This relationship between G/H and MAP values is used to derive a new paleoprecipitation proxy by plotting soil G/H values against their respective MAP values (Figure 3.4); linear regression through this dataset produces the following equation, which has a standard error of ±157 mm yr^{-1}:

$$MAP\ (mm\ yr^{-1}) = 1003.5\ \times (G/H) + 49.3 \qquad (3.1)$$

G/H and MAP values were highly related ($R^2 = 0.96$; Figure 3.4), and the strength of this relationship is highly significant ($p < 0.001$). As a result, the relationship between G/H ratios and mean annual precipitation has both a substantially stronger predictive power and a smaller standard error than other available quantitative precipitation proxies (c.f., CIA-K). Multivariate regressions with other climatic variables such as mean annual temperature (MAT) and range of mean monthly precipitation (RMMP) were not found to be significant (Appendix B1).

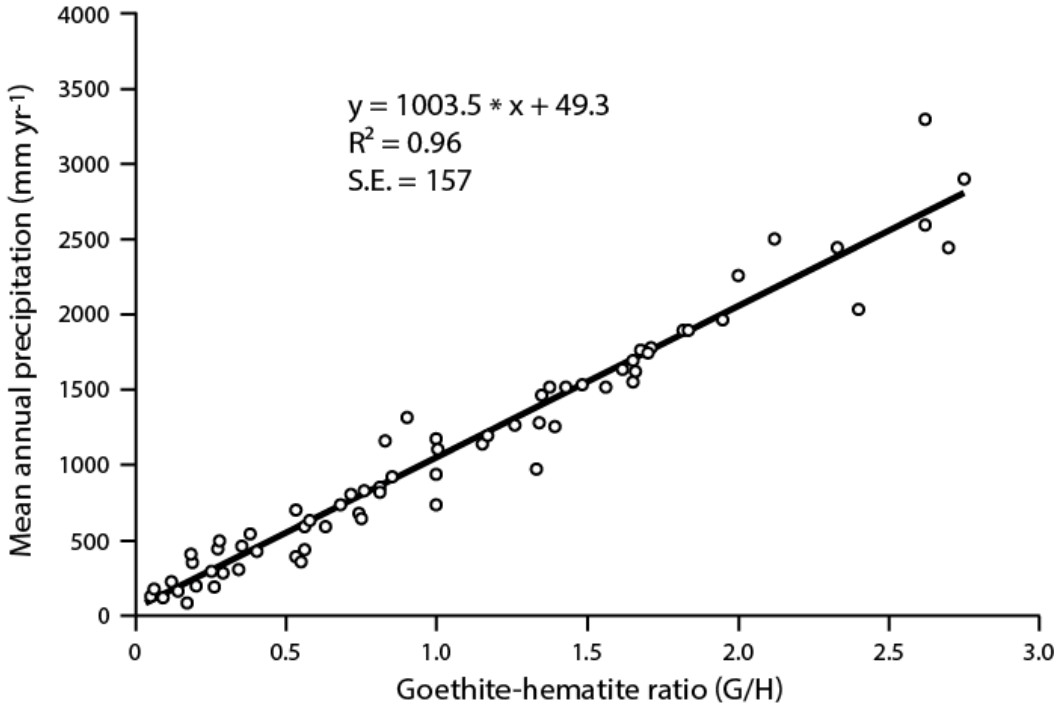

Figure 3.4 Relationship between mean annual precipitation (MAP) and goethite–hematite ratios (G/H) of modern soils worldwide. Linear regression describes the G/H paleoprecipitation proxy (Equation 3.1), for which $R^2 = 0.96$ and standard error (S.E.) is ±157 mm yr^{-1}.

3.4 APPLICABILITY OF THE NEW PROXY

The wide range of climatic conditions, soil types, and geographic settings represented in the dataset (Figure 3.1; Appendix B1) suggests that this paleoprecipitation proxy relationship is applicable worldwide, including under past greenhouse conditions where hydrologic cycling was likely more rapid and precipitation may have been higher than present values in many regions (e.g., Bowen et al., 2004; Hyland and Sheldon, 2013). While this paleoprecipitation proxy should be widely applicable, there are a few important limitations. The G/H proxy should not be applied to soils with evidence of significant or extreme seasonality (e.g., vertic features/Vertisols; Mack et al., 1993), as soils experiencing vertical mixing and substantial variability in water availability throughout the year may have extremely variable G/H values or a non-linear relationship between hydration conditions and MAP (e.g., Kampf and Schwertmann, 1983). Additionally, this proxy is not suitable for very weakly developed soils (e.g., Entisols; Mack et al., 1993) or channel-proximal sediments, as poorly developed B-horizons and excess waterlogging of soil horizons due to fluvially controlled water-table fluctuations can result in artificially elevated goethite–hematite ratios (e.g., Torrent et al., 2010). Lastly, this proxy is not applicable for paleosols that have experienced burial to depths >10 km due to the conversion of pedogenic goethite to remineralized hematite; goethite undergoes an oxidative transformation at temperatures exceeding 250–270 °C (Gualtieri and Venturelli, 1999), which in continental sedimentary basins are typically reached at depths in excess of 10 km (e.g., Bjorlykke, 2010). In spite of these caveats, the G/H paleoprecipitation proxy is applicable to a much wider range of conditions than any other available proxy, especially at high mean annual precipitation values (c.f., Sheldon et al., 2002; Retallack, 2005; Balsam et al., 2011).

3.5 PALEOPRECIPITATION CASE STUDY

In order to evaluate the effectiveness of the new precipitation proxy, we derived paleoprecipitation estimates for early Eocene paleosols from the Wasatch Formation of southwestern Wyoming (Green River Basin). This dataset included 16 paleosols spanning the Early Eocene Climatic Optimum (EECO; 52–50 Mya), an event which was characterized by a large-scale shift in precipitation regimes (Figure 3.5; Hyland and Sheldon, 2013). Published precipitation estimates from the Formation were based on depth to Bk horizon and bulk geochemistry climofunctions (Hyland and Sheldon, 2013), as well as paleobotanical proxies (Wilf et al., 1998), all of which provide a robust comparison for G/H ratio estimates.

Based on these three published proxy records, precipitation in the Green River Basin during the peak of the EECO has been characterized as roughly doubling between 52 and 51 Mya (Wilf et al., 1998; Hyland and Sheldon, 2013; Appendix B2). Depth to Bk estimates (based on climofunctions in Retallack, 2005) and bulk geochemistry estimates (based on CIA-K climofunctions of Sheldon et al., 2002) both show a change from early Eocene baseline estimates around 500–600 mm yr^{-1} to peak estimates of roughly 1000–1200 mm yr^{-1}, followed by a decline back to baseline values (Figure 3.5; Hyland and Sheldon, 2013). While paleobotanical estimates of the EECO from Wyoming have lower spatial and temporal resolution than paleosol estimates, they also indicate a similar range of precipitation values for the event; Wilf et al. (1998) use an independently-derived leaf-area regression called MlnA (comparable to Climate Leaf-Analysis Multivariate Program) to estimate early Eocene baseline precipitation around 850 mm yr^{-1}, with peak values approaching 1200 mm yr^{-1} (Figure 3.5).

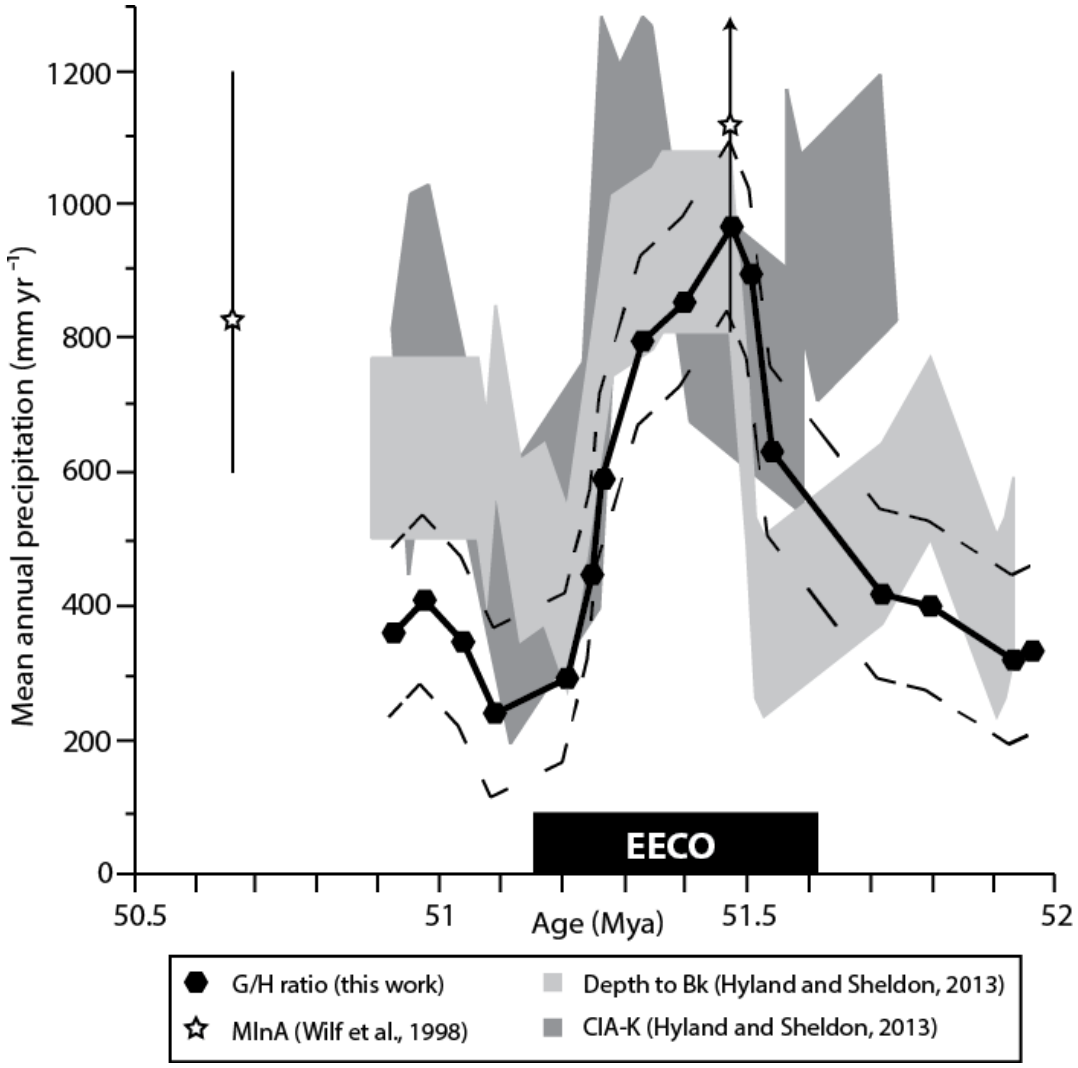

Figure 3.5 Comparison of mean annual precipitation estimates from the Eocene Green River Basin (Wyoming, USA) case study. Proxy estimates from G/H ratios (filled symbols) indicate similar results to paleobotanical (MlnA, Wilf et al., 1998), paleopedological (depth to Bk, Hyland and Sheldon, 2013), and geochemical (CIA-K; Hyland and Sheldon, 2013) estimates for the Early Eocene Climatic Optimum.

While all of these records are in good agreement, each has a complicating issue that makes them incomplete individual records of the EECO event. Depth to Bk estimates are inherently minimum precipitation values due to soil profile erosion and compaction, and are unavailable for paleosols in higher precipitation regimes (e.g., peak EECO; 51.7–51.6 Mya) because carbonates rarely form in sub-humid and wetter soils (> 750 mm yr^{-1}; Retallack, 2005). Bulk geochemistry estimates are more widely applicable in climate terms, but require more well-

developed paleosols (Bt-horizon), thus no estimates are possible for 52.0–51.7 Mya (Figure 3.5). Paleobotanical estimates of paleoprecipitation require the preservation of relatively complete leaf specimens for analysis, which are uncommon for floras in this region during the early Eocene, and as a result there are only two estimates through the EECO in southwestern Wyoming (Figure 3.5; Wilf et al., 1998). Additionally, both available paleobotanical estimates have substantially higher uncertainty than paleosol-based estimates (as much as 700 mm yr^{-1}; Wilf et al., 1998).

Using the goethite–hematite ratio paleoprecipitation proxy for these same Green River Basin paleosols, estimated precipitation values range between 240 and 973 mm yr^{-1}, with a change of roughly 650 mm yr^{-1} during the peak EECO (Figure 3.5). When compared to published estimates from paleopedological (depth to Bk; Hyland and Sheldon, 2013), geochemical (CIA-K; Hyland and Sheldon, 2013), and paleobotanical (MlnA; Wilf et al., 1998) proxies, these data show both a similar temporal trend and a similar magnitude shift in precipitation regime across the EECO, and also fill in times not covered by other datasets (Figure 3.5). In some cases the estimate of MAP based on G/H ratios is lower than other estimates (similar to depth to Bk, which have been shown to be minimum values; Retallack, 2005; Sheldon and Tabor, 2009), which could potentially indicate the influence of paleosol oxidation over time either as a result of burial diagenesis or the impact of the surface weathering of paleosols in the modern dry climate of Wyoming. As a result of the unidirectional oxidative transformation of goethite to hematite, G/H ratio estimates from visibly reddened paleosols (such as those used here) should be interpreted as a minimum estimate of paleoprecipitation. However, the error envelopes (defined by standard error) between the G/H ratio and other proxy estimates from this site are overlapping, and these data consistently describe large-scale precipitation changes in the deep past (e.g., the EECO), which suggests that soil magnetic properties like goethite–hematite

ratios can serve as a robust quantitative proxy for paleoprecipitation. While more case studies are necessary to confirm the applicability of this proxy to different continents and timescales and more work should be undertaken to describe lateral heterogeneity of G/H ratios within soil catenas (specifically in soil A-horizons, which are not addressed here), this study provides a new and widely applicable method for describing past changes in the hydrological cycle.

3.6 CONCLUSIONS

Understanding precipitation in the present and during past episodes of climate change is important for determining and preparing for impacts of the hydrological cycle on global environmental systems in the future. Soil magnetic properties, specifically the ratio of pedogenic goethite to hematite, can be related quantitatively to modern precipitation regimes worldwide via a highly significant ($p < 0.001$) and extremely strong ($R^2 = 0.96$) linear regression model. This newly derived relationship serves as a precipitation proxy that is applicable to a wide range of soil types and climatic regimes worldwide, and the resulting climofunction has been robustly applied to paleosols in order to estimate paleoprecipitation during the Early Eocene Climatic Optimum, a rapid global climate change event.

REFERENCES CITED

Abrajevitch, A., Van der Voo, R., Rea, D.K., 2009. Variations in relative abundances of goethite and hematite in Bengal Fan sediments: Climatic vs. diagenetic signals. Marine Geology 267, 191–206.

Anand, R.R., Gilkes, R.J., 1987. Iron oxides in lateritic soils from western Australia. Journal of Soil Science 38, 607–622.

Balsam, W.L., Ellwood, B.B., Ji, J., Williams, E.R., Long, X., El Hassani, A., 2011. Magnetic susceptibility as a proxy for rainfall: Worldwide data from tropical and temperate climate. Quaternary Science Reviews 30, 2732–2744.

Bartlett, R.J., James, B.R., 1993. Redox chemistry of soils. Advances in Agronomy 50, 151–208.

Bigham, J.M., Golden, D.C., Bowen, L.H., Buol, S.W., Weed, S.B., 1978. Iron oxide mineralogy of well-drained Ultisols and Oxisols: Characterization of iron-oxides in soil clays by Mossbauer-spectroscopy, X-ray-diffractometry, and selected chemical techniques. Soil Science Society of America Journal 42, 816–825.

Bjorlykke, K., 2010. Heat transport in sedimentary basins. In: Bjorlykke, K. (Ed.), Petroleum Geoscience: From sedimentary environments to rock physics, Springer (New York), 253–260.

Bowen, G.J., Beerling, D.J., Koch, P.L., Zachos, J.C., Quattlebaum, T., 2004. A humid climate state during the Palaeocene/Eocene thermal maximum. Nature 432, 495–499.

Carter-Stiglitz, B., Banerjee, S.K., Gourlan, A., Oches, E., 2006. A multiproxy study of Argentina loess: Marine oxygen isotope stage 4 and 5 environmental record from pedogenic hematite. Palaeogeography, Palaeoclimatology, Palaeoecology 239, 45–62.

Choat, B., Jansen, S., Brodribb, T.J., Cochard, H., Delzon, S., Bhaskar, R., Bucci, S.J., Field, T.S., Gleason, S.M., Hacke, U.G., Jacobsen, A.L., Lens, F., Maherali, H., Martinez-Vilalta, J., Mayr, S., Mencuccini, M., Mitchel, P.J., Nardini, A., Pittermann, J., Pratt, R.B., Sperry, J.S., Westoby, M., Wright, I.J., Zanne, A.E., 2012. Global convergence in the vulnerability of forests to drought. Nature 491, 752–755.

Cornell, R.M., Schwertmann, U., 2003. The iron oxides: Structure, properties, reactions, occurrences, and uses. Wiley-VCH (Weinheim), pp.664.

Curi, N., Franzmeier, D.P., 1987. Effect of parent rocks on chemical and mineralogical properties of some Oxisols in Brazil. Soil Science Society of America Journal 51, 153–158.

De la Horra, R., Galan-Abellan, A.B., Lopez-Gomez, J., Sheldon, N.D., Barrenechea, J.F., Luque, F.J., Arche, A., Benito, M.I., 2012. Paleoecological and paleoenvironmental changes during the continental Middle-Late Permian transition at the SE Iberian Ranges, Spain. Global and Planetary Change 94-95, 46–61.

Downs, R.T., 2006. The RRUFF Project: An integrated study of the chemistry, crystallography, Raman and infrared spectroscopy of minerals. Program and Abstracts of the 19th General Meeting of the International Mineralogical Association (Kobe, Japan), O03-13.

France, D.E., Oldfield, F., 2000. Identifying goethite and hematite from rock magnetic measurements of soils and sediments. Journal of Geophysical Research 105, 2781–2795.

Geiss, C.E., Zanner, C.W., Banerjee, S.K., Joanna, M., 2004. Signature of magnetic enhancement in a loessic soil in Nebraska, United States of America. Earth and Planetary Science Letters 189, 269–276.

Gualtieri, A.F., Venturelli, P., 1999. In situ study of the goethite–hematite phase transformation by real time synchrotron powder diffraction. American Mineralogist 84, 895–904.

Heslop, D., Dillon, M., 2007. Unmixing magnetic remanence curves without a priori knowledge. Geophysical Journal International 170, 556–566.
Hyland, E.G., Sheldon, N.D., 2013. Coupled CO2-climate response during the Early Eocene Climatic Optimum. Palaeogeography, Palaeoclimatology, Palaeoecology 369, 125–135.
Jenny, H., 1941. Factors of Soil Formation: A system of quantitative pedology. Dover Publications Inc. (New York), pp. 281.
Kampf, N., Schwertmann, U., 1983. Goethite and hematite in a climosequence in southern Brazil and their application in classification of kaolinitic soils. Geoderma 29, 27–39.
Kruiver, P.P., Dekkers, M.J., Heslop, D., 2001. Quantification of magnetic coercivity components by the analysis of acquisition curves of isothermal remanent magnetization. Earth and Planetary Science Letters 189, 269–276.
Mack, G.H., James, W.C., Monger, H.C., 1993. Classification of paleosols. Geological Society of America Bulletin 105, 129–136.
Maher, B.A., Thompson, R., 1995. Paleorainfall reconstructions from pedogenic magnetic susceptibility variations in the Chinese loess and paleosols. Quaternary Research 44, 383–391.
National Climatic Data Center, 2002. United States Climate Normals: 1971–2000. Climatography of the US: National Oceanic and Atmospheric Administration, http://www.ncdc.noaa.gov/data#normals, Accessed: 6/2013.
Navarrete, I.A., Tsutsuki, K., Kondo, R., Asio, V.B., 2008. Genesis of soils across a late Quaternary volcanic landscape in the humid tropical island of Leyte, Philippines. Australian Journal of Soil Research 46, 403–414.
Nordt, L.C., Driese, S.D., 2010. New weathering index improves paleorainfall estimates from Vertisols. Geology 38, 407–410.
Piao, S., Ciais, P., Huang, Y., Shen, Z., Peng, S., Li, J., Zhou, L., Liu, H., Ma, Y., Ding, Y., Friedlingstein, P., Liu, C., Tan, K., Yu, Y., Zhang, T., Fang, J., 2010. The impacts of climate change on water resources and agriculture in China. Nature 467, 43–51.
Prudencio, M.I., Dias, M.I., Waerenborgh, J.C., Ruiz, F., Trindade, M.J., Abad, M., Marques, R., Gouveia, M.A., 2011. Rare earth and other trace and major elemental distribution in a pedogenic calcrete profile (Slimene, NE Tunisia). Catena 87, 147–156.
Retallack, G.J., 2001. Soils of the Past: An introduction to paleopedology. Blackwell Science (Malden), pp. 404.
Retallack, G.J., 2005. Pedogenic carbonate proxies for amount and seasonality of precipitation in paleosols. Geology 33, 333–336.
Retallack, G.J., Sheldon, N.D., Cogoini, M., Elmore, R.D., 2003. Magnetic susceptibility of early Paleozoic and Precambrian paleosols. Palaeogeography, Palaeoclimatology, Palaeoecology 198, 373–380.
Retallack, G.J., Sheldon, N.D., Carr, P.F., Fanning, M., Thompson, C.A., Williams, M.L., Jones, B.G., Hutton, A., 2011. Multiple early Triassic greenhouse crises impeded recovery from Late Permian mass extinction. Palaeogeography, Palaeoclimatology, Palaeoecology 308, 233–251.
Reynolds, R.C., 1993. Wildfire: A computer program for the calculation of three-dimensional powder X-ray diffraction patterns for polytypes and their disordered variations. Reynolds and Reynolds: http://www.angelfire.com/md/newmod/#wildfire, Accessed: 10/2013.

Sangode, S.J., Bloemendal, J., 2004. Pedogenic transformation of magnetic minerals in Pliocene-Pleistocene palaeosols of the Siwalik Group, NW Himalaya, India. Palaeogeography, Palaeoclimatology, Palaeoecology 212, 95–118.
Schulze, D.G., 1981. Identification of soil iron-oxide minerals by differential X-ray-diffraction. Soil Science Society of America Journal 45, 437–440.
Schwertmann, U., Kampf, N., 1985. Properties of goethite and hematite in kaolinitic soils of southern and central Brazil. Soil Science 139, 344–350.
Sheldon, N.D., Tabor, N.J., 2009. Quantitative paleoenvironmental and paleoclimatic reconstruction using paleosols. Earth-Science Reviews 95, 1–52.
Sheldon, N.D., Retallack, G.J., Tanaka, S., 2002. Geochemical climofunctions from North American soils and applications to paleosols across the Eocene-Oligocene boundary in Oregon. Journal of Geology 110, 687–696.
Singh, B., Gilkes, R.J., 1992. Properties and distribution of iron-oxides and their association with minor elements in the soils of south-western Australia. Journal of Soil Science 43, 77–98.
Tardy, Y., Roquin, C., 1992. Geochemistry and evolution of lateritic landscapes. In: Martini, I.P., Chesworth, W. (Eds.), Developments in Earth Surface Processes, Elsevier (Amsterdam), pp. 407–443.
Torrent, J., Schwertmann, U., Schulze, D.G., 1980. Iron oxide mineralogy of some soils of two river terrace sequences in Spain. Geoderma 23, 191–208.
Torrent, J., Liu, Q., Barron, V., 2010. Magnetic susceptibility changes in relation to pedogenesis in a Xeralf chronosequence in northwestern Spain. European Journal of Soil Science 61, 161–173.
Valdes, P., 2011. Built for stability. Nature Geoscience 4, 414–416.
Waddell, J., Weil, R., 1996. Water distribution in soil under ridge-till and no-till corn. Soil Science Society of America Journal 60, 230–237.
Wang, C., Ross, G.J., Protz, R., 1989. Effect of crystalline iron-oxides on development and classification of podzolic soils in western Labrador, Newfoundland. Soil Science Society of America Journal 53, 870–875.
Wilf, P., Wing, S.L., Greenwood, D.R., Greenwood, C.L., 1998. Using fossil leaves as paleoprecipitation indicators: An Eocene example. Geology 26, 203–206.
World Meteorological Organization, 2010. Standard Climate Normals: 1961–1990. United Nations Statistics Division, http://data.un.org/Data.aspx?d=CLINO&f=ElementCode%3a06, Accessed: 6/2013.
Yapp, C., 2001. Rusty relics of Earth history: iron oxides, isotopes, and surficial environments. Annual Reviews of Earth and Planetary Sciences 29, 165–199.

CHAPTER IV

Terrestrial paleoenvironmental reconstructions indicate transient peak warming during the Early Eocene Climatic Optimum

Official citation:
Hyland, E.G., Sheldon, N.D., Fan, M., 2013. Terrestrial paleoenvironmental reconstructions indicate transient peak warming during the early Eocene climatic optimum. Geological Society of America Bulletin 125, 1338–1348.

ABSTRACT

Major changes in climate and ecology occurred during the Early Eocene Climatic Optimum, sometime between 52 and 50 Mya. Recent work suggests that the timing and duration of the event are characterized by different responses in the marine and terrestrial realms, and that traditional causal mechanisms may not adequately explain such differences. We applied high-resolution paleopedology, geochemical analysis, and phytolith biostratigraphy techniques to paleosol suites within the well-described Wind River Formation of western Wyoming, USA. This multiproxy record indicates a short (<1 Ma) peak period of carbon isotopic enrichment (up to 2‰ higher) and elevated pCO_2, high temperatures (up to 8 °C higher), increased precipitation (up to 500 mm yr^{-1} higher), and shifts in floral composition (up to 10%). Terrestrial climatic and ecological changes of this kind during the Early Eocene Climatic Optimum are consistent with changes in contemporaneous records that have been ascribed to high atmospheric pCO_2, but a transient peak interval suggests that the cause of high atmospheric pCO_2 during the early Eocene was likely not increased volcanism or decreased silicate weathering, which operate on longer

timescales. Instead, terrestrial records from across western North America agree that Early Eocene Climatic Optimum changes may have been caused by other sources, such as a combination of increased ventilation of oceanic carbon and increased petroleum generation in sedimentary basins. The climatic and environmental changes exhibited by this and other North American terrestrial records also define a pattern of regional response that is relevant for understanding the impacts of global climate change events.

4.1 INTRODUCTION

4.1.1 Early Eocene Climatic Optimum

The Early Eocene Climatic Optimum (EECO) is one of the most important intervals of the Cenozoic in terms of understanding and predicting changes in global climate and ecological responses to major warming events. Recent work has shown that the EECO was the warmest period of the Cenozoic and correlates to major changes in both marine (e.g., Zachos et al., 2001, 2008) and terrestrial records (e.g., Greenwood and Wing, 1995; Hyland and Sheldon, 2013). Primarily observed from marine cores, the EECO is described as a broad temperature maximum spanning 52–50 Mya that correlates to increased atmospheric pCO_2 (e.g., Zachos et al., 2001). Increases in atmospheric carbon dioxide are considered the primary driver of these higher global temperatures and consequent faunal turnover events (e.g., Wasatchian-Bridgerian boundary; Zonneveld et al., 2000) and have been previously attributed to increased volcanism and changes in silicate weathering through the late Paleocene–early Eocene (Zachos et al., 2008). Despite the broad trend seen in marine records, many terrestrial records from North America (e.g., Sewall and Sloan, 2006; Hren et al., 2010; Hyland and Sheldon, 2013) and other continents (e.g., Wilf et al., 2003) indicate more rapid changes in temperature, precipitation, and ecology. This suggests that the climatic and ecological changes of the EECO may have been more transient events than previously defined, which provided the impetus for analyzing the high-resolution records of pedological, geochemical, isotopic, and biostratigraphic changes within a major terrestrial basin presented in this work.

4.1.2 Wind River Basin

The Wind River Basin is located in west-central Wyoming (USA; Figure 4.1), and it is one of many synorogenic Cretaceous–Eocene–age Laramide basins that have been structurally

and stratigraphically described in great detail (e.g., Keefer, 1965; Winterfeld and Conard, 1983; Smith et al., 2008; Fan et al., 2011). Despite significant work on the structural and sedimentological history of the basin, little has been done to characterize the climatic or ecological history of the region. The Wind River Basin and surrounding region have maintained a latitude similar to that of the present (±2°; Scotese, 2000) since at least the early Paleocene, and estimated basinal elevations remained unchanged and low through the Miocene (~0.5 km above sea level [asl]; Smith et al., 2008; Fan et al., 2011), indicating that any changes in early Eocene climate were likely not due to either latitudinal effects caused by changes in global circulation patterns (Thrasher and Sloan, 2009) or altitudinal effects caused by tectonic uplift of the basin itself (Fan et al., 2011).

Basinal facies are characterized primarily as fluvially deposited sediments sourced from the exhumation of local Precambrian structures like the Wind River Range to the west and Owl Creek Mountains to the north (Figure 4.1; Fan et al., 2011). The Wind River Formation itself is a series of interfingering pebble-cobble conglomerates, sandstones, and paleosols (Figure 4.2) that have been interpreted as a mid- to low-relief alluvial and braided fluvial system that deposited sediment between roughly 53.2 and 50.7 (±0.5 Ma) Mya, during the late Wasatchian (Wa6-Wa7) to early Bridgerian (Br0) North American Land Mammal Ages (NALMA; Stucky, 1984; Clyde et al., 1994, 1997, 2001; Smith et al., 2003; Machlus et al., 2004; Fan et al., 2011). Therefore, the formation spans the time period identified by marine paleoclimatic records as the EECO (e.g., Zachos et al., 2001).

Here, we examine a well-constrained terrestrial record of the Early Eocene Climatic Optimum through the paleopedology, geochemical properties, and phytolith assemblage analysis of two well-exposed sections of the Wind River Formation ~10 km east of the town of Dubois,

Wyoming (USA; Figure 4.1). The sites are distinct, though well correlated, and are herein referred to using the same terminology as the work of Fan et al. (2011), which defined and described the two sites: site 1DB, a 122 m stratigraphic section located at 43.501705°N, 109.531171°W (~2080 m asl); and site 2DB, a 301 m section located at 43.505628°N, 109.537177°W (~2055 m asl).

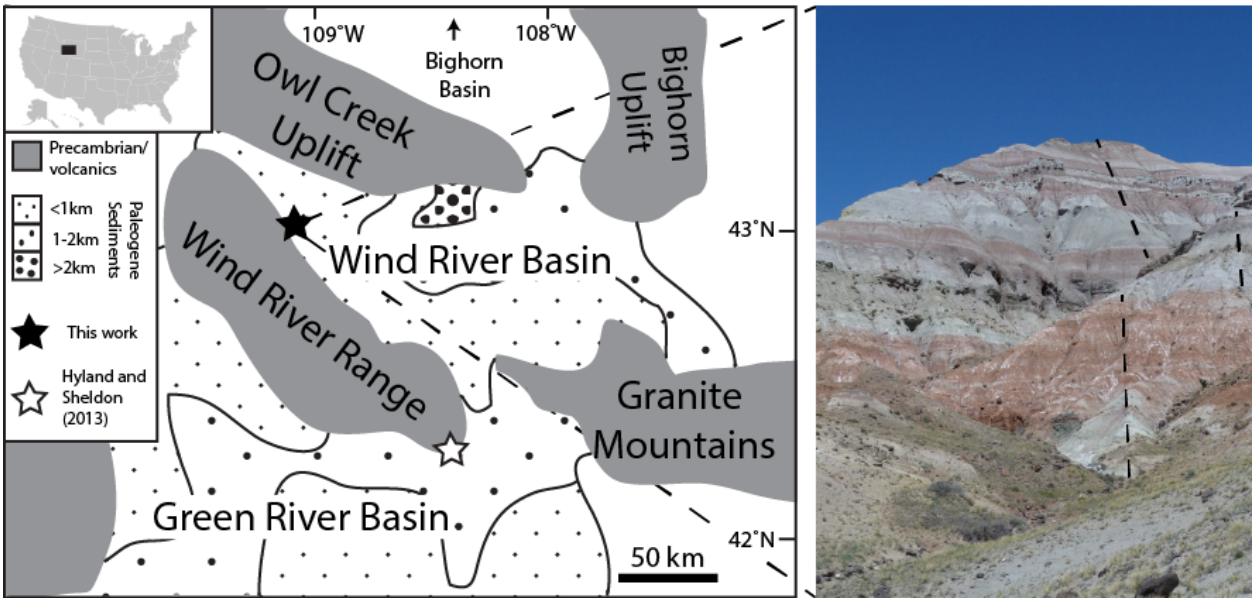

Figure 4.1 Schematic map of southwestern Wyoming. Identified sites include in the Wind River (this work) and Green River Basins (Hyland and Sheldon, 2013) with thickness of Paleogene sediments indicated (Smith et al., 2008). Black box in inset shows area of the United States depicted in full map. Image at right is the top ~100 m of site 2DB, and dashed lines indicate measured section.

4.2 METHODS

Sites 1DB and 2DB (Figure 4.1) were selected to include paleosols that were part of Fan et al.'s (2011) lithologic and isotopic record of the Wind River Formation. The sites are ~1 km apart and are well correlated through laterally continuous marker beds with conserved pedogenic features, overall stratigraphic sequence comparison (Figure 4.2), and comparable carbon isotopic

and whole-rock geochemical records between individual paleosols. The age of the integrated section is known fairly precisely (53.2–50.7 ± 0.5 Mya; Clyde et al., 1994, 1997; Machlus et al., 2004; Smith et al., 2003, 2008), and the ages of individual paleosols were determined based on interpolated sedimentation rates (~120 m Ma^{-1}), which were tied to biostratigraphic boundaries (e.g., Stucky, 1984; Clyde et al., 1997) due to a lack of magnetostratigraphic or detrital zircon tie points (Fan et al., 2011). The Wasatchian Wa6-Wa7 (Lost Cabinean–Lysitean) NALMA boundary can be correlated to a roughly 10 m interval at a stratigraphic height of ~50 m within this section (Figure 4.2; Stucky, 1984). As a result, individual paleosol ages can be resolved to within roughly 40–80 kyr based on fossil locality correlations to NALMA boundaries (±41 kyr; e.g., Stucky, 1984; Clyde et al., 1997, 2001), and on paleosol degree of development age models (Bt horizon thickness and carbonate nodule diameters as proxies for paleosol formation duration; e.g., Sheldon and Tabor, 2009).

Paleosol profiles were identified amongst other sedimentary facies by pedogenic features including horizonation, color, and burrowing or root traces (e.g., Mack et al., 1993), and they were described and sampled throughout depth profiles and for significant pedogenic features. All of the paleosols were trenched to a depth of at least 20 cm before sampling to minimize the risk of contamination from modern surface weathering or root material. We identified 83 individual paleosols throughout the two stratigraphic sections, and the sections were combined to form an integrated temporal record. Paleosol characterizations, quantitative paleoclimatic estimates, and ecological reconstructions were made from this integrated record based on four independent proxies: (1) field measurements and qualitative facies descriptions; (2) whole-rock geochemical properties, such as the degree of chemical weathering; 3) the stable isotopic composition of

carbon ($\delta^{13}C$) from pedogenic carbonates and preserved organic matter; and (4) phytolith assemblage compositions.

4.2.1 Whole-rock geochemistry

Major-element compositions of whole-rock samples (n = 63) from selected paleosol depth profiles (all well-developed soils) were determined using X-ray fluorescence (XRF) analysis at ALS Chemex Laboratory in Vancouver (BC), Canada, where average analytical uncertainty of major elements from XRF analyses is 0.001%, and duplicate analyses had a mean standard deviation of 0.11%. Profile compositions were used as inputs for climofunctions derived by Sheldon et al. (2002), including estimates of precipitation (mean annual precipitation [MAP]), temperature (mean annual temperature [MAT]), and long-term weathering (ΔW; Sheldon and Tabor, 2009). Major-element compositions of Ti and Al (Ti/Al ratio) were used for provenance analysis, because the conservative nature of both elements within a soil profile and source variability of Ti allow us to identify major changes in sediment sources (Sheldon and Tabor, 2009). Each proxy has been applied to soils of varying type and age (e.g., Driese and Ober, 2005; Hembree and Nadon, 2011), and all have been used extensively in reconstructing the Cenozoic climatic history of North America (e.g., Kraus and Riggins, 2007; Takeuchi et al., 2007; Sheldon, 2009).

The relationship of MAP to the chemical index of alteration without potassium (CIA – K; Maynard, 1992) is given by the following function:

$$\text{MAP (mm yr}^{-1}) = 221.1e^{0.0197(\text{CIA} - \text{K})} \quad (4.1)$$

where the standard error is ±182 mm yr^{-1}, and R^2 = 0.72 (Sheldon et al., 2002). This MAP proxy is based on the observation that modern soils that receive higher MAP display greater chemical weathering, and this relationship has been robustly compared to independent paleoprecipitation

proxies (e.g., paleobotanical and other paleosol estimates; Sheldon et al., 2002; Retallack, 2007). This proxy cannot be applied to paleosols with inherited carbonate (limestone parent), paleosols on hillslopes, laterites, or Vertisols (Sheldon et al., 2002; Nordt and Driese, 2010), but given that there is no evidence of any of these features at either site (Table 4.1), such complications can be discounted.

The relationship of long-term chemical weathering to the chemical index of alteration (CIA) is given by the following function:

$$\Delta W = \mathrm{CIA}_x - \mu\mathrm{CIA} \qquad (4.2)$$

where ΔW is the standard deviation between CIA in an individual paleosol (CIA_x) and mean chemical weathering for the entire sequence (μCIA), and ΔW is expressed as a three-point running average. This proxy is based on the correlation between trends in long-term chemical weathering and factors such as changes in precipitation, temperature, and seasonality, which affect rates of pedogenesis and have been robustly applied to most soil types, including all of those described for our sites (e.g., Sheldon, 2009; Retallack et al., 2011; Sheldon et al., 2012).

The relationship of MAT to the degree of salinization (*S*; Sheldon et al., 2002) is given by the following function:

$$\mathrm{MAT}\ (^{\circ}\mathrm{C}) = -18.5\ (S) + 17.3 \qquad (4.3)$$

where the standard error is ±4 °C, and $R^2 = 0.37$ (Sheldon et al., 2002). This MAT proxy is based on the observation that soils in regions with low MAT tend to more readily accumulate salts (K, Na; Sheldon et al., 2002). While this index can be used to quantify paleotemperature values, we interpret it primarily as an indicator of the degree and vector of change rather than as a purely quantitative proxy. Recent work has shown that while in some cases reconstructed values are difficult to reconcile with other lines of evidence (predicting lower absolute MAT values than

estimates from paleobotanical assemblages and evaporitic deposits), changes in salinization closely follow direction and magnitude of temperature trends observed in other proxies (e.g., Sheldon, 2009).

Table 4.1 Descriptions of major pedotypes in the Wind River Formation.

Pedotype name[a] (Soil Order[b])	Generalized description (Approximate age[c])	Site 1DB[d]	Site 2DB[d]
Red Hills (Alfisol)	Root traces, some eluvial development (Bt); (~10^4 years)	7	27
Torrey Lake (gleyic Alfisol)	Root traces, significant argillic development (Bt), redoximorphic features (Bg); (~10^5 years)	11	22
Table Mountain (calcic Alfisol)	Root traces, some eluvial development (Bt), carbonate-bearing horizon (Bk); (~10^4 years)	2	2
East Fork (Inceptisol)	Colored horizon (Bw) and variable texture, usually contains root traces; (~10^3 years)	5	7
	Total	25	58
	Section Height	122m	301m

[a] Pedotype names are assigned based on local geographic markers.
[b] Soil Orders based on taxonomy of the USDA (1999) and Mack et al. (1993).
[c] Approximate ages based on average time of soil type development (Retallack, 2001).
[d] Number of paleosols of each type at this site.

4.2.2 Stable isotope analysis

We performed carbon stable isotopic analyses of pedogenic carbonate nodules, organic matter occluded in nodules, and organic root traces for $\delta^{13}C_{cc}$ and $\delta^{13}C_{org}$ compositions (n = 35). Carbonate samples (n = 5) were thin sectioned and spot sampled for micritic calcite, which was then analyzed using a ThermoFinnigan MAT 253 isotope ratio mass spectrometer with a KielIV autosampler at the University of Michigan. Results are reported in per mil (‰) relative to the Vienna Peedee belemnite (VPDB) standard and were calibrated using NBS 18 and 19, with analytical uncertainty of less than 0.1‰ (2σ). Nodule and bulk soil samples from the full stratigraphic range (Figure 4.2) were cleaned in methanol to remove modern carbon, and nodules were dissolved in dilute HCl (7%) to isolate occluded organic matter. Organic root trace samples were also treated with dilute HCl (5%) to remove detrital carbonate, and both types of samples

were powdered and weighed into tin capsules, which were then analyzed using a Costech elemental analyzer attached to a Finnigan Delta V+ isotope ratio mass spectrometer at the University of Michigan. Results are reported in per mil (‰) relative to the VPDB standard and were calibrated using International Atomic Energy Agency (IAEA) sucrose and caffeine standards. Analytical uncertainty for these measurements was also maintained at less than 0.1‰ (2σ). Carbon isotope compositions were used as a high-resolution carbon isotope stratigraphy of this time period, and as a comparison point to determine whether similar records from carbonates in this section may have been affected by diagenesis (e.g., Fan et al., 2011). To facilitate comparison, organic carbon ($\delta^{13}C_{org}$) values were translated to carbonate ($\delta^{13}C_{cc}$) values using a conservative estimate of average enrichment (respiration plus calcite precipitation) of carbonate relative to preserved organic matter (+15.5‰; Cerling and Quade, 1993; Koch, 1998). For the limited number of profiles where both pedogenic carbonate and organic matter were available, material was used to estimate atmospheric pCO_2 using the paleobarometry equation of Cerling (1984; Ekart et al., 1999):

$$\mathrm{pCO_2\ (ppmv)} = Sz\left(\frac{\delta^{13}Cs - 1.0044*\delta^{13}Cr - 4.4}{\delta^{13}Ca - \delta^{13}Cs}\right) \qquad (4.4)$$

where S_z is calculated based on MAP values (Cotton and Sheldon, 2012), $\delta^{13}C_s$ is pedogenic carbonate values corrected for temperature dependence (Romanek et al., 1992), $\delta^{13}C_r$ is organic carbon values (Retallack, 2009), $\delta^{13}C_a$ is estimated atmospheric carbon compositions (Tipple et al., 2010), and error estimates were calculated using Gaussian error propagation (Retallack, 2009).

4.2.3 Phytoliths

Quantitative counts of phytoliths (plant silica bodies) have been widely applied for reconstructing records of Cenozoic vegetation and ecological change (e.g., Strömberg, 2005;

Zucol et al., 2010; Miller et al., 2012). Samples for phytolith extraction were collected from the top 10 cm of paleosol A horizons (n = 16) across the full temporal range of both stratigraphic sections (Figure 4.2). Samples were processed using the methodology of Strömberg et al. (2007), wherein 1–2 g of homogenized material is disaggregated via dissolution in dilute (10%) HCl and sieved through 250 µm and 53 µm sieves. Samples were also cleaned of organic material using a concentrated solution of HNO_3 and $KClO_3$, and finally separated via zinc bromide ($ZnBr_2$) heavy liquid floatation (2.38 g cm^{-3}) to isolate the biosilica fraction. Isolates were then mounted on slides using Cargille Meltmount 1.539 and analyzed and photographed using a Leica petrographic microscope at a range of magnifications (400–1000×). Phytoliths were categorized by plant functional group based on morphotypes defined by Strömberg (2003, 2005), and assemblage composition was calculated as a fraction of total diagnostic morphologies, where each sample contained >200 diagnostic counts. Specific morphotypes have a counting error of ~8%; however, broad-category vegetation assemblage compositions used for environmental interpretations such as these have smaller total counting error, generally <2% (e.g., Strömberg, 2002).

4.3 RESULTS

4.3.1 Pedology

All of the sediment at both DB sites was fluvially derived, as evidenced by abundant coarse-grained channel deposits with laterally variable erosive surfaces and other depositional features like cross-bedding and lateral grading. Provenance tests by Fan et al. (2011) and the Ti/Al ratio of paleosol depth profiles through time (e.g., Figure 4.2; Appendix C1) confirm a constant spatiotemporal source of clastic material, and no apparent removal of Ti or Al. While

none of this channel material exhibited evidence of pedogenesis, depositional systems like this fluvial margin of the Wind River Basin are superb locations for the burial of intact paleosols; channel-distal floodplain paleoenvironments at 1DB and 2DB have preserved 83 distinct paleosols throughout the full temporal span of these stratigraphic sections, with 25 paleosols at site 1DB (~1 paleosol per 4.9 m) and 58 paleosols at site 2DB (~1 paleosol per 5.2 m). In addition to similar rates of deposition and pedogenesis at both sites, paleosol characteristics are conserved across the landscape in identifiable assemblages with features such as color, textural horizonation, ped structures, organic root traces, rhizohaloes, gleying, clay skins/slickensides, iron-manganese nodules, and rare pedogenic carbonate nodules (Figure 4.3).

Pedogenic features were grouped into distinct pedotypes based on the taxonomic classification schemes of modern soils (USDA Soil Survey Staff, 1999) and paleosols (Mack et al., 1993), and these are detailed in Table 4.1. The four primary pedotypes include: the Red Hills Alfisol, characterized by its red color, significant root traces (rhizohaloes), and moderate development of a clayey Bt horizon; the Torrey Lake gleyic Alfisol, which is characterized by its dark-red/purple color, significant root traces and preserved root material, redoximorphic features like iron-manganese nodules and gleying, and the development of thick clayey Bt horizons; the Table Mountain calcic Alfisol, which is characterized by its red color, minor root traces (rhizohaloes), limited development of a clayey Bt horizon, and the variable development of a calcic Bk horizon (primarily dispersed carbonate); and the East Fork Inceptisol, which is characterized by its orange/light-red color, minor root traces (rhizohaloes), and variable textural maturity. The name of each pedotype was assigned based on local landmarks.

Each of the four pedotypes occurs roughly an equal number of times between the two sites (when scaled for section thickness) and commonly occurs contemporaneously. The

common incidence of paleosols of similar type (Figure 4.2; Table 4.1) indicates that the environments in both localities, and their relationship to the fluvial distributary system, were shared (e.g., Kraus, 1999; Hamer et al., 2007; Weissmann et al., 2010). While these environments were spatially stable, the temporal record indicates significant changes in pedotype during a defined interval from roughly 51.6 through 51.1 Mya. During this interval, both sites exhibit an increased incidence of paleosols, and specifically of the Torrey Lake pedotype (Figure 4.2), which is indicative of more significant weathering and conditions conducive to increased pedogenesis, such as floodplain saturation and heightened biotic influence (e.g., burrowing and significant vegetation).

Pedotype descriptions and pedological analysis can be complicated by diagenetic processes such as burial compaction, postburial oxidation, chemical alteration, and the precipitation of diagenetic minerals (Retallack, 1991). Sediments from this section indicate little in the way of burial compaction, as ichnofossils and other pedogenic features show no evidence of shortening, and structural relationships within this part of the basin indicate that overlying sediment loads were minimal (<1 km; Smith et al., 2008). Similarly, paleosols at these sites show little evidence of postburial oxidation, as many paleosols preserve in situ organic carbon root traces. Postburial chemical changes within paleosols are slightly more difficult to discern, but we assume that little bulk alteration has taken place based on the fact that most geochemical depth profiles of paleosols within these sections follow trends observed in modern soils (Figure 4.2; e.g., Maynard, 1992). However, these sediments do exhibit the possibility of minor diagenesis in the form of altered and re-precipitated carbonate observed in diffuse concretions and sparry veins within some of the studied paleosol profiles (Figure 4.3). This evidence of diagenesis presents a problem for the analysis of the stable isotopic composition of carbon and oxygen from

carbonates within this section, as field observations of such features indicate that formerly pedogenic features like carbonate nodules may have been altered beyond the point of analytical usefulness, a hypothesis we tested through the analysis of the carbon isotopic composition of preserved organic materials, which would not be subject to such chemical alteration.

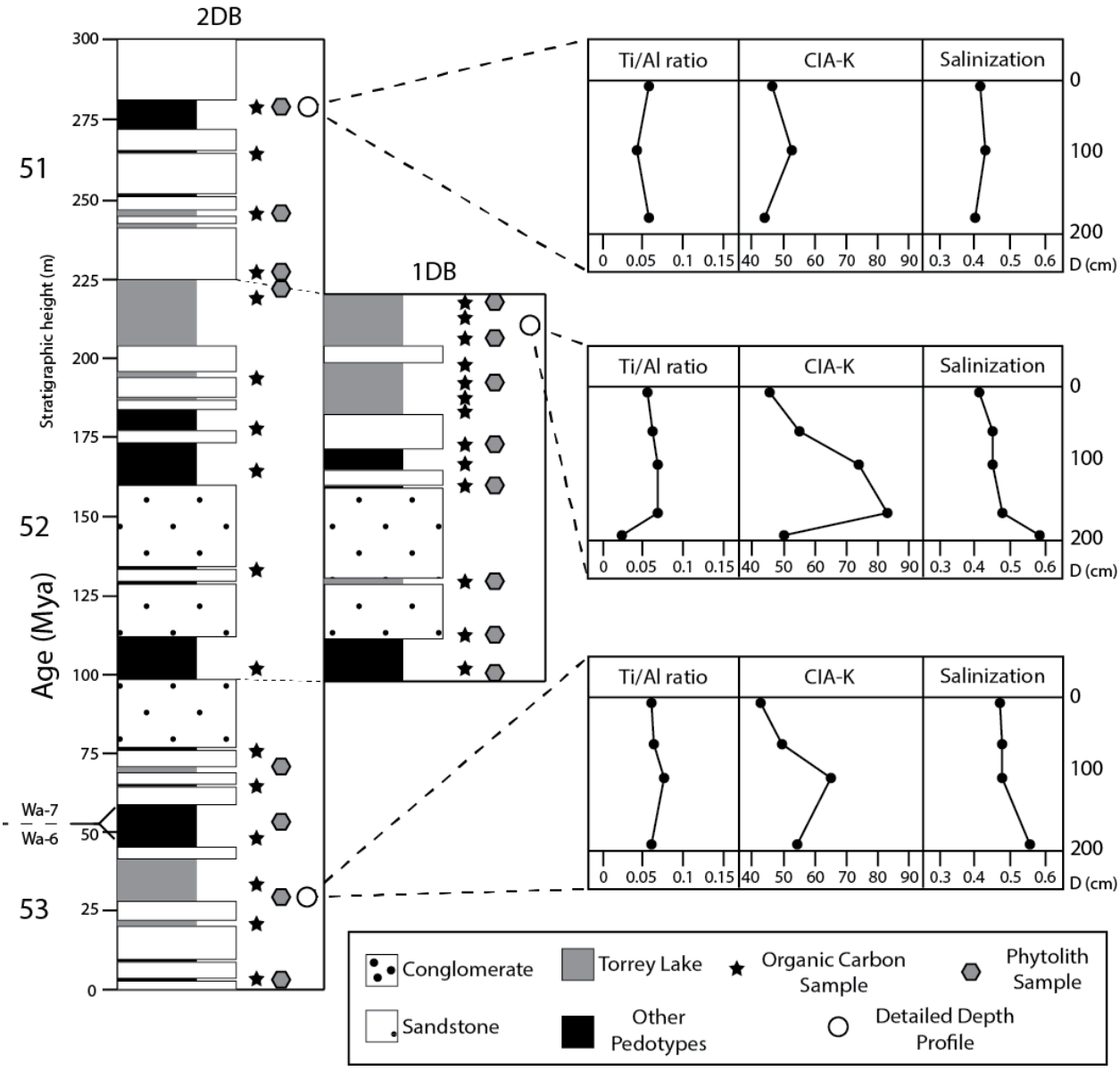

Figure 4.2 Stratigraphy of sites 1DB (right) and 2DB (left) with major lithologies/pedotypes. Sample levels and types are given with symbols next to corresponding stratigraphy. Detailed geochemical depth profiles including Ti/Al ratios, CIA–K, and salinization curves are provided for indicated paleosols.

4.3.2 Precipitation

Proxy values for paleoprecipitation (mean annual precipitation; MAP) derived from geochemical climofunctions based on the elemental ratios (CIA – K) of the eluvial Bt horizons of paleosols exhibited a range of values from 352 to 1152 mm yr^{-1} (Figure 4.4), with a mean value of 635 mm yr^{-1} (σ = 162 mm yr^{-1}). Physical evidence from the sampled paleosols justifies such a range, with features like limited horizonation and carbonate-bearing horizons in paleosols that indicate low MAP values, and well-developed horizons and saturation features (gleying, iron-manganese nodules) in soils that indicate higher MAP values (Figure 4.2 and Figure 4.3; Table 4.1). MAP values display a distinct trend through time, with stable lower MAP values (~400–800 mm yr^{-1}) throughout the section that are interrupted by a rapid rise to, and decline from, a period of higher MAP values (>900 mm yr^{-1}) between ca. 51.4 and 51.1 Mya (Figure 4.4). This period of higher precipitation also corresponds to the previously described interval of increased soil development and increased incidence of the Torrey Lake pedotype (Table 4.1).

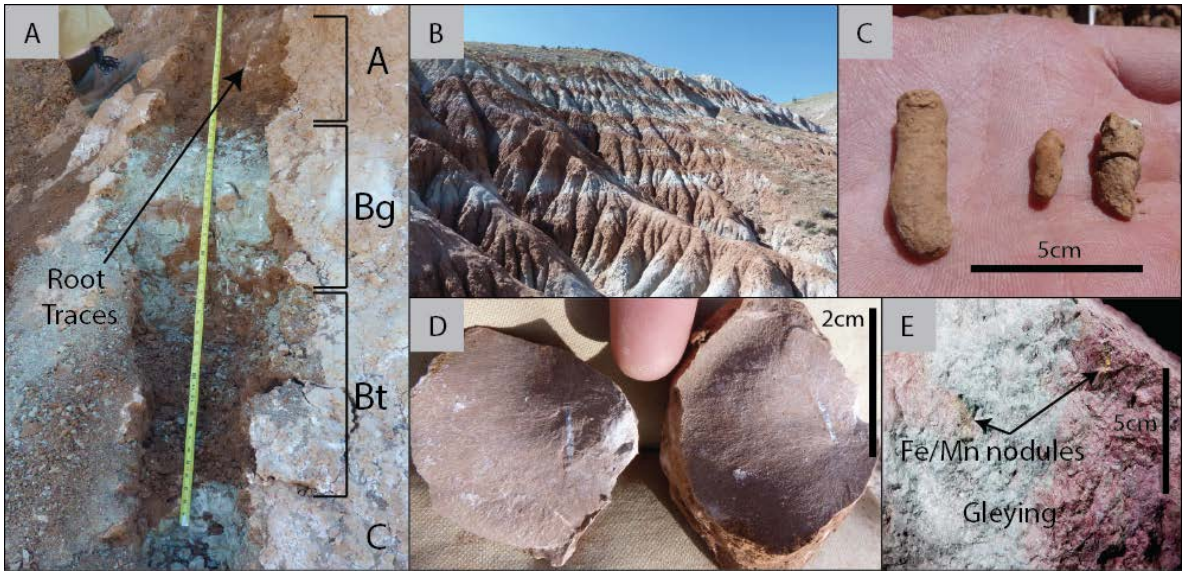

Figure 4.3 Common outcrop features from sites 1DB and 2DB: (A) Torrey Lake–type paleosol with soil horizons labeled; (B) sequence of stacked paleosols (~15 m of section); (C) infilled burrows from soil A horizon; (D) carbonate "nodule" with sparry veins; and (E) redoximorphic features (iron-manganese nodules and gleying).

4.3.3 Weathering

Proxy values for relative long-term weathering trends (ΔW) derived from geochemical climofunctions based on the elemental ratios (CIA) of the eluvial Bt horizons of paleosols exhibited a range of values from -23.1 to +20.5 (Figure 4.4), with a standard deviation of 9.2. While these absolute values have little meaning, the timing of trends within this proxy system is useful for identifying periods of change in the weathering regime (and associated drivers like precipitation and temperature; e.g., Sheldon et al., 2012); here, ΔW values show a distinct increase to a period of higher weathering rates between 51.4 and 51 Mya, contemporaneous with the previously described increases in MAP (Figure 4.4) and local changes in dominant pedotype.

4.3.4 Temperature

Proxy values for paleotemperature (MAT) derived from geochemical climofunctions based on the elemental ratios (salinization) of the eluvial Bt horizons of paleosols exhibited a range of values from 6.8 to 10.7 °C (Figure 4.4), with a mean value of 8.9 °C (σ = 1.0 °C). These MATs correspond to salinization values from 0.36 to 0.58, with a mean value of 0.46 (σ = 0.05; Appendix C1). Though the absolute MAT values from salinization can be ambiguous and are prone to underestimation (e.g., Sheldon, 2009), the robustness of trends in salinization is important; MAT values also display a distinct trend through time, with values rising to a peak period of high MAT values (>10 °C) at ca. 51.7 Mya, followed by a general stabilization of temperatures at this higher range (Figure 4.4). The onset of this period of higher temperatures slightly precedes (~0.3 Ma) the previously described intervals of increased precipitation, weathering, and pedotype changes (Figure 4.4), but it is otherwise contemporaneous.

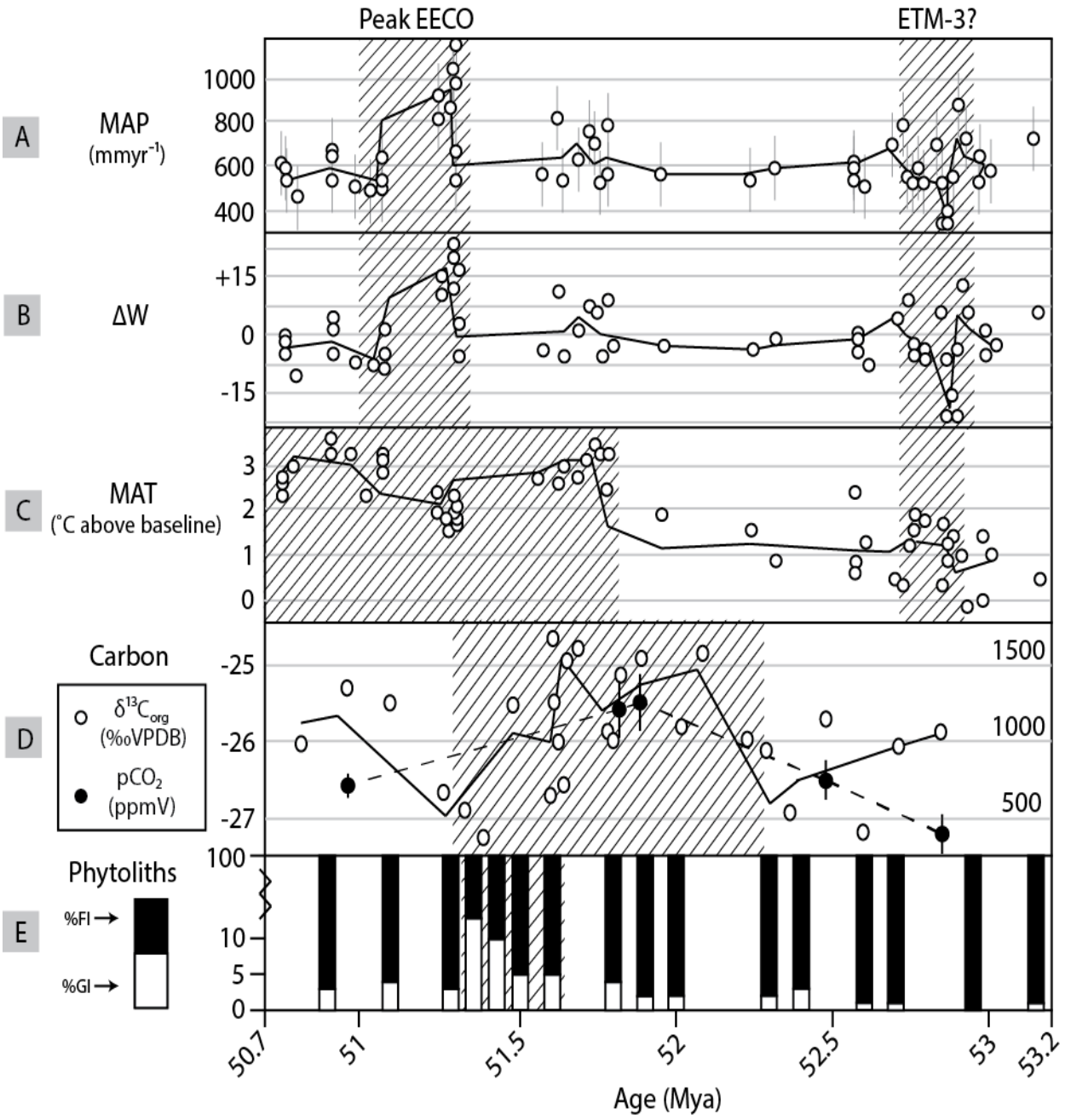

Figure 4.4 Integrated climatological and ecological proxy data from sites 1DB and 2DB: (A) mean annual precipitation (MAP) values given in open circles, error bars are ±182 mm yr^{-1}; (B) relative weathering rate (ΔW), where a positive value indicates an increase in weathering; (C) mean annual temperature (MAT) above early Eocene baseline (absolute error is ±4 °C); (D) δ^{13}Corg values given in open circles (error is ±0.1‰; less than the size of the data points), and estimated atmospheric pCO_2 values given in filled circles (error indicated by vertical lines, scales with Gaussian error propagation); and (E) phytolith assemblage major % compositions (error is ~±2%), where black portion represents forest indicators (FI) and white portion represents grass indicators (GI). All trend lines are given as 3 point running averages, and shaded boxes represent periods of significant change. EECO—Early Eocene Climatic Optimum; ETM—Eocene Thermal Maximum; VPDB—Vienna Peedee Belemnite.

4.3.5 Carbon record

Stable isotopic measurements of carbon from preserved organic matter ($\delta^{13}C_{org}$) exhibited a range of values from -28‰ to -24.2‰ (VPDB; Figure 4.4; Appendix C2), with a mean value of -25.8‰ (σ = 1.0‰). With assumed average enrichment from organic carbon to pedogenic carbonate (Cerling and Quade, 1993; Koch, 1998), extrapolated values result in a $\delta^{13}C_{cc}$ range of -12.5‰ to -8.7‰ (VPDB) for carbonate formed in equilibrium with the preserved organic matter, with a mean value of -10.3‰, while measured $\delta^{13}C_{cc}$ values from pedogenic nodules range from -9.5‰ to -7.3‰ (VPDB; Appendix C2). Measured $\delta^{13}C_{org}$ and $\delta^{13}C_{cc}$ values resulted in estimates of atmospheric pCO_2 ranging from 350 to 1265 ppmv, with average error between 120 and 355 ppmv. Carbon isotopic values displayed a distinct trend through time, with a >2‰ shift toward more enriched (higher) isotopic values between 52.3 and 51.3 Mya, concurrent with a 2–3× increase in estimated atmospheric pCO_2 (Figure 4.4D). The onset of the shift toward higher carbon isotopic values and increased atmospheric pCO_2 occurs ~0.5 Ma before any of the other described climatic/environmental changes (MAP, MAT, etc.), though its full extent (and peak value) overlaps with the time period of change identified by each of those proxies (Figure 4.4).

4.3.6 Phytolith record

In total, 16 paleosol samples within this section yielded enough phytolith material for quantitative phytolith analysis (>200 diagnostic bodies). The overall phytolith assemblage contained 15 diagnostic morphotypes and 6 nondiagnostic or nonphytolith (diatoms, sponges) morphotypes (Appendix C3; Figure 4.5). Diagnostic morphotypes included the compound groups POOID, PACCAD, GRASS-D, DICOT, FI-GEN, CONI, and PALM, which were collapsed into the functional groups of forest, or closed ecosystem, indicators (FI), and grass, or

open ecosystem, indicators (GI) after Strömberg et al. (2007). FI compound groups included DICOT, FI-GEN, CONI, and PALM, while GI compound groups included POOID and PACCAD (e.g., Strömberg et al., 2007), and the group GRASS-D was excluded from reconstruction calculations due to known production biases related to moisture availability (e.g., Strömberg, 2003). Assemblages averaged 3.7% grass indicators, with a standard deviation of 3.4% (Appendix C3), and thus are dominantly forest-type vegetation. However, a peak period from ca. 51.6 to 51.3 Mya includes a group of sample assemblages with between 5% and 13% GI (Figure 4.4), which is significantly above the average % GI for the periods both before and after this event (~2.6% GI). This period coincides roughly with the span between the initiation of rising MAT and rising MAP, as shown by the combined records (Figure 4.4).

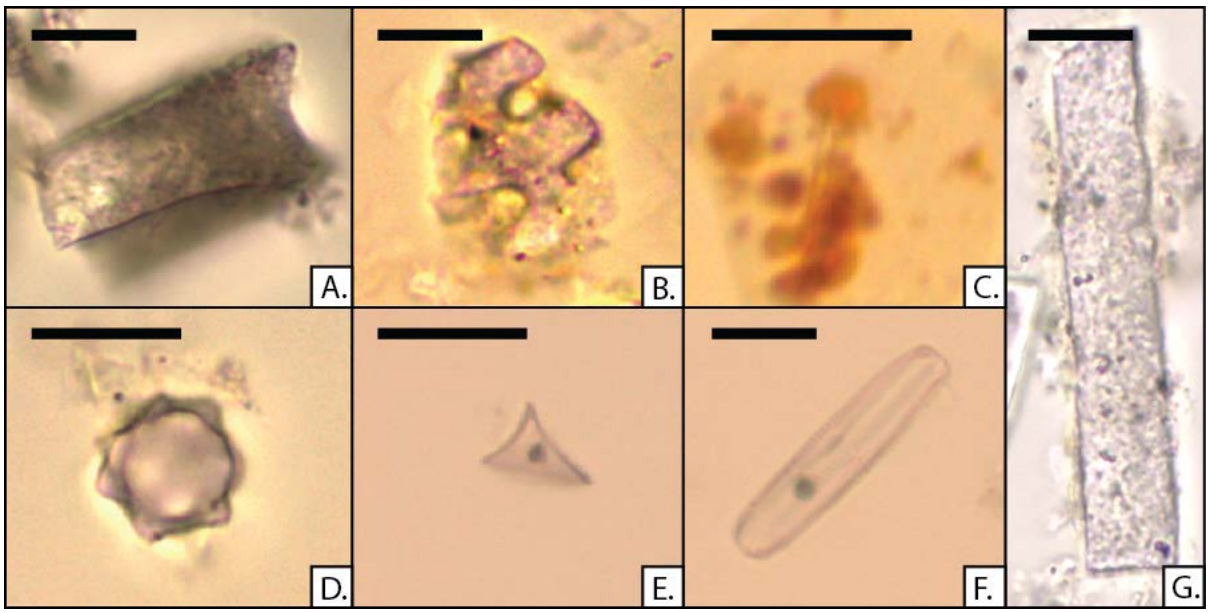

Figure 4.5 Phytolith plates for common morphotypes from the early Eocene Wind River Formation including: A) faceted rectangular block (Blo-3; 1DB-76), B) mesophyll bodies (M-4; 1DB-37), C) tiny pink spheres (Cl-4; 1DB-76), D) echinate sphere (Clm-2; 1DB-68), E) conical rondel (Co-2; 1DB-76), F) diatom frustule (Diat; 1DB-37), and G) Md elongate (Elo-18; 1DB-68). Morphotypes in plates A, B, C, D, and G are characterized as forest indicators (FI), while the morphotype in plate E is characterized as a grass indicator (GI) and the morphotype in plate F is characterized as an aquatic indicator. Black bars in each image are ~5 μm.

4.4 DISCUSSION

4.4.1 Climate change

4.4.1.1 Early Eocene Climatic Optimum

Early Eocene Climatic Optimum records characterize the event as a long-term atmospheric pCO_2 and temperature maximum, concurrent with major changes in local climate and ecology (e.g., Zachos et al., 2001). While this climate change is globally well documented in marine records, especially through isotopic proxies, few high-resolution climatic or ecological terrestrial records exist for the event. This new Wind River Basin terrestrial record fills a crucial gap in our understanding of how nonmarine systems respond to climate change events, and it agrees well with the magnitudes of change seen in previous temperature and biostratigraphic records (e.g., Zachos et al., 2001; Ivany et al., 2008). Terrestrial records, however, disagree with most marine records in terms of the timescale of the EECO event (Figure 4.6).

While differing responses between marine and terrestrial records of climatic events are not unexpected given the opposing or variable nature of many marine and terrestrial biogeochemical cycles (see section *4.4.5*) and differences in the dynamics of how these types of records are preserved and how they reflect climatic change (e.g., Retallack, 2001, 2007), the disagreements between records can be highly informative. We find a transient peak warming event within the overall warm climatic period (Figure 4.4C), whereas marine records indicate only a broad temperature maximum, suggesting that the previously accepted mechanism for driving the EECO (long-term changes in silicate weathering and volcanic activity, which should be recorded similarly in both marine and terrestrial settings; Zachos et al., 2001) may not accurately describe the dynamics of global change occurring between 52 and 50 Mya.

4.4.1.2 Precipitation and temperature

The described record of MAP across the EECO indicates a rapid increase of as much as 500 mm yr^{-1} starting at roughly 51.4 Mya (Figure 4.4). Unsurprisingly, given that localized weathering is highly dependent on changes in precipitation, the weathering record similarly shows a rapid increase in long-term weathering rate across this time interval (Figure 4.4). Changes in paleosol type also occur during this interval (Figure 4.2), where increased incidence of the Torrey Lake pedotype indicates a significant increase in saturation features caused by ponded floodplains and decreased drainage (Kraus and Aslan, 1993), which are also consistent with a rapid climatic shift to higher mean precipitation values (e.g., Retallack, 2007). In addition to being internally consistent, these moisture records agree well in terms of magnitude and response rate, both with other paleosol-based precipitation records from this time period (Figure 4.6; Krause et al., 2010; Hyland and Sheldon, 2013), and with modeled MAP changes resulting from atmospheric changes during the EECO event (Thrasher and Sloan, 2010).

The rapid increase in the MAT record occurs slightly before (<1 Ma) those seen in the MAP and weathering records (Figure 4.4). Many terrestrial records (e.g., Kraus and Riggins, 2007; Retallack, 2007; Hyland and Sheldon, 2013) display similar lags between these types of changes during major climatic events, often ascribed to increased temperatures leading to higher evaporation rates, which consequently cause elevated MAP and weathering values. Such elevated MATs during the EECO agree with marine proxy reconstructions (e.g., Zachos et al., 2001, 2008), but they are slightly lower than comparable terrestrial records (e.g., Greenwood and Wing, 1995; Fricke and Wing, 2004; Hren et al., 2010) in terms of both absolute MAT and the absolute magnitude of temperature change. However, the use of the salinization paleosol proxy for reconstructing MAT has been shown in previous work to underestimate absolute

temperatures (Sheldon, 2009), and measured salinization values (see section *4.3*; Appendix C1) nearly exactly match the range of salinization values and magnitude of temperature change produced by other work (e.g., Krause et al., 2010; Hyland and Sheldon, 2013) for the EECO. This previous work suggests that our MAT record from these paleosols is showing a robust pattern that is characteristic of the event, and that the range of absolute MAT in this record may more reasonably be expressed as ~9–17 °C, as calibrated from the combined salinization-oxygen isotopic record of Hyland and Sheldon (2013), which results in absolute temperatures and temperature changes that are more consistent with records from other terrestrial proxies (e.g., Greenwood and Wing, 1995; Chew, 2009) and model results (e.g., Thrasher and Sloan, 2009).

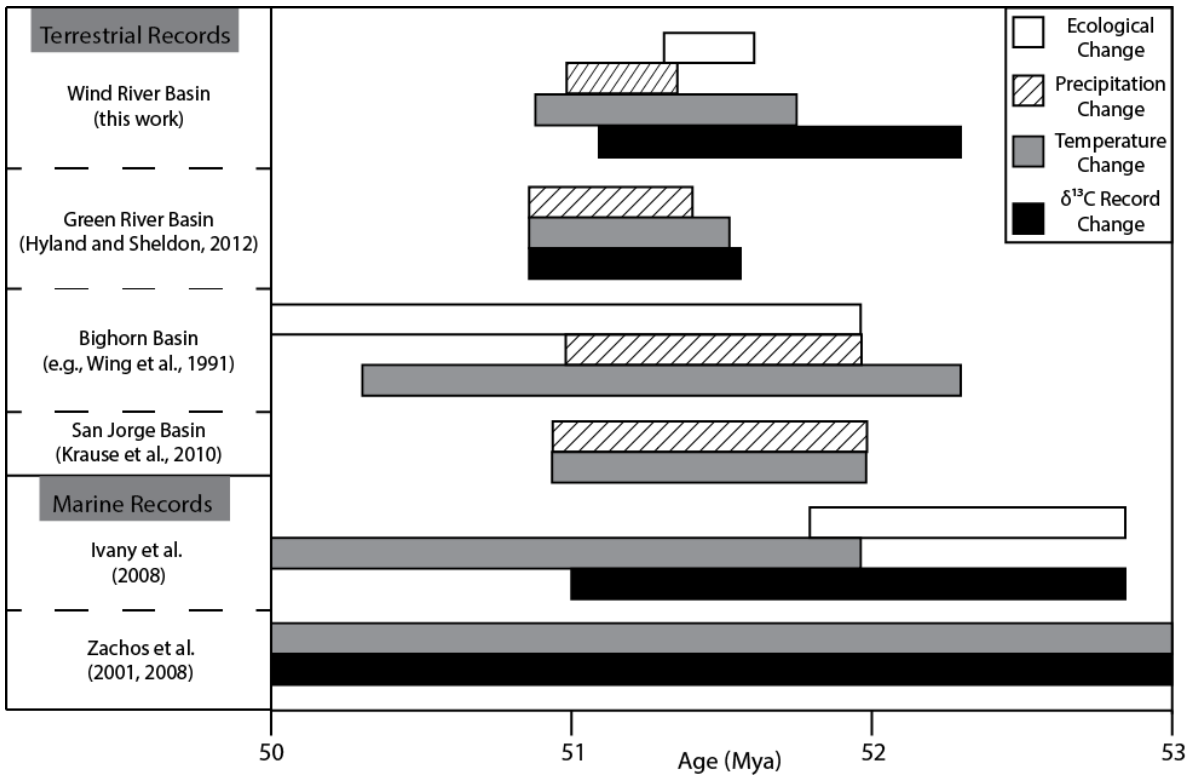

Figure 4.6 Comparison of major climatic and ecological records across the Early Eocene Climatic Optimum, including marine (Zachos et al., 2001, 2008; Ivany et al., 2008) and terrestrial (Wing et al., 1991; Greenwood and Wing, 1995; Krause et al., 2010; Hyland and Sheldon, 2013) records compared to this work. Boxes indicate time period over which proxy data indicate a major change in one (or more) of the following: carbon/atmospheric pCO_2 (black boxes), mean annual temperatures (gray boxes), mean annual precipitation (hatched boxes), or ecological conditions (white boxes) such as floral/faunal turnover.

Perhaps most importantly, the climatic record from the Wind River Basin agrees well with the contemporaneous record from the Green River Basin (Hyland and Sheldon, 2013) on the opposite side of the incipient Wind River Range in terms of the magnitude and duration of the EECO event, which indicates that this terrestrial record is capturing a truly global climate signal. If either of these records were purely local or regional, we would expect distinct responses on either side of the range (i.e., rain shadows or topographic temperature gradients, variable or lacking responses from one basin to another; Takeuchi et al., 2007), while instead both basins record a coherent response to the EECO.

4.4.1.3 Atmospheric pCO_2

Carbon isotopic records through the EECO exist for both marine (e.g., Zachos et al., 2001) and terrestrial (e.g., Hyland and Sheldon, 2013) environments. An isotopic record from carbonates collected from Wind River sections was previously published by Fan et al. (2011), who reported $\delta^{13}C_{cc}$ values that ranged from -3.8‰ to -9.5‰ (VPDB; Figure 4.7), which were translated into atmospheric pCO_2 values ranging from 900 to 2050 ppmv for the early Eocene. While these values are within the range of atmospheric pCO_2 originally predicted by Ekart et al. (1999) for the early Eocene, they are substantially higher than more recent revisions to the EECO record (e.g., ~400–1500 ppmv; Breecker et al., 2010; Smith et al., 2010; Beerling and Royer, 2011; Hyland and Sheldon, 2013), and they exhibit a temporal trend distinctly different from those records, and from our own organic carbon record and atmospheric pCO_2 reconstruction (Figure 4.4D). Despite this, the averaged atmospheric pCO_2 value from Fan et al.'s (2011) record that comes from the Wind River Formation (~900 ppmv) is within the range of values presented here (Figure 4.4D) and by others (Beerling and Royer, 2011).

Our carbon record is from measurements of the carbon isotopic ratio of preserved organic matter within paleosol profiles, which, unlike pedogenic carbonates, is unaffected by isotopic fractionation due to postburial diagenetic fluids and re-precipitation (Koch, 1998). By converting organic carbon values to the pedogenic carbon scale using the average carbonate precipitation from soil CO_2 values (+15.5‰; Cerling and Quade, 1993; Koch, 1998), we can directly compare our carbon record to that of Fan et al. (2011) (Figure 4.7) and others (Beerling and Royer, 2011; Hyland and Sheldon, 2013). These predicted carbonate values are significantly lower than those measured by Fan et al. (2011), and they display a different trend, with a >2‰ increase (rather than an ~1‰ decrease) in $\delta^{13}C$ during the period from 52.3 to 51.3 Mya. While specific $\delta^{13}C_{org}$ values exhibit some variability as a result of ecosystem heterogeneity (Figure 4.4D), the shift in the running average value indicates that the change in $\delta^{13}C_{org}$ values is a real trend (Figure 4.8). The difference between Fan et al.'s (2011) carbonate record and our organic carbon record (Figure 4.7) is likely a result of diagenetic resetting of the $\delta^{13}C_{cc}$ values of the pedogenic carbonates in the two sections, which is suggested by the sparry nature of most nodular carbonate (Figure 4.3D) and the widespread presence of secondary carbonate cement in many paleosols and channel deposits.

However, the trend in carbon isotopic values from our organic carbon record is robust, and it agrees with measured values from other pedogenic records of the event (e.g., Hyland and Sheldon, 2013). The approximate 2‰–3‰ shift toward higher carbon values is comparable to carbon record shifts seen in increases of 2–3× atmospheric pCO_2 (e.g., Cerling, 1992), which are consistent with changes seen in the few atmospheric pCO_2 values we were able to reconstruct (Figure 4.4D), and in other records of the EECO (e.g., Beerling and Royer, 2011; Hyland and Sheldon, 2013). Carbon isotopic shifts of this magnitude have also been attributed to transient

drying events (e.g., Kraus and Riggins, 2007) or to increased C_4 vegetation (e.g., Fox and Koch, 2004), but as our MAP and phytolith records show neither of those changes during this time period, we can attribute the change in the $\delta^{13}C$ record to the estimated 2–3× increase in atmospheric pCO_2 seen in Figure 4.4D.

4.4.2 Event timing and topographic implications

The sequence of climatic events exhibited by paleosol records through this period follows trends that are well established and appear both in modeling experiments of rapid climate change (Thrasher and Sloan, 2009) and in other terrestrial climate records (Hyland and Sheldon, 2013). As detailed in Figures 4.4 and 4.6, we show a rapid (~0.3 Ma) increase in atmospheric pCO_2 followed closely by a rapid increase in MAT, which in turn led to significant changes in evaporation rates and MAP (e.g., Thrasher and Sloan, 2010). Not only does this record follow expected patterns of terrestrial climate change for a rapid pCO_2 increase (e.g., IPCC, 2007), the magnitude of change described by each of these paleosol proxies agrees well with changes in other proxy records (e.g., Ivany et al., 2008; Zachos et al., 2008). While the described magnitudes agree with expected terrestrial change based on other records, the changes in the Wind River Basin disagree with previously published marine records in terms of timing. However, the identified EECO changes in our record, which identify a shorter (<1 Ma) and later (closer to 52–51 Mya) peak interval, agree well with other paleosol records from both North and South America (e.g., Figure 4.6; Krause et al., 2010; Hyland and Sheldon, 2013). These changes suggest a broad-scale difference in the timing of marine and terrestrial responses during the early Eocene, and they highlight the possibility that previously discussed causal mechanisms like weathering and volcanism are untenable due to their long response times (e.g., Zachos et al., 2001).

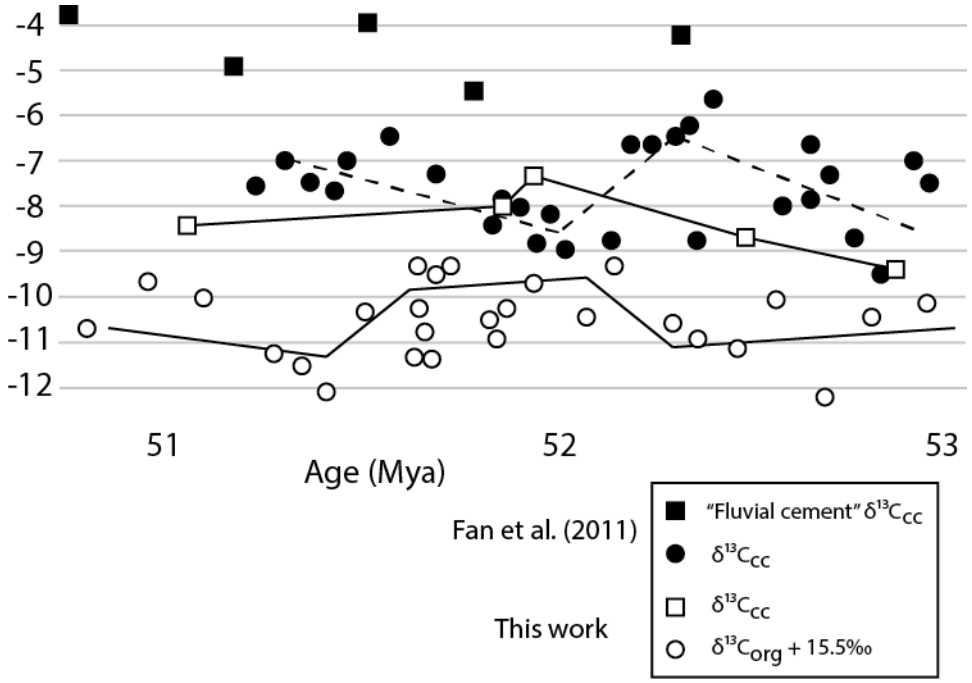

Figure 4.7 Comparison of $\delta^{13}C_{cc}$ from Fan et al. (2011) and extrapolated $\delta^{13}C_{cc}$ from this work. Note difference in the shape of running average trends and the overall offset between data sets. Previously published $\delta^{13}C_{cc}$ are not in equilibrium with $\delta^{13}C_{org}$ from the Wind River Basin, and likely many of the carbonate analyses represent diagenetically altered samples.

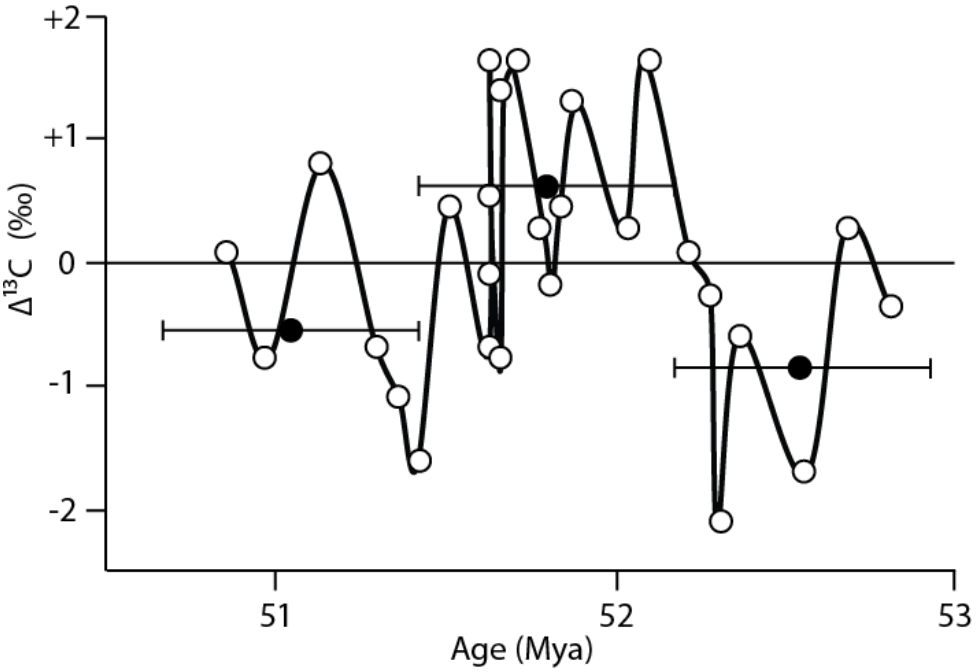

Figure 4.8 $\Delta^{13}C_{org}$ ($\delta^{13}C - \delta^{13}C_{mean}$) of paleosol carbon through time. Open circles indicate calculated values, while filled circles indicate mean value of 0.75 Ma bins (indicated by horizontal solid lines).

While terrestrial records of the EECO agree on short climatic and ecological response times, there is a slight offset in the timing of peak change (Figure 4.6) among sites in the Bighorn Basin (e.g., Greenwood and Wing, 1995), the Wind River Basin (this work), and the Green River Basin (e.g., Hyland and Sheldon, 2013). Local changes in MAT and MAP occurred earliest and most severely in the Bighorn Basin (e.g., Wing et al., 1991; Greenwood and Wing, 1995), followed temporally by the Wind River Basin (Fricke and Wing, 2004; this work), and finally the Green River Basin (Greenwood and Wing, 1995; Hyland and Sheldon, 2013). The resolution of age models in each of these localities does not allow for distinctions in terms of the exact spatiotemporal progression of this change (i.e., the precise age of event initiation in each locality), but based on the known ages and time spans of each record, the pattern of progressive north-south response is robust. Such a pattern of progressive response to the climatic events of the EECO (i.e., onset times progress north to south) suggests that sufficiently elevated Laramide/Front Range topography (e.g., Figure 4.1; Smith et al., 2008) may have created a local pattern of northeast-southwest atmospheric circulation (e.g., Thrasher and Sloan, 2010; Huber and Caballero, 2011) during the early Eocene, modulating the effects of global change caused by the EECO. This implies that by the early Eocene, Laramide topography in both western and central Wyoming had reached elevations high enough to alter regional atmospheric circulation and to control local climatic responses (e.g., Smith et al., 2008).

4.4.3 Eocene Thermal Maximum 3 (ETM-3)

In addition to recording the EECO, this high-resolution climatic record is long enough to include an earlier Eocene climatic event that may correlate to the transient ETM-3 event. In marine records, the ETM-3 spans roughly 52.8–52.5 Mya, and it is characterized by rapid temperature and carbon isotope excursions previously linked to high atmospheric pCO_2 (Zachos

et al., 2008; DeConto et al., 2012). During this same time period, terrestrial proxies from the Wind River Basin record a rapid excursion to higher temperatures (+1 °C), consequent with a decrease in precipitation (-200 mm yr^{-1}), all of which return to previous values within 0.3 Ma (Figure 4.4). This pattern is consistent with other records of ETM-3 (e.g., Wing and Harrington, 2001; Zachos et al., 2008; DeConto et al., 2012), and it fits well with terrestrial climatic and environmental responses to rapid carbon release events (e.g., Kraus and Riggins, 2007; Krause et al., 2010), which is an important verification of the robust link between our terrestrial record and other global records of early Eocene climate. While the ETM-3 event is briefly recorded in the Wind River Formation, its extent and magnitude are poorly characterized by this section and should be examined in more detail in other continental basins to confirm the nature of this earlier climatic shift in terrestrial settings.

4.4.4 Ecological change

Many records of ecological change during the Early Eocene Climatic Optimum exist from floral and faunal biostratigraphies on multiple continents (e.g., Wing et al., 1991; Zonneveld et al., 2000; Wilf et al., 2003). Such records highlight global ecological changes resulting from climate change during the EECO, and regional studies in continental North America have identified periods of rapid change (<1 Ma) in mammalian records (e.g., Alroy, 2000; Zonneveld et al., 2000; Chew, 2009) and vegetation (e.g., Wing et al., 1991; Wing and Harrington, 2001). The phytolith record (Figure 4.4) details a similarly short period of change (~0.5 Ma) in vegetation composition in western North America, and the time span and magnitude of this change agree well with other regional vegetation records and with land-cover model projections (e.g., Wing et al., 1991; Thrasher and Sloan, 2010). Ecological differences described by these terrestrial records are also contemporaneous with periods of climatic change

(Figures 4.4 and 4.6), confirming the suggested link between rapid climate change and significant floral and faunal turnover during the EECO (e.g., Zonneveld et al., 2000; Woodburne et al., 2009).

Due to the timing of vegetation composition change shown by the phytolith record, we suggest that such compositional changes may result specifically from the rapid increase in MAT, which occurs slightly before the increase in MAP (Figure 4.4). Periods of climate change involving increased MAT without a coupled change in MAP have been shown to increase habitat complexity and floral diversity (e.g., Woodburne et al., 2009), and to cause changes in faunal ranges or niche utilization (e.g., Alroy, 2000). The kind of floral shift indicated by the phytolith record exhibits similarly increased ecosystem complexity via the expansion of warm-adapted (C_3) tropical grasses, and it appears to agree well with other records of the early Eocene that describe a period of rapid floral diversification and ecological heterogeneity in concert with changes in climatic drivers like MAT and MAP (e.g., Wing and Harrington, 2001; Wilf et al., 2003; Woodburne et al., 2009).

4.4.5 Causes of terrestrial change

Based on paleosol proxy records from the Wind River and other terrestrial basins (Figures 4.4 and 4.6), it is clear that the sequence of climatic and ecological events that characterize the EECO on land is a transient response to a global driver of atmospheric pCO_2. The short timescales involved make it unlikely that reduced silicate weathering or increased volcanic emissions were responsible for elevated carbon inputs to the atmosphere, and the lack of a significant negative isotopic excursion in the carbon ($\delta^{13}C$) record suggests that the release and oxidation of a large source of methane (as invoked for other transient events like the

Paleocene-Eocene thermal maximum; e.g., Zachos et al., 2003) is also unlikely during the EECO.

Recent work has suggested that the rapid ventilation of dissolved carbon from large bodies of water such as oceans (Sexton et al., 2011) and major lacustrine systems (Whiteside et al., 2011) could provide a mechanism for the redistribution of appropriate amounts of carbon through the rapid release and subsequent sequestration of significant (as much as ~1500 Gt C; Jahren et al., 2001) isotopically enriched (relative to the atmosphere) pools. Such a mechanism fits well with this and other terrestrial records (Figure 4.6), where the only carbon isotopic signal results from increased atmospheric pCO_2 (Figure 4.4), and the timescales of change are quite short (<1 Ma). Importantly, the mechanism is also conducive to the more gradual changes seen within the marine carbon record (~2–3 Ma), as long-term decreases in carbon burial (evidenced by a gradual negative carbon isotope excursion in the marine record; e.g., Zachos et al., 2001) could be a result of the increased oceanic dissolution and storage of a significant carbon pool over time, providing a source for the subsequent rapid oxidation and ventilation of carbon that led to an atmospheric pCO_2 maximum during the EECO, as defined by major changes in the terrestrial record (Figure 4.6). Unlike changes in weathering or volcanism during the early Eocene (cf. Zachos et al., 2001), such a mechanism provides a single explanation for variation in marine and terrestrial climate responses through the EECO and, importantly, addresses the differences in timescale between marine and terrestrial records of the event.

These climatic changes and carbon record excursions could also have been exacerbated by a temperature feedback mechanism caused by the increased generation and expulsion of petroleum in major lacustrine and marine sedimentary basins that are known from the early Eocene climatic optimum (e.g., Kroeger and Funnell, 2012). Rapid changes in petroleum fluxes

can occur on very short timescales (<1 Ma) due to increased subsurface carbon burial and remobilization rates during times of climatic warming (Gu et al., 2011; Kroeger and Funnell, 2012), which cause further changes in atmospheric carbon fluxes and increases in surface temperatures, contributing to the rapidity of major warming events like the EECO.

The Early Eocene Climatic Optimum is a crucial part of understanding how climate has changed throughout the Cenozoic, and with little previous work on terrestrial responses to climate change, and much of the available terrestrial record in disagreement with causal mechanisms suggested by global marine records, more terrestrial records from other continents are needed (e.g., Wilf et al., 2003; Krause et al., 2010). Terrestrial records from North America appear to be converging on at least a regional/hemispheric record of the early Eocene (e.g., Figure 4.6; Greenwood and Wing, 1995), but further global coverage from paleosol and paleobotanical records will greatly illuminate whether this event had the widespread climatic and ecological effects that are suggested by this study. In addition to improving terrestrial records of the EECO, more work needs to be undertaken to discuss and confirm the mechanism of carbon sourcing to the atmosphere (e.g., Sexton et al., 2011; Whiteside et al., 2011) that appears to be the primary driver for many of the changes we discuss (Figures 4.4 and 4.6).

4.5 CONCLUSIONS

The paleomargin of the Wind River Basin, as defined by the Eocene Wind River Formation, was a fluvial distributary system characterized by channels and floodplain soil development. Paleosols preserved in this environment exhibit a variety of physical and geochemical characteristics and floral microfossil assemblages that provide a high-resolution and spatially robust record of climatic and ecological change during the Early Eocene Climatic

Optimum. Multiproxy records from these paleosols describe a short peak period of <1 Ma (~51 Mya) during which carbon isotopic enrichment (up to 2‰ higher) and elevated atmospheric pCO_2 (~2–3× increase), high MAT (up to 8 °C higher), increased MAP (up to 500 mm yr^{-1} higher), and shifts in floral assemblage composition (up to 10%) describe regional responses to EECO maxima. This record agrees well with other recent terrestrial records of the EECO, and along with these records may provide a detailed account of the ways in which topographically complex regions like western North America respond to global climatic events. Additionally, the rapidity of the climatic and environmental changes during the peak interval in this record suggests that the terrestrial response to the EECO was transient and may have resulted from short-term drivers like changes in oceanic carbon ventilation and basinal petroleum generation instead of long-term trends like volcanism and silicate weathering. A detailed insight into the causes, timescales, and terrestrial responses to events such as the Early Eocene Climatic Optimum may prove instrumental in fully understanding our climate system and its impact on biological processes.

REFERENCES CITED

Alroy, J., 2000, New methods for quantifying macroevolutionary patterns and processes: Paleobiology 26, 707–733.

Beerling, D.J., Royer, D.L., 2011. Convergent Cenozoic CO_2 history. Nature Geoscience 4, 418–420.

Breecker, D.O., Sharp, Z.D., McFadden, L.D., 2010. Atmospheric CO_2 concentrations during ancient greenhouse climates were similar to those predicted for A.D. 2100. Proceedings of the National Academy of Sciences of the United States of America, 107, 576–580.

Cerling, T.E., 1984. The stable isotope composition of modern soil carbonate and its relationship to climate. Earth and Planetary Science Letters 71, 229–240.

Cerling, T.E., 1992. Use of carbon isotopes in paleosols as an indicator of the pCO_2 of the paleoatmosphere: Global Biogeochemical Cycles 6, 307–314.

Cerling, T.E., Quade, J., 1993. Stable carbon and oxygen isotopes in soil carbonates, *in* Swart, P.K., et al., eds., Climate Change in Continental Isotopic Records. American Geophysical Union Geophysical Monograph 78, 217–231.

Chew, A., 2009. Paleoecology of the early Eocene Willwood mammal fauna from the central Bighorn Basin, Wyoming. Paleobiology 35, 13–31.

Clyde, W.C., Stamatakos, J., Gingerich, P.D., 1994. Chronology of the Wasatchian Land-Mammal Age (early Eocene): Magnetostratigraphic results from the McCullough Peaks section, northern Bighorn Basin, Wyoming. The Journal of Geology 102, 367–377.

Clyde, W.C., Zonneveld, J.P., Stamatakos, J., Gunnell, G.F., Bartels, W.S., 1997. Magnetostratigraphy across the Wasatchian/Bridgerian NALMA boundary (early to middle Eocene) in the western Green River Basin, Wyoming. The Journal of Geology 105, 657–670.

Clyde, W.C., Sheldon, N.D., Koch, P.L., Gunnell, G.F., Bartels, W.S., 2001. Linking the Wasatchian/Bridgerian boundary to the Cenozoic global climate optimum: New magnetostratigraphic and isotopic results from South Pass, Wyoming. Palaeogeography, Palaeoclimatology, Palaeoecology 167, 175–199.

Cotton, J.M., Sheldon, N.D., 2012. New constraints on using paleosols to reconstruct atmospheric pCO_2. Geological Society of America Bulletin 124, 1411–1423.

DeConto, R.M., Galeotti, S., Pagani, M., Tracy, D., Schaefer, K., Zhang, T., Pollard, D., Beerling, D.J., 2012. Past extreme warming events linked to massive carbon release from thawing permafrost. Nature 484, 87–91.

Driese, S.G., Ober, E.G., 2005. Paleopedologic and paleohydrologic records of precipitation seasonality from early Pennsylvanian “underclay” paleosols, U.S.A. Journal of Sedimentary Research 75, 997–1010.

Ekart, D.D., Cerling, T.E., Montanez, I.P., Tabor, N.J., 1999. A 400-million year carbon isotope record of pedogenic carbonate: Implications for paleoatmospheric carbon dioxide. American Journal of Science 299, 805–827.

Fan, M., DeCelles, P.G., Gehrels, G.E., Dettman, D.L., Quade, J., Peyton, S.L., 2011. Sedimentology, detrital zircon geochronology, and stable isotope geochemistry of the lower Eocene strata in the Wind River Basin, central Wyoming. Geological Society of America Bulletin 123, 979–996.

Fox, D.L., Koch, P.L., 2004. Carbon and oxygen isotopic variability in Neogene paleosol carbonates: Constraints on the evolution of the C_4 grasslands of the Great Plains, USA. Palaeogeography, Palaeoclimatology, Palaeoecology 207, 305–329.

Fricke, H.C., Wing, S.L., 2004. Oxygen isotope and paleobotanical estimates of temperature and $\delta^{18}O$-latitude gradients over North America during the early Eocene. American Journal of Science 304, 612–635.

Greenwood, D.R., Wing, S.L., 1995. Eocene continental climates and latitudinal temperature gradients. Geology 23, 1044–1048.

Gu, G., Dickens, G.R., Bhatnagar, G., Colwell, F.S., Hirasaki, G.J., Chapman, W.G., 2011. Abundant early Palaeogene marine gas hydrates despite warm deep-ocean temperatures. Nature Geoscience 4, 848–851.

Hamer, J.M., Sheldon, N.D., Nichols, G.J., Collinson, M.E., 2007. Late Oligocene–early Miocene paleosols of distal fluvial systems, Ebro Basin, Spain. Palaeogeography, Palaeoclimatology, Palaeoecology 247, 220–235.

Hembree, D.I., Nadon, G.C., 2011. A paleopedologic and ichnologic perspective of the terrestrial Pennsylvanian landscape in the distal Appalachian Basin, U.S.A. Palaeogeography, Palaeoclimatology, Palaeoecology 312, 138–166.

Hren, M.T., Pagani, M., Erwin, D.M., Brandon, M., 2010. Biomarker reconstruction of the early Eocene paleotopography and paleoclimate of the northern Sierra Nevada. Geology 38, 7–10.

Huber, M., Caballero, R., 2011. The early Eocene equable climate problem revisited. Climate of the Past 7, 603–633.

Hyland, E., Sheldon, N.D., 2013. Coupled CO_2-climate response during the Early Eocene Climatic Optimum. Palaeogeography, Palaeoclimatology, Palaeoecology 369, 125–135.

Intergovernmental Panel on Climate Change (IPCC), 2007, Fourth Assessment Report: Climate Change (AR4): Geneva, Switzerland, IPCC, 104 p.

Ivany, L.C., Lohmann, K.C., Hasiuk, F., Blake, D.B., Glass, A., Aronson, R.B., Moody, R.M., 2008. Eocene climate record of a high southern latitude continental shelf: Seymour Island, Antarctica. Geological Society of America Bulletin 120, 659–678.

Jahren, A.H., Arens, N.C., Sarmiento, G., Guerrero, J., Amundson, R., 2001. Terrestrial record of methane hydrate dissociation in the Early Cretaceous. Geology 29, 159–162.

Keefer, W.R., 1965. Stratigraphy and Geologic History of the Uppermost Cretaceous, Paleocene, and Lower Eocene Rocks in the Wind River Basin, Wyoming. U.S. Geological Survey Professional Paper 495-A, 77 p.

Koch, P.L., 1998. Isotopic reconstruction of past continental environments. Annual Review of Earth and Planetary Sciences 26, 573–613.

Krause, J.M., Bellosi, E.S., Raigemborn, M.S., 2010. Lateritized tephric palaeosols from central Patagonia, Argentina: A southern high-latitude archive of Palaeogene global greenhouse conditions. Sedimentology 57, 1721–1749.

Kraus, M.J., 1999. Paleosols in clastic sedimentary rocks: Their geologic applications. Earth-Science Reviews 47, 41–70.

Kraus, M.J., Aslan, A., 1993. Eocene hydromorphic paleosols—Significance for interpreting ancient floodplain processes. Journal of Sedimentary Petrology 63, 453–463.

Kraus, M.J., Riggins, S., 2007. Transient drying during the Paleocene–Eocene thermal maximum (PETM): Analysis of paleosols in the Bighorn Basin, Wyoming. Palaeogeography, Palaeoclimatology, Palaeoecology 245, 444–461.

Kroeger, K.F., Funnell, R.H., 2012. Warm Eocene climate enhanced petroleum generation from Cretaceous source rocks: A potential climatic feedback mechanism? Geophysical Research Letters 39, L04701.
Machlus, M., Hemming, S.R., Olsen, P.E., Christie-Blick, N., 2004. Eocene calibration of geomagnetic polarity time scale reevaluated: Evidence from the Green River Formation of Wyoming. Geology 32, 137–140.
Mack, G.H., James, W.C., Monger, H.C., 1993. Classification of paleosols. Geological Society of America Bulletin 105, 129–136.
Maynard, J.B., 1992. Chemistry of modern soils as a guide to interpreting Precambrian paleosols. The Journal of Geology 100, 279–289.
Miller, L., Smith, S.Y., Sheldon, N.D., Strömberg, C.A.E., 2012. Eocene vegetation dynamics in Montana inferred from a high-resolution phytolith record. Geological Society of America Bulletin 124, 1577–1589.
Nordt, L.C., Driese, S.D., 2010. New weathering index improves paleorainfall estimates from Vertisols. Geology 38, 407–410.
Retallack, G.J., 1991. Untangling the effects of burial alteration and ancient soil formation. Annual Review of Earth and Planetary Sciences 19, 183–206.
Retallack, G.J., 2001. Soils of the Past—An Introduction to Paleopedology: Oxford, UK, Blackwell Science Ltd., 404 p.
Retallack, G.J., 2007. Cenozoic paleoclimate on land in North America. The Journal of Geology 115, 271–294.
Retallack, G.J., 2009. Refining a pedogenic carbonate CO_2 paleobarometer to quantify a middle Miocene greenhouse spike. Palaeogeography, Palaeoclimatology, Palaeoecology 281, 57–65.
Retallack, G.J., Sheldon, N.D., Carr, P.F., Fanning, M., Thompson, C.A., Williams, M.L., Jones, B.G., Hutton, A., 2011. Multiple Early Triassic greenhouse crises impeded recovery from Late Permian mass extinction. Palaeogeography, Palaeoclimatology, Palaeoecology 308, 233–251.
Romanek, C.S., Grossman, E.L., Morse, J.W., 1992. Carbon isotopic fractionation in synthetic aragonite and calcite: Effects of temperature and precipitation rate. Geochimica et Cosmochimica Acta 56, 419–430.
Scotese, C.R., 2000. Earth System History Geographic Information System, ArcView 3.2, v. 2.0C.
Sewall, J.O., Sloan, L.C., 2006. Come a little bit closer: A high-resolution climate study of the early Paleogene Laramide foreland. Geology 34, 81–84.
Sexton, P.F., Norris, R.D., Wilson, P.A., Palike, H., Westerhold, T., Röhl, U., Bolton, C.T., Gibbs, S., 2011. Eocene global warming events driven by ventilation of oceanic dissolved organic carbon. Nature 471, 349–352.
Sheldon, N.D., 2009. Non-marine records of climate change across the Eocene-Oligocene transition, *in* Koeberl, C., and Montanari, A., eds., The Late Eocene Earth—Hothouse, Icehouse, and Impacts. Geological Society of America Special Publication 452, 241–248.
Sheldon, N.D., Tabor, N.J., 2009. Quantitative paleoenvironmental and paleoclimatic reconstruction using paleosols. Earth-Science Reviews 95, 1–52.
Sheldon, N.D., Retallack, G.J., Tanaka, S., 2002. Geochemical climofunctions from North American soils and applications to paleosols across the Eocene-Oligocene boundary in Oregon. The Journal of Geology 110, 687–696.

Sheldon, N.D., Costa, E., Cabrera, L., Garces, M., 2012. Continental climatic and weathering response to the Eocene-Oligocene transition. The Journal of Geology 120, 227–236.
Smith, M.E., Singer, B., Carroll, A., 2003. $^{40}Ar/^{39}Ar$ geochronology of the Eocene Green River Formation, Wyoming. Geological Society of America Bulletin 115, 549–565.
Smith, M.E., Carroll, A.R., Singer, B.S., 2008. Synoptic reconstruction of a major ancient lake system: Eocene Green River, western United States. Geological Society of America Bulletin 120, 54–84.
Smith, R.Y., Greenwood, D.R., Basinger, J.F., 2010. Estimating paleoatmospheric pCO_2 during the early Eocene climatic optimum from stomatal frequency of *Ginkgo*, Okanagan Highlands, British Columbia, Canada. Palaeogeography, Palaeoclimatology, Palaeoecology 293, 120–131.
Strömberg, C.A.E., 2002. The origin and spread of grass-dominated ecosystems in the Late Tertiary of North America: Preliminary results concerning the evolution of hypsodonty. Palaeogeography, Palaeoclimatology, Palaeoecology 177, 59–75.
Strömberg, C.A.E., 2003. The Origin and Spread of Grass-Dominated Ecosystems during the Tertiary of North America and How it Relates to the Evolution of Hypsodonty in Equids [Ph.D. thesis]: Berkeley, California, Department of Biology, University of California–Berkeley, 779 p.
Strömberg, C.A.E., 2005. Decoupled taxonomic radiation and ecological expansion of open-habitat grasses in the Cenozoic of North America. Proceedings of the National Academy of Sciences of the United States of America 102, 11980–11984.
Strömberg, C.A.E., Werdelin, L., Friis, E.M., Sarac, G., 2007. The spread of grass-dominated habitats in Turkey and surrounding areas during the Cenozoic: Phytolith evidence. Palaeogeography, Palaeoclimatology, Palaeoecology 250, 18–49.
Stucky, R.K., 1984. Revision of the Wind River faunas, early Eocene of central Wyoming: Part 5. Geology and biostratigraphy of the upper part of the Wind River Formation, northeastern Wind River Basin. Annals of the Carnegie Museum 53, 231–325.
Takeuchi, A., Larson, P.B., Suzuki, K., 2007. Influence of paleorelief on the mid-Miocene climate variation in southeastern Washington, northeastern Oregon, and western Idaho, USA. Palaeogeography, Palaeoclimatology, Palaeoecology 254, 462–476.
Thrasher, B.L., Sloan, L.C., 2009. Carbon dioxide and the early Eocene climate of western North America. Geology 37, 807–810.
Thrasher, B.L., Sloan, L.C., 2010. Land cover influences on regional climate of western North America during the early Eocene. Global and Planetary Change 72, 25–31.
Tipple, B.J., Meyers, S.R., Pagani, M., 2010. Carbon isotope ratio of Cenozoic CO_2: A comparative evaluation of available geochemical proxies. Paleoceanography 25, PA3202.
U.S. Department of Agriculture Soil Survey Staff, 1999. Keys to Soil Taxonomy (8th ed.): Blacksburg, Virginia, Pocahontas Press, 600 p.
Weissmann, G.S., Hartley, A.J., Nichols, G.J., Scuderi, L.A., Olson, M., Buehler, H., Banteah, R., 2010. Fluvial form in modern continental sedimentary basins: Distributive fluvial systems. Geology 38, 39–42.
Whiteside, J.H., Olsen, P.E., Eglinton, T.I., Cornet, B., McDonald, N.G., Huber, P., 2011. Pangean Great Lake paleoecology on the cusp of the end-Triassic extinction. Palaeogeography, Palaeoclimatology, Palaeoecology 301, 1–17.

Wilf, P., Cuneo, N.R., Johnson, K.R., Hicks, J.F., Wing, S.L., Obradovich, J.D., 2003. High plant diversity in Eocene South America: Evidence from Patagonia. Science 300, 122–125.

Wing, S.L., Harrington, G.J., 2001. Floral response to rapid warming in the earliest Eocene and implications for concurrent faunal change. Paleobiology 27, 539–563.

Wing, S.L., Bown, T.M., Obradovich, J.D., 1991. Early Eocene biotic and climatic change in interior western North America. Geology 19, 1189–1192.

Winterfeld, G.F., Conard, J.B., 1983. Laramide tectonics and deposition, Washakie Range and northwestern Wind River Basin, Wyoming, *in* Lowell, J.D., ed., Rocky Mountain Foreland Basins and Uplifts: Denver, Colorado, Rocky Mountain Association of Geologists, 137–148.

Woodburne, M.O., Gunnell, G.F., Stucky, R.K., 2009. Climate directly influences Eocene mammal faunal dynamics in North America. Proceedings of the National Academy of Sciences of the United States of America 106, 13399–13403.

Zachos, J., Pagani, M., Sloan, L., Thomas, E., Billups, K., 2001. Trends, rhythms, and aberrations in global climate 65 Ma to present. Science 292, 686–693.

Zachos, J.C., Wara, M.W., Bohaty, S., Delaney, M.L., Petrizzo, M.R., Brill, A., Bralower, T.J., Premoli-Silva, I., 2003. A transient rise in tropical sea surface temperature during the Paleocene-Eocene thermal maximum. Science 302, 1551–1554.

Zachos, J., Dickens, G.R., Zeebe, R.E., 2008. An early Cenozoic perspective on greenhouse warming and carbon-cycle dynamics. Nature 451, 279–283.

Zonneveld, J.P., Gunnell, G.F., Bartels, W.S., 2000. Early Eocene fossil vertebrates from the southwestern Green River Basin, Lincoln and Uinta Counties, Wyoming. Journal of Vertebrate Paleontology 20, 369–386.

Zucol, A.F., Brea, M., Bellosi, E.S., 2010. Phytolith studies in Gran Barranca (central Patagonia, Argentina): The middle-late Eocene, *in* Madden, R.H., Carlini, A.A., Vucetich, M.G., and Kay, R.F., eds., Paleontology of Gran Barranca: Evolution and Environmental Change through the Middle Cenozoic of Patagonia: Cambridge, UK, Cambridge University Press, 317–340.

CHAPTER V

Constraining the Early Eocene Climatic Optimum: An inter-hemispheric comparison

Official citation:

Hyland, E.G., Cotton, J.M., Sheldon, N.D., Fiorella, R.P., *in preparation*. Constraining the Early Eocene Climatic Optimum: An inter-hemispheric comparison.

ABSTRACT

The Early Eocene Climatic Optimum (EECO) was a period of major climatic and environmental change (53–50 Mya) that was caused by perturbations to the global carbon cycle. Recent work from terrestrial sections in the Northern Hemisphere demonstrate that the event is characterized by different responses in the terrestrial and marine realms, which suggests that traditional causal mechanisms may not adequately explain the dynamics of the EECO. Here we present a new high-resolution multiproxy record of terrestrial conditions during the EECO from the Southern Hemisphere (Maíz Gordo Formation, northwestern Argentina) and compare this record to those from the Northern Hemisphere. Similar to the Northern Hemisphere records, the new record shows a transient peak period of carbon isotopic enrichment, as well as increased temperatures and precipitation which indicate that terrestrial environmental responses to EECO changes were broadly consistent in temperate settings worldwide. This global consistency can be used to constrain potential causal mechanisms for the EECO through a series of global carbon model scenarios using the LOSCAR platform that represent traditional concepts of early Eocene carbon cycle perturbations (e.g., volcanism, methane hydrate releases). These model simulations

indicate that no single causal mechanism sufficiently explains marine and terrestrial proxy observations, and that a preferred carbon modeling scenario involving both increased ventilation of oceanic carbon and increased carbonate weathering can meet basic target criteria for the EECO.

5.1 INTRODUCTION

The Early Eocene Climatic Optimum (EECO) occurred between 53 and 50 Mya, with substantial shifts in greenhouse gas concentrations, global temperatures, precipitation patterns, as well as floral and faunal biogeographies, and may be the best available analogue for future climatic conditions in a high CO_2 world (>500 ppm) based on climate sensitivity models (e.g., IPCC, 2007; Rohling et al., 2012). The climate impacts and ecological responses of the EECO are well described and robustly modeled (e.g., Zachos et al., 2001; Smith et al., 2008; Thrasher and Sloan, 2009; Huber and Caballero, 2011), but the primary cause of the high carbon dioxide concentrations that led to the EECO remains highly contentious. This fundamentally affects how the event dynamics are understood and the potential predictive value for future climate change.

While proxy and model-based estimates of the magnitude of change in global temperatures (~6°C; e.g., Greenwood and Wing, 1995; Zachos et al., 2001), regional precipitation (~600 mm yr^{-1}; e.g., Shellito et al., 2003; Hyland et al., 2013), and atmospheric CO_2 concentrations (~1000 ppm; e.g., Royer et al., 2001; Demicco et al., 2003; Hyland and Sheldon, 2013) are well constrained for the EECO, pinpointing the release timescale and source of greenhouse gases responsible for the event has been difficult due to the complicated nature of the carbon cycle and terrestrial-atmospheric-oceanic interactions. Until recently, nearly all of the available early Eocene and specifically EECO climate proxy data came from ocean sediments worldwide (e.g., Shellito et al., 2003; Sluijs et al., 2008; Hollis et al., 2012), but new terrestrial proxy data from both western North America and now central South America (Figure 5.1) have shed light on discrepancies between the purported causes of the EECO and the changes recorded in terrestrial and marine materials (e.g., Krause et al., 2010; Hyland and Sheldon, 2013; Hyland et al., 2013; this work).

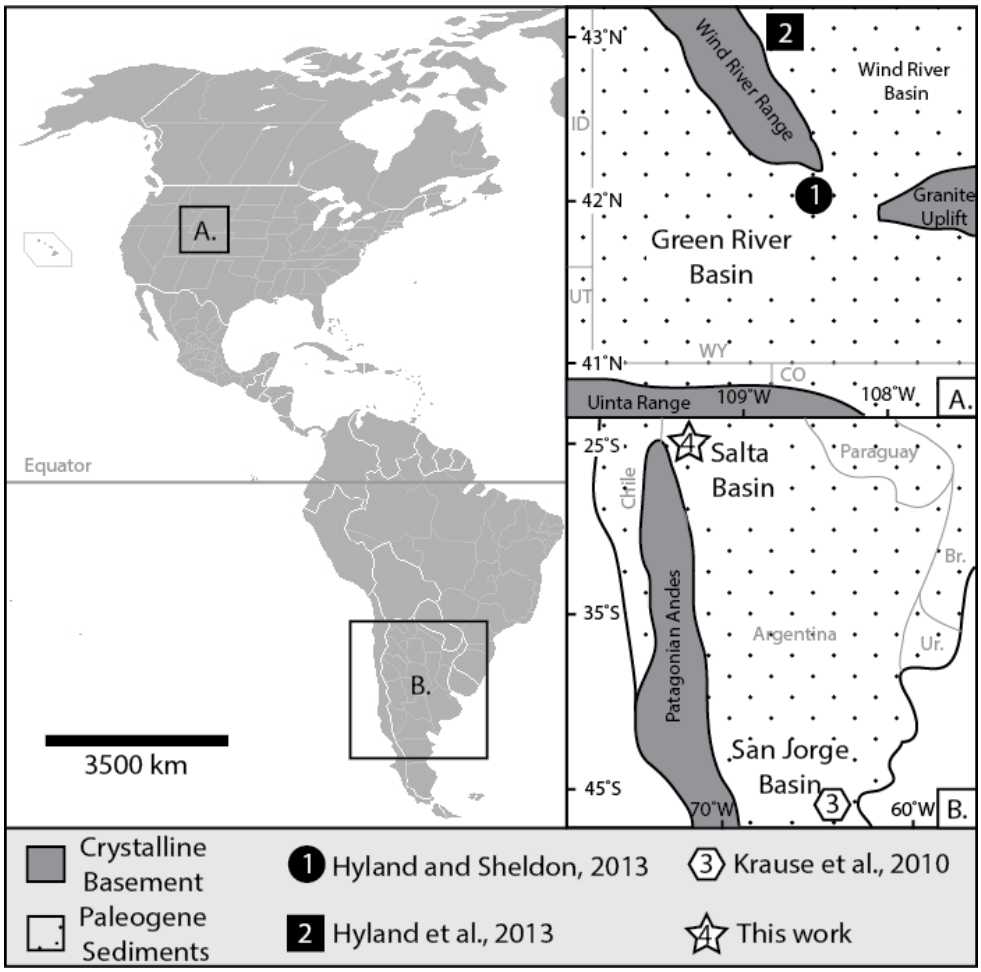

Figure 5.1 Site locations for terrestrial EECO reconstructions in the Northern (A) and Southern (B) Hemispheres.

The comparison of marine and terrestrial records is crucial for detailing the dynamics of the global climate system and for understanding the changes in the carbon cycle that led to the EECO. Here we compile high-resolution proxy records from North America and present a new record from South America (Salta Basin) as the first inter-hemispheric comparison of the terrestrial impacts of the EECO on regional/global climates and the global carbon cycle. While there is some timescale uncertainty inherent in such a broad scale comparison across terrestrial localities, each of the chosen sites is fairly well constrained (±0.3 Ma) and has been further tuned based on the initiation of the EECO carbon isotope excursion. We present these records in the

context of established marine proxy trends during the early Eocene, and illustrate the effects of simulated carbon cycle changes on major carbon reservoirs via mass-balance accounting and carbon cycle modeling (e.g., Kump and Arthur, 1999; Zeebe et al., 2009; McInerney and Wing, 2011; Sluijs et al., 2013) in order to examine potential drivers of greenhouse-gas-related global change during the EECO.

5.2 PREVIOUS RESULTS

5.2.1 Northern Hemisphere records

Paleogene terrestrial records from the Northern Hemisphere are known primarily from temperate North America (western United States and Canada), and the most detailed records of the EECO are found in the intermontane basins of Wyoming (Figure 5.1; e.g., Greenwood and Wing, 1995; Smith et al., 2008; Fan et al., 2011; Hyland and Sheldon, 2013; Hyland et al., 2013). The record of the EECO event in these Northern Hemisphere sites is defined by a positive carbon isotope excursion (CIE) of ~3–5‰ in organic carbon (Figure 5.2A) and ~2–3‰ in pedogenic carbonates, which corresponds to an ~1000 ppm increase in atmospheric pCO_2 relative to pre-event concentrations (Hyland and Sheldon, 2013; Hyland et al., 2013). This greenhouse gas increase is coupled with a temperature rise of ~5–7°C (Figure 5.2C; Greenwood and Wing, 1995; Hyland and Sheldon, 2013; Hyland et al., 2013), which is inferred from paleobotanical, paleosol geochemical, and pedogenic carbonate stable isotope ($\delta^{18}O$) methods. As a result of rising temperatures and changes in atmospheric circulation patterns, regional precipitation also increased by ~600 mm yr^{-1} (Figure 5.2D; Smith et al., 2008; Hyland and Sheldon, 2013; Hyland et al., 2013; Chapters 3 – 5), which is inferred from sedimentological changes, paleosol physical properties (depth to Bk), and paleosol geochemistry.

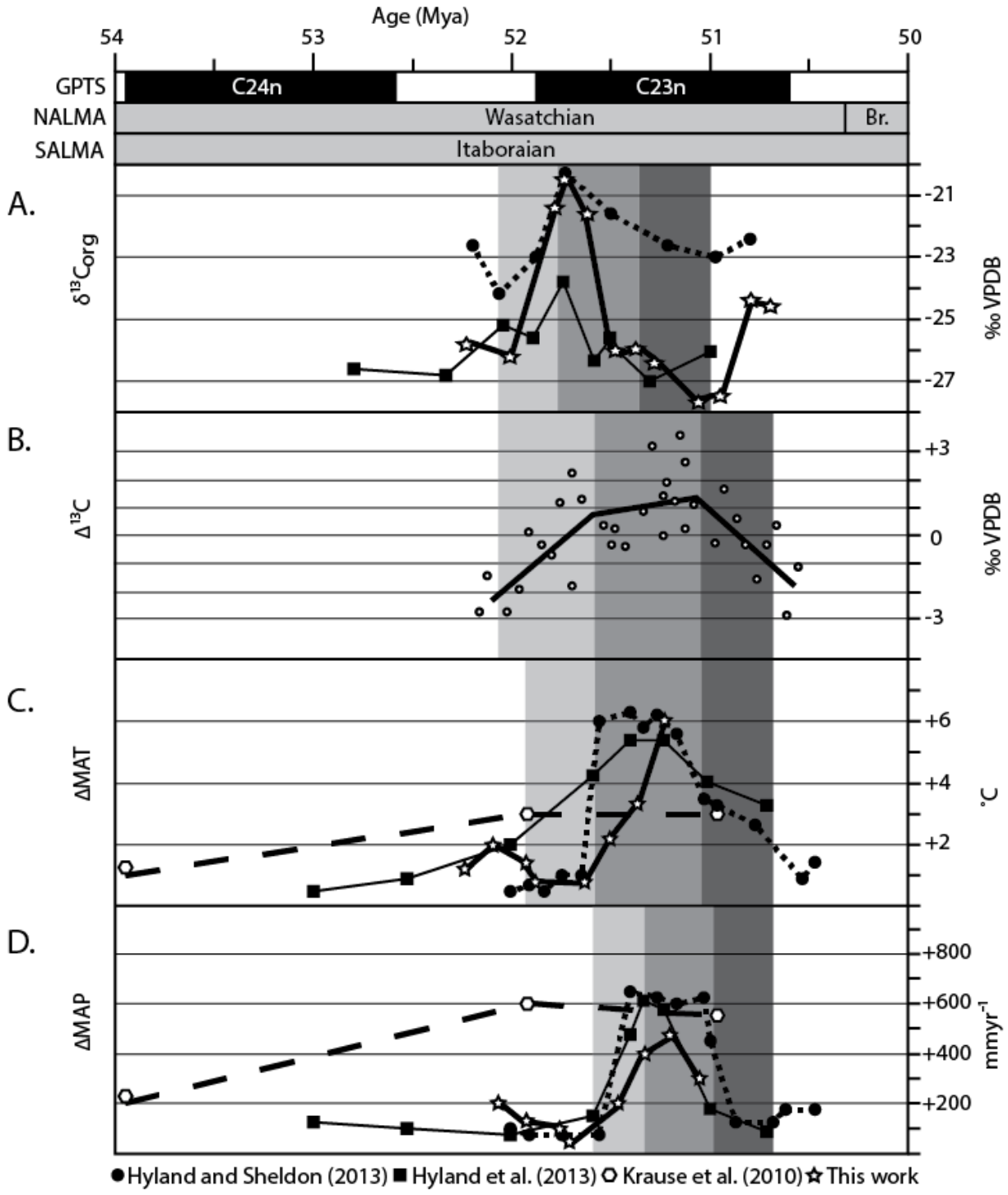

Figure 5.2 Comparison of A) carbon isotope ($\delta^{13}C_{org}$), B) carbon isotope anomaly ($\Delta^{13}C$) from the Green River Basin (Hyland and Sheldon, 2013) with generalized trend, C) temperature (ΔMAT), and D) precipitation (ΔMAP) proxy records of the EECO from temperate latitudes in both hemispheres. Closed symbols represent sites in North America (Hyland and Sheldon, 2013; Hyland et al., 2013), and open symbols represent sites in South America (Krause et al., 2010; this work). Shaded windows indicate the initiation, peak, and recovery phases of the EECO event. Points displayed in panel A are 3-pt running averages of original source data.

Despite problems with explaining global temperature gradients in equable Eocene climates, both regional climate models for North America (e.g., Thrasher and Sloan, 2009; Thrasher and Sloan, 2010) and global climate models (e.g., Shellito et al., 2003; Huber et al., 2011) suggest that these recorded changes are consistent with a rapid increase to 2–3× pre-EECO atmospheric CO_2 concentrations.

5.2.2 Southern Hemisphere records

Terrestrial records from the Paleogene of the Southern Hemisphere are limited, though some low-resolution examples exist from basins in South America (Argentina; Figure 5.1) that can potentially be expanded as local stratigraphy improves (e.g., Krause et al., 2010). While no carbon isotope records are available for this time period, both paleosol-based and paleobotanical estimates of paleoclimatic conditions identify the EECO in the Southern Hemisphere. Krause et al. (2010) previously described Patagonian lateritic paleosols that span the EECO and reconstructed peak MAT ~3°C higher than the Eocene baseline, and peak MAP ~600 mm yr^{-1} higher than the Eocene baseline (Figure 5.2). Similarly, Wilf et al. (2003) suggested peak warming of ~6°C (MAT) and peak increases in precipitation near ~200 mm yr^{-1} based on a series of paleobotanical records from the same region. However, with a lack of carbon isotope records and limited preservation of paleosols or plant material during the EECO itself, the structure and duration of the event remain poorly constrained for the Southern Hemisphere. Despite these limitations and minimal regional or high-resolution climate modeling for South America during the early Eocene (e.g., Jaramillo and Cardenas, 2013), global climate models suggest that these Argentine records are also consistent with rapidly increased atmospheric greenhouse gas concentrations (e.g., Shellito et al., 2003; Huber et al., 2011).

5.3 METHODS

To expand and improve high-resolution records of the EECO in the Southern Hemisphere, we constructed a multiproxy record throughout the early Eocene for a site in the Salta Basin of northwestern Argentina (Cerro Bayo; Figure 5.1). The Cerro Bayo section contains a series of fluvio-lacustrine formations deposited in the Salta Basin (paleo-Lake Alémania) during the early Paleogene (Marquillas et al., 2005). While the Salta Basin now resides at moderate elevations in the subtropics (near 25°S), this section was originally deposited at lower elevations (Salfity and Monaldi, 2006) in temperate latitudes around 40°S (±5°; Scotese, 2000), making the Cerro Bayo section an excellent comparison point in the Southern Hemisphere for many of the available Northern Hemisphere records of the EECO (e.g., Hyland et al., 2013).

We constrained the age of this record by performing magnetostratigraphic sampling of the upper Cerro Bayo section in the Salta Basin (Figure 5.1; Maíz Gordo Formation) to determine normal and reversed polarity intervals and to tie the local polarity pattern to the geomagnetic polarity timescale (GPTS; Gradstein et al., 2012). Paleomagnetic sampling of cores drilled from oriented hand samples was conducted at the University of Michigan Paleomagnetism Laboratory. Stepwise thermal demagnetization used an ASC thermal demagnetizer and a 2G cryogenic magnetometer, and analysis of 62 sampling levels (~1.8 m interval) yielded reliable characteristic remanent magnetization (ChRM) directions at 58 levels (Appendix D1). ChRM directions from vector endpoint diagrams were calculated on a minimum of 5 measurements (250–600°C) using Virtual Paleomagnetic Directions (VPD) software (Ramón and Pueyo, 2008). Sample means were calculated for ~3 individual cores for each sample level, and samples with a mean angular deviation (MAD) >15° were rejected from further analysis; resultant MAD values for final samples averaged 7.4°. Polarity zones are

defined by multiple stable sample levels and a lack of ambiguous samples in those zones, suggesting the primary origin of the established intervals.

In order to construct high-resolution multiproxy records of this site, we collected paleosol samples (trenched to at least 20 cm below the modern surface to avoid contamination) within the measured local stratigraphy and analyzed both the major elemental composition of paleosol bulk samples and the carbon isotope composition of paleosol A-horizon samples. Major element data from paleosol geochemical analyses (XRF analyses performed at ALS Chemex Laboratory, where major element replicate standard deviations are < 0.5%) of identified B-horizons were input into weathering climofunctions for mean annual temperature (MAT; Gallagher and Sheldon, 2013) and mean annual precipitation (MAP; Sheldon et al., 2002). Carbon stable isotope data from organic root and dispersed carbon material were sampled from paleosol A-horizons and cleaned of modern organics with methanol, acidified with 7% HCl, rinsed, and homogenized before being analyzed at the University of Michigan Stable Isotope Laboratory on a Costech elemental analyzer attached to a Finnigan Delta V+ isotope ratio mass spectrometer, where analytical uncertainty is < 0.1‰.

In order to compare conditions observed in proxy records and examine carbon reservoirs and release sources, a long-term ocean-atmosphere-sediment carbon cycle reservoir model (LOSCAR; Zeebe et al., 2009; Zeebe, 2012 and references therein) was used. Model initialization conditions for LOSCAR simulations followed the global boundary conditions of Zeebe et al.'s (2009) late Paleocene simulation ("prePETM"), with modifications to starting climatic parameters fitting the early Eocene ("preEECO"; summarized in Appendix D4). To simulate the observed profile of the EECO isotopic excursions and atmospheric pCO_2 estimates both in terms of their magnitude and specific conditions, a series of potential causal scenarios

(summarized in Appendix D5) that have been suggested for the early Eocene were tested including: 1) increased volcanic emissions (e.g., Zachos et al., 2008), 2) large-scale methane releases (e.g., Dickens, 2003), 3) increased carbonate weathering and metamorphism (e.g., Kerrick and Caldeira, 1999; Kent and Muttoni, 2008), and 4) changes in ocean circulation/increased ventilation (e.g., Sexton et al., 2011; Hyland et al., 2013). Successful simulation of the EECO with LOSCAR is recognized through four target criteria (Scenario 0, Table 5.1), which include roughly a doubling of atmospheric pCO_2, increasing $\delta^{13}C$ of atmospheric CO_2, decreasing $\delta^{13}C$ of dissolved inorganic carbon (DIC), and a shoaling of the carbonate compensation depth (CCD). Each of these conditions is based on substantial proxy data from both terrestrial (atmospheric conditions; e.g., Hyland and Sheldon, 2013; this work) and marine (oceanic conditions; e.g., Zachos et al., 2001; Muttoni and Kent, 2007; Norris et al., 2013) records, and collectively represent minimum requirements for any viable carbon model scenario for the EECO (c.f., Sluijs et al., 2013).

5.4 RESULTS

5.4.1 Salta Basin results

The EECO is represented in the Salta Basin at Cerro Bayo by fluvial sediments and paleosols within the Maíz Gordo Formation, which spans roughly 53.2–50.5 Mya based on magnetostratigraphic and biostratigraphic relationships (Figure 5.3; Quattrocchio and Volkheimer, 2000; Gelfo et al., 2009; Gradstein et al., 2012; Woodburne et al., 2014). Based on magnetostratigraphic boundaries (Gradstein et al., 2012), sedimentation rates were constant (~50 m Ma^{-1}) within the Maíz Gordo Formation with slight variations between upper and lower due to changes in lithology and depositional mode (c.f., Marquillas et al., 2005), which agrees with

estimates from depositional constraints provided by uplift models (DeCelles et al., 2011). This new age model assessment of the Maíz Gordo Formation thereby allows for a high-resolution reconstruction of climate conditions in the Southern Hemisphere that is comparable to other terrestrial sites during the EECO interval.

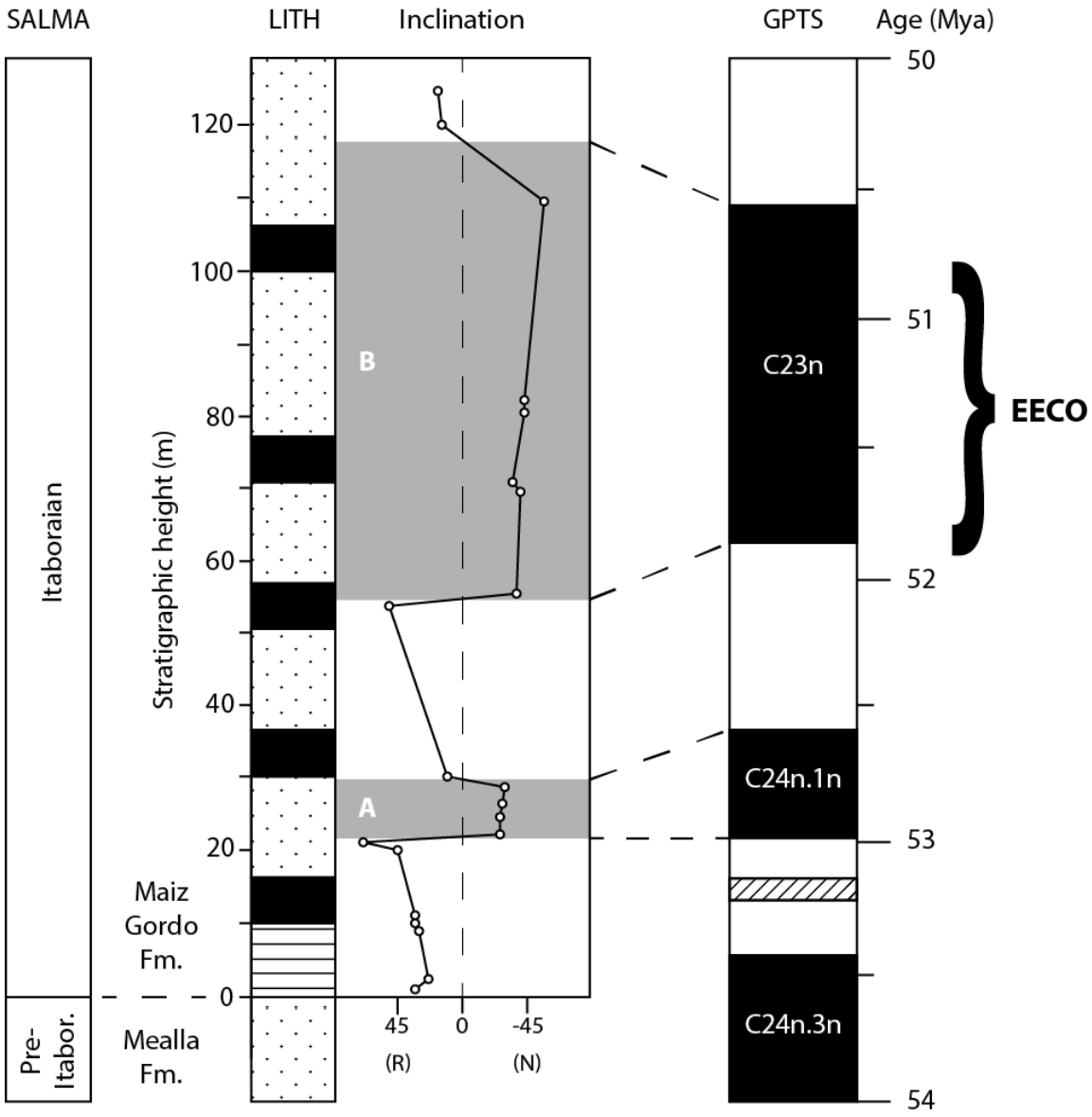

Figure 5.3 Age interpolation model based on magnetostratigraphic boundaries and sedimentological and paleontological constraints. Paleontological age constraints are based on mammalian and palynofloral records known from the base and upper Maíz Gordo Formation (Quattrocchio and Volkheimer, 2000; Gelfo et al., 2009) and the revised SALMA timescale of Woodburne et al. (2014).

Using paleosol-based terrestrial climate proxies such as weathering indices of paleosol profiles (CIA-K of Sheldon et al., 2002; PWI of Gallagher and Sheldon, 2013) and organic carbon isotopic compositions in paleosol A-horizons (e.g., Cotton and Sheldon, 2012), the first multiproxy record of terrestrial change during the EECO in the temperate Southern Hemisphere (Figure 5.2) has been compiled. The EECO is characterized in the Salta Basin by a positive CIE of ~5.5‰ in organic carbon (Figure 5.2A), from roughly -26.4‰ to -20.7‰, that occurred between 52.0 and 51.5 Mya. This carbon isotope change is coupled with a temperature rise of ~6°C, from roughly 9.8°C to 15.9°C, inferred from MAT climofunctions, as well as a consequent precipitation increase of ~500 mm yr^{-1}, from roughly 710 mm yr^{-1} to 1220 mm yr^{-1}, which is indicated by MAP climofunctions (Figure 5.2). In each case, these proxy records indicate transient peak conditions occurring on timescales of < 0.5 Ma, with rapid initiation periods followed by a longer peak and recovery (to Eocene baselines) period.

5.4.2 Model results

EECO carbon cycle dynamics were explored first by considering the impact of single-mechanism scenarios (Table 5.1), and then by examining scenarios in which multiple-mechanism changes were modeled. Each scenario was compared to the EECO target criteria established from proxy records and summarized in Scenario 0 of Table 5.1, where a successful simulation scenario required matching responses in all categories (see *Methods*).

Results for the increased volcanism scenarios (Scenario 1 family) were able to attain high atmospheric pCO_2 values for the EECO (Scenarios 1.2 and 1.3; Table 5.1), but predicted limited or slightly positive carbon isotope excursions in both the atmosphere and deep ocean and resulted in a distinct deepening of the CCD in all basins (Table 5.1; Appendix D6). These isotopic and CCD changes were inconsistent with the EECO target scenario, and the magnitude

of the carbon release required to attain high atmospheric pCO_2 concentrations over these time periods via increased volcanic degassing is unreasonably large based on modern and paleo-calculations of volcanic production rates even under conditions of extremely active spreading centers or large igneous provinces (e.g., Self et al., 2005; Bryan and Ferrari, 2013).

Results for the methane release scenarios (Scenario 2 family) were unable to attain sufficiently high atmospheric pCO_2 values for the EECO and also predicted substantial negative carbon isotope excursions in both the atmosphere and deep ocean, though these simulations did succeed in predicting a shoaling of the CCD in all major ocean basins (Table 5.1; Appendix D6). These carbon concentration and isotope changes were inconsistent with the EECO target scenario, and due to the long timescale of methane regeneration/storage post-Paleocene Eocene Thermal Maximum (e.g., Zeebe et al., 2009; McInerney and Wing, 2011), additional large methane releases or methane sources with substantially different $\delta^{13}C$ compositions (-55 ±10‰; e.g., Zeebe et al., 2009) are unlikely.

Results for the carbonate weathering scenarios (Scenario 3 family) were unable to attain sufficiently high atmospheric pCO_2 values for the EECO, predicted positive carbon isotope excursions in both the atmosphere and deep ocean, and also predicted a deepening of the CCD in all major ocean basins (Table 5.1; Appendix D6). All of these results are inconsistent with the EECO target scenario, and any larger changes in carbonate weathering (e.g., more substantial uplift or metamorphism of carbonate sediments in the Tethyan basin) are likely unrealistic for the early Eocene based on paleogeographic reconstructions (Kerrick and Caldeira, 1999).

Results for the increased ocean ventilation scenarios (Scenario 4 family) were unable to attain sufficiently high atmospheric pCO_2 values for the EECO, but these simulations did successfully reconstruct both a positive atmospheric CIE and a negative oceanic ($\delta^{13}C_{DIC}$ of deep

water) CIE, as well as a shoaling of the CCD in all major basins (Table 5.1). These changes are largely consistent with the EECO target scenario, except for the limited rise in atmospheric carbon dioxide. Thus, while individual mechanisms for the EECO are variably successful in predicting empirically observed results, no single mechanism for carbon cycle change during the EECO is sufficient to explain proxy observations. This instead suggests that a combination of mechanisms including increased ventilation and another carbon cycle perturbation may be required to attain the EECO conditions characterized in proxy records.

Table 5.1 LOSCAR scenario conditions and results for the EECO compared to proxy observations of atmospheric carbon dioxide concentrations (pCO_2), carbon isotope composition of the atmosphere ($\delta^{13}C_a$), carbon isotope composition of the deep ocean ($\delta^{13}C_{DIC}$), and the depth of the carbonate compensation depth (CCD).

Scenario	pCO_2	$\delta^{13}C_a$	$\delta^{13}C_{DIC}$	CCD	Evaluation
0. EECO target (FIG 5.2)	**~200%**	↑	↓	**Shoals**	-----
1.1 Volcanism (+10%) 1.2 Volcanism (+25%) 1.3 Volcanism (+50%)*	>200%	↑	↑	Deepens	FAIL
2.1 Methane (1000 Pg) 2.2 Methane (3000 Pg) 2.3 Methane (6000 Pg)†	<180%	↓	↓	Shoals	FAIL
3.1 Carbonates (-33%) 3.2 Carbonates (-66%)	<125%	↑	↑	Deepens	FAIL
4.1 Ventilation (+10%) 4.2 Ventilation (+25%) 4.3 Ventilation (+50%)	<140%	↑	↓	Shoals	FAIL
5. Combined (4.3 and 3.2)	190%	↑	↓	Shoals	SUCCESS

* Inconsistent with volcanic area observations (Self et al., 2005; Bryan and Ferrari, 2013)
† Inconsistent with methane generation and burial rates (McInerney and Wing, 2011)

Results for the combined-mechanism scenario of increased ventilation and carbonate weathering (Scenario 5 family) produce atmospheric pCO_2 values similar to the EECO target

scenario (~190%), as well as a short term positive atmospheric CIE (+0.5‰), a long term negative oceanic CIE (-0.7‰; $\delta^{13}C_{DIC}$ of deep water), and a substantial shoaling of the CCD in all major basins (~1000 m), all of which are consistent with the EECO target scenario (Table 5.1; Figure 5.4). Combined-mechanism scenarios for other pairs of causal mechanisms (e.g., ventilation and volcanism) do not produce the same successful EECO target criteria responses as Scenario 5 due to conflicting carbon cycle responses (opposing CIEs), and are therefore not discussed further in the context of this work.

5.5 DISCUSSION

5.5.1 Inter-hemispheric dynamics

Terrestrial climate records from temperate regions in the Northern and Southern Hemispheres are in broad agreement in terms of the magnitude of climatic and ecological (e.g., Wilf et al., 2003; Hyland et al., 2013) change that occurred during the Early Eocene Climatic Optimum (Figure 5.2). While terrestrial records are consistent between hemispheres, the magnitude of change and the timescale of the event recorded in these continental basins differ from those recorded in marine sediments in both hemispheres. In the context of these global marine records (e.g., Zachos et al., 2001; Sluijs et al., 2008; Hollis et al., 2012), terrestrial proxy records in both hemispheres show slightly enhanced temperature and isotopic shifts; however, this enhancement is consistent with linked terrestrial-marine records of other climatic events like the Paleocene-Eocene Thermal Maximum (e.g., McInerney and Wing, 2011) or the Eocene-Oligocene transition (e.g., Sheldon et al., 2012), which also record larger magnitude changes in terrestrial settings than in marine settings due to the effects of continentality and relative carbon reservoir size.

Given those expected differences in apparent event magnitude, proxy records from other climatic events and from global climate models (e.g., Huber et al., 2011; Rohling et al., 2012) suggest that the observed magnitudes of EECO climatic responses in the terrestrial and marine records are in agreement and that they result from increased atmospheric greenhouse gas concentrations, but that the two types of records diverge both in terms of the direction/magnitude of change of their respective carbon isotope excursions and in terms of the timescale over which the resultant climatic shifts are manifest. Terrestrial records of the EECO show an average CIE of +4‰ (Figure 5.2), whereas marine records show the opposite trend in carbon, with an average CIE of -0.7‰ (e.g., Zachos et al., 2008). Paired carbon isotope data from organic ($\delta^{13}C_{org}$) and inorganic ($\delta^{13}C_{cc}$) sources at each terrestrial locality also record a positive $\Delta^{13}C$ anomaly ($\delta^{13}C_{org}$ - $\delta^{13}C_{cc}$) during the EECO event of roughly 3.5‰ (Figure 5.2). In addition to this carbon record discrepancy, the timescales of change are significantly different between the terrestrial record (Figure 5.2), where the peak event is characterized by a rapid initiation phase (~0.2 Ma) followed by a plateau of peak climatic conditions (~0.5 Ma) and a rapid recovery phase (~0.2 Ma), and the marine record, where the event is characterized by a gradual shift and recovery over a period of ~2–3 Ma (e.g., Zachos et al., 2001).

These dynamics indicate that the carbon cycle perturbation that led to the peak EECO and the following recovery processes operated on an intermediate timescale and affected major carbon pools differently (e.g., Schrag et al., 2013), which may require a fundamental reinterpretation of suggested causal mechanisms for the event itself (e.g., increased volcanism; Zachos et al., 2008). Therefore, it is possible use all of these carbon cycle response conditions to differentiate between potentially new causal mechanisms in modeling the imbalance between carbon fluxes and burial that resulted in the events of the EECO.

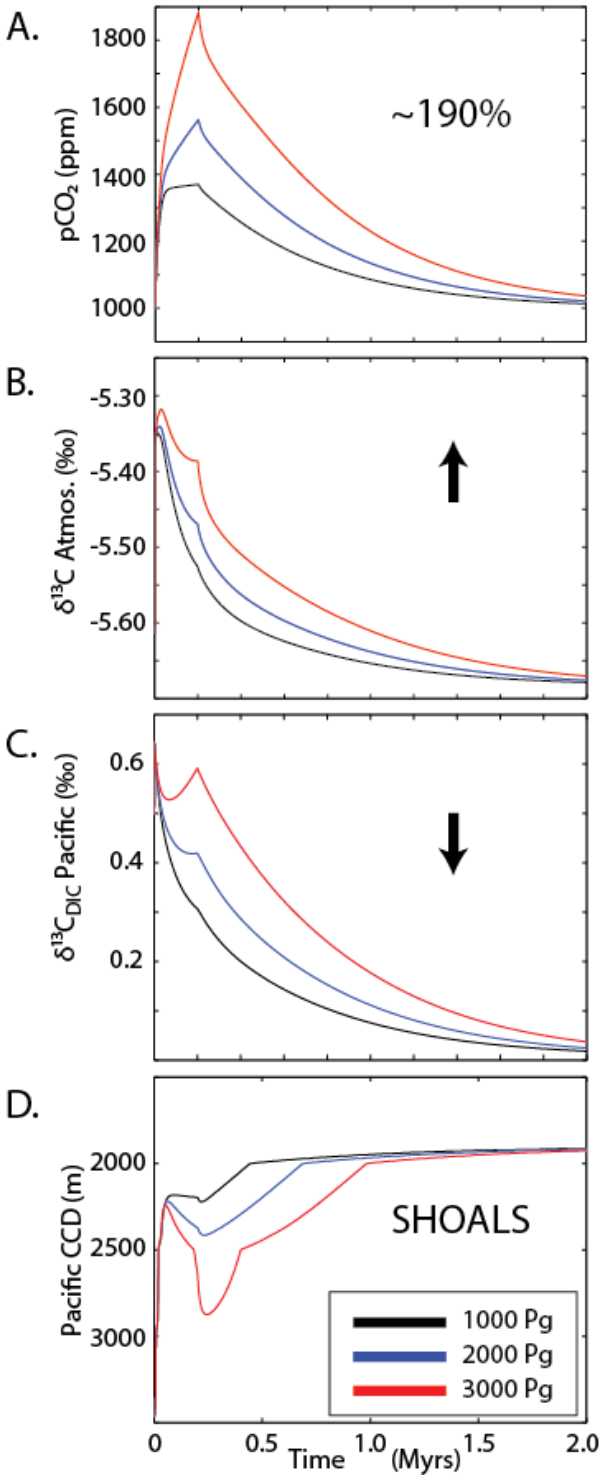

Figure 5.4 LOSCAR model results for preferred EECO carbon scenario (Scenario 5), including predicted changes in A) atmospheric pCO_2, B) carbon isotopic composition of the atmosphere ($\delta^{13}C$ Atmos.), C) carbon isotopic composition of dissolved inorganic carbon in the Pacific Ocean ($\delta^{13}C_{DIC}$ Pacific), and D) carbonate compensation depth of the Pacific Ocean (Pacific CCD). Pacific Ocean values are shown here due to the greater availability of proxy data for comparison (e.g., Zachos et al., 2008), however results for other ocean basins display the same direction and similar magnitudes of change.

5.5.2 EECO causal mechanisms

We suggest a preferred carbon cycle model (Scenario 5) for the EECO involving both increased oceanic ventilation and a discrete carbon input from a source such as heightened carbonate weathering (Figure 5.4), which closely matches proxy observations both in terms of the target conditions (Table 5.1) and their magnitude of change (Figure 5.2), and also remains within the realm of reasonable boundary conditions for the early Eocene carbon cycle. Not only does this scenario match proxy observations in terms of the EECO target criteria, but it also predicts the observed differences in the timescales of change between the terrestrial (~0.5–1 Ma) and the marine (~2–3 Ma) proxy records, as shown by the CIE model results (Figure 5.4B and Figure 5.4C, respectively).

In this scenario, initial EECO conditions are caused by increased oceanic ventilation of dissolved inorganic carbon due to heightened surface mixing and shorter residence times caused by the combination of a more rapid/vigorous hydrologic cycle during global greenhouse conditions (e.g., Bowen et al., 2004; Held and Soden, 2006), the restriction and circulatory closure of the Tethyan and Arctic Ocean basins (e.g., Brinkhuis et al., 2006; Kent and Muttoni, 2008), and regional-scale changes in ocean chemistry (e.g., Zeebe, 2012b). Rapid hydrologic cycling during greenhouse periods can cause changes in ocean surface evaporation rates as well as changes in terrestrial inputs into the oceans (Held and Soden, 2006), which can result in changes in regional and global ocean chemistry, particularly in restricted or closed ocean basins (Zeebe, 2012b; Norris et al., 2013). These changes in ocean chemistry (e.g., salinity) coupled with variably restricted major ocean basins (e.g., Tethys and Arctic Oceans) could have resulted in substantial changes to global oceanic circulation and the more rapid mixing of the surface and intermediate ocean, particularly in those restricted basins, producing the ventilation or removal

of carbon from the large deep ocean reservoir and its subsequent addition to the much smaller atmospheric reservoir. These elevated temperatures and high precipitation greenhouse conditions would likely also result in the ventilation of lacustrine carbon from large continental basins (e.g., Lake Alemanía, Lake Gosiute; Whiteside et al., 2011; Hyland et al., 2013), via this same process. Unfortunately this additional carbon flux is not addressed here due to the limitations of the LOSCAR model in terms of modeling terrestrial carbon sources, but lacustrine sources would further amplify the carbon release effect caused by oceanic ventilation and would thereby enhance the overall carbon cycle impact of these greenhouse conditions.

As a result of this longer-term change in global paleoclimatic conditions caused by increased ventilation (which is reflected in marine records; e.g., Muttoni and Kent, 2007; Zachos et al., 2008), a transient carbon release from a relatively isotopically heavy source could cause the remaining peak EECO conditions like high atmospheric pCO_2 and elevated temperatures (which are reflected in terrestrial records; Figures 5.2 and 5.4). This carbon release, while still relatively transient in comparison to longer term carbon cycle forcings, likely occurred on a short to intermediate timescale (~100 kyr based on proxy records; Figure 5.2), and could be generated by sources such as rapid carbonate weathering. Rapid carbonate weathering could result from the same combination of global changes including: heightened greenhouse conditions, or the expansion of warm/wet environments that are conducive to rapid weathering (e.g., Bowen et al., 2004); concurrent changes in global paleogeography and increased equatorial uplift, such as the exposure of carbonate marine sediments within the Tethyan basin (e.g., Kent and Muttoni, 2008) that would provide readily weathered material; and changes in regional ocean chemistry, such as shifts in salinity and pH in restricted basins (e.g., Zeebe, 2012b; Norris et al., 2013) that would cause decreased rates of carbonate sedimentation or burial. Together these factors could have

resulted in a relatively short-term carbonate weathering event that produced a substantial flux of carbon from the large surface sediment reservoir to the much smaller atmospheric reservoir.

While this combined-mechanism scenario is plausible based on current modeling and available proxy data, more detailed carbon cycle modeling and proxy observations in the future will help elucidate the particular dynamics of the EECO, particularly in terms of the timescale of the peak event. Specifically, developing a coupled global circulation model (GCM) and isotope-enabled carbon cycle model using early Eocene boundary conditions would allow for the inclusion of many climate and carbon release/drawdown feedbacks that are otherwise missing from modeling efforts thus far (e.g., terrestrial carbon pools), and which may play an important role in modulating global responses to carbon cycle perturbations on intermediate to long timescales. Additionally, this preferred carbon scenario can be further tested by comparing other proxy observations to expected results from these modeling simulations, particularly in terms of marine preservation records and basin-specific carbon isotope stratigraphy, or in terms of terrestrial records of large lacustrine basins and increased hydrologic and carbon cycling.

5.6 CONCLUSIONS

A high-resolution multiproxy record of the early Eocene from the Southern Hemisphere at a site on the margin of the Salta Basin (Cerro Bayo) is presented, where new magnetostratigraphy of the Maíz Gordo Formation indicates that it is early Eocene in age and preserves a sequence of fluvial and paleosol sediments that correspond to the EECO. Multiproxy records from these paleosols record a peak period of carbon isotopic enrichment (up to 5‰ higher), increased MAT (up to 6°C higher), and increased MAP (up to 500 mm yr^{-1} higher) that is consistent with results from temperate Northern Hemisphere sites. When paired with marine

records of the EECO, these consistent responses provide a set of target observations for testing carbon cycle perturbation scenarios using the LOSCAR global carbon cycle model. Each of the previously suggested scenarios for generating the EECO was tested, and the target observations are matched most closely by increased oceanic ventilation. However, in order to predict fully the changes in the carbon cycle and global climatic and ecological responses to the EECO, a more complex combined scenario including both increased ventilation and an additional carbon source (e.g., carbonate weathering) is required. Additionally, these results suggest that further modeling of the EECO using more advanced modeling resources (coupled GCM and isotope-enabled carbon models including terrestrial carbon pools and a more complex ocean system) and more detailed proxy records may be necessary to understand fully the causes and feedbacks associated with carbon cycle dynamics during the EECO.

REFERENCES CITED

Bowen, G.J., Beerling, D.J., Koch, P.L., Zachos, J.C., and Quattlebaum, T., 2004, A humid climate state during the Palaeocene/Eocene thermal maximum: Nature, v. 432, p. 495–499.

Brinkhuis, H., Scouten, S., Collinson, M.E., Sluijs, A., Damste, J.S.S., Dickens, G.R., Huber, M., Cronin, T.M., Onodera, J., Takahashi, K., and the Expedition 302 Team, 2006, Episodic fresh surface waters in the Eocene Arctic Ocean: Nature, v. 441, p. 606–609.

Bryan, S.E., and Ferrari, L., 2013, Large igneous provinces and silicic large igneous provinces: Progress in our understanding over the last 25 years: Geological Society of America Bulletin, v. 125, p. 1053–1078.

Cotton, J.M., and Sheldon, N.D., 2012, New constraints on using paleosols to reconstruct atmospheric pCO_2: Geological Society of America Bulletin, v. 124, p. 1411–1423.

DeCelles, P.G., Carrapa, B., Horton, B.K., and Gehrels, G.E., 2011, Cenozoic foreland basin system in the Central Andes of northwestern Argentina: Implications for Andean geodynamics and modes of deformation: Tectonics, v. 30, p. 6013–6043.

Demicco, R.V., Lowenstein, T.K., and Hardie, L.A., 2003, Atmospheric pCO_2 since 60 Ma from records of seawater pH, calcium, and primary carbonate mineralogy: Geology, v. 31, p. 793–796.

Dickens, G.R., 2003, Rethinking the global carbon cycle with a large, dynamic and microbially mediated gas hydrate capacitor: Earth and Planetary Science Letters, v. 213, p. 169–183.

Fan, M., DeCelles, P.G., Gehrels, G.E., Dettman, D.L., Quade, J., and Peyton, S.L., 2011, Sedimentology, detrital zircon geochronology, and stable isotope geochemistry of the lower Eocene strata of the Wind River Basin, central Wyoming: Geological Society of America Bulletin, v. 123, p. 979–996.

Gallagher, T.M., and Sheldon, N.D., 2013, A new paleothermometer for forest paleosols and its implications for Cenozoic climate: Geology, v. 41, p. 647–650.

Gelfo, J.N., Goin, F.J., Woodburne, M.O., and Muizon, C.D., 2009, Biochronological relationships of the earliest South American Paleogene mammalian faunas: Palaeontology, v. 52, p. 251–269.

Gradstein, F.M., Ogg, J.G., Schmitz, M., and Ogg, G., 2012, The Geologic Time Scale 2012: Elsevier (Amsterdam, NED), pp. 1176.

Greenwood, D.R., and Wing, S.L., 1995, Eocene continental climates and latitudinal temperature gradients: Geology, v. 23, p. 1044–1048.

Held, I.M., and Soden, B.J., 2006, Robust responses of the hydrological cycle to global warming: Journal of Climate, v. 19, p. 5686–5699.

Hollis, C.J., Taylor, K.W.R., Handley, L., Pancost, R.D., Huber, M., Creech, J.B., Hines, B.R., Crouch, E.M., Morgans, H.E.G., Crampton, J.S., Gibbs, S., Pearson, P.N., and Zachos, J.C., 2012, Early Paleogene temperature history of the Southwest Pacific Ocean: Reconciling proxies and models: Earth and Planetary Science Letters, v. 350, p. 53–66.

Huber, M., and Caballero, R., 2011, The early Eocene equable climate problem revisited: Climate of the Past, v. 7, p. 603–633.

Hyland, E., and Sheldon, N.D., 2013, Coupled CO_2-climate response during the Early Eocene Climatic Optimum: Palaeogeography, Palaeoclimatology, Palaeoecology, v. 369, p. 125–135.

Hyland, E., Sheldon, N.D., and Fan, M., 2013, Terrestrial paleoenvironmental reconstructions indicate transient peak warming during the early Eocene climatic optimum: Geological Society of America Bulletin, v. 125, p. 1338–1348.
Intergovernmental Panel on Climate Change, 2007, Fourth Assessment Report: Climate Change (AR4): In Pachuari, R.K., and Reisinger, A. (Eds.), IPCC Geneva, Switzerland, 104 pp.
Jaramillo, C., and Cardenas, A., 2013, Global warming and Neotropical rainforests: A historical perspective: Annual Review of Earth and Planetary Sciences, v. 41, p. 741–766.
Kent, D.V., and Muttoni, G., 2008, Equatorial convergence of India and early Cenozoic climate trends: Proceedings of the National Academy of Sciences USA, v. 105, p. 16065–16070.
Kerrick, D.M., and Caldeira, K., 1999, Was the Himalayan orogeny a climatically significant coupled source and sink for atmospheric CO_2 during the Cenozoic?: Earth and Planetary Science Letters, v. 173, p. 195–203.
Krause, J.M., Bellosi, E.S., and Raigemborn, M.S., 2010, Lateritized tephric palaeosols from Central Patagonia, Argentina: a southern high-latitude archive of Palaeogene global greenhouse conditions: Sedimentology, v. 57, p. 1721–1749.
Marquillas, R.A., Del Papa, C., and Sabino, I.F., 2005, Sedimentary aspects and paleoenvironmental evolution of a rift basin: Salta Group (Cretaceous-Paleogene), northwestern Argentina: International Journal of Earth Sciences, v. 94, p. 94–113.
McInerney, F.A., and Wing, S.L., 2011, The Paleocene-Eocene Thermal Maximum: a perturbation of carbon cycle, climate, and biosphere with implications for the future: Annual Reviews in Earth and Planetary Sciences, v. 39, p. 489–516.
Muttoni, G., and Kent, D.V., 2007, Widespread formation of cherts during the Early Eocene Climatic Optimum: Palaeogeography, Palaeoclimatology, Palaeoecology, v. 253, 348–362.
Norris, R.D., Turner, S.K., Hull, P.M., and Ridgewell, A., 2013, Marine ecosystem responses to Cenozoic global change: Science, v. 341, p. 492–498.
Quattrocchio, M.E., and Volkheimer, W., 2000, Paleoclimatic changes during the Paleocene-Lower Eocene in the Salta Group Basin, NW Argentina: In Volkheimer, W., and Smelka, A. (Eds.), Southern Hemisphere Paleo- and Neoclimates: Key sites, data and models, Springer (New York, USA), pp. 353–367.
Ramón, M.J., and Pueyo, E.L., 2008, Cálculo de direcciones y planos virtuales paleomagnéticas: Ejemplos y comparación con otros métodos: Geotemas, v. 10, p. 1203–1206.
Rohling, E.J., Sluijs, A., Dijkstra, H.A., and PALAEOSENS Project Members, 2012, Making sense of palaeoclimate sensitivity: Nature, v. 491, p. 683–691.
Royer, D.L., Wing, S.L., Beerling, D.J., Jolley, D.W., Koch, P.L., Hickey, L.J., and Berner, R.A., 2001, Paleobotanical evidence for near-present-day levels of atmospheric CO_2 during part of the Tertiary: Science, v. 292, p. 2310–2313.
Salfity, J.A., and Monaldi, C.R., 2006, Hoja Geologica 2566-IV: Metan: SEGEMAR Boletin, v. 319, p. 1–80.
Scotese, C.R., 2000, Earth System History Geographic Information System, ArcView 3.2v2.0c.
Self, S., Thordarson, T., and Widdowson, M., 2005, Gas fluxes from flood basalt eruptions: Elements, v. 1, p. 283–287.
Sheldon, N.D., Retallack, G.J., and Tanaka, S., 2002, Geochemical climofunctions from North American soils and application to paleosols across the Eocene-Oligocene boundary in Oregon: Journal of Geology, v. 110, p. 687–696.

Sheldon, N.D., Costa, E., Cabrera, L., and Garcés, M., 2012, Continental climatic and weathering response to the Eocene-Oligocene Transition: Journal of Geology, v. 120, p. 227–236.

Shellito, C.J., Sloan, L.C., and Huber, M., 2003, Climate model sensitivity to atmospheric CO_2 levels in early-middle Paleogene: Palaeogeography, Palaeoclimatology, Palaeoecology, v. 193, p. 113–123.

Schrag, D.P., Higgins, J.A., Macdonald, F.A., and Johnston, D.T., 2013, Authigenic carbonate and the history of the global carbon cycle: Science, v. 339, p. 540–543.

Sluijs, A., Rohl, U., Schouten, S., Brumsack, H.J., Sangiorgi, F., Damste, J.S.S., and Brinkhuis, H., 2008, Arctic late Paleocene-early Eocene paleoenvironments with special emphasis on the Paleocene-Eocene thermal maximum: Paleoceanography, v. 23, PA1S11.

Sluijs, A., Zeebe, R.E., Bijl, P.K., and Bohaty, S.M., 2013, A middle Eocene carbon cycle conundrum: Nature Geoscience, v. 6, p. 429–434.

Smith, M.E., Carroll, A.R., and Mueller, E.R., 2008, Elevated weathering rates in the Rocky Mountains during the Early Eocene Climatic Optimum: Nature Geoscience, v. 1, p. 370–374.

Thrasher, B.L., and Sloan, L.C., 2009, Carbon dioxide and the early Eocene climate of western North America: Geology, v. 37, p. 807–810.

Thrasher, B.L., and Sloan, L.C., 2010, Land cover influences on the regional climate of western North America during the early Eocene: Global and Planetary Change, v. 72, p. 25–31.

Whiteside, J.H., Olsen, P.E., Eglinton, T.I., Cornet, B., McDonald, N.G., Huber, P., 2011, Pangean Great Lake paleoecology on the cusp of the end-Triassic extinction: Palaeogeography, Palaeoclimatology, Palaeoecology, v. 301, p. 1–17.

Wilf, P., Cuneo, N.R., Johnson, K.R., Hicks, J.F., Wing, S.L., and Obradovich, J.D., 2003, High plant diversity in Eocene South America: evidence from Patagonia: Science, v. 300, p. 122–125.

Woodburne, M.O., Goin, F.J., Bond, M., Carlini, A.A., Gelfo, J.N., Lopez, G.M., Iglesias, A., Zimicz, A.N., 2014, Paleogene land mammal faunas of South America: A response to global climatic changes and indigenous floral diversity: Journal of Mammalian Evolution, v. 21, p. 1–73.

Zachos, J.C., Pagani, M., Sloan, L.C., Thomas, E., and Billups, K., 2001, Trends, rhythms, and aberrations in global climate 65 Ma to the present: Science, v. 292, p. 686–693.

Zachos, J.C., Dickens, G.R., and Zeebe, R.E., 2008, An early Cenozoic perspective on greenhouse warming and carbon-cycle dynamics: Nature, v. 451, p. 279–283.

Zeebe, R.E., Zachos, J.C., and Dickens, G.R., 2009, Carbon dioxide forcing alone insufficient to explain Paleocene-Eocene Thermal Maximum warming: Nature Geoscience, v. 2, p. 576–580.

Zeebe, R.E., 2012, LOSCAR: Long-term Ocean-atmosphere-Sediment CArbon cycle Reservoir Model v2.0.4: Geoscientific Model Development, v. 5, p. 149–166.

Zeebe, R.E., 2012, History of seawater carbonate chemistry, atmospheric CO_2, and ocean acidification: Annual Review of Earth and Planetary Science, v. 40, p. 141–165.

CHAPTER VI

Conclusions: The Early Eocene Climatic Optimum

This chapter summarizes the central results of each of the previous data chapters, presents overall conclusions with regard to the Early Eocene Climatic Optimum, places these conclusions and contributions within the context of the current understanding of Paleogene climate, and proposes future research and modeling directions for expanding knowledge of the climatic, ecological, and environmental conditions surrounding the EECO.

6.1 SUMMARY OF CONCLUSIONS

6.1.1 Chapter 2

This chapter presents the first high-resolution multiproxy record of terrestrial climatic conditions from the early Eocene. It focuses on the Green River/Great Divide Basin of Wyoming, and describes fluvial and floodplain environments along the margin of paleo-Lake Gosiute. These floodplains show evidence of large scale continuous soil development, distinct horizonation, and features comparable primarily to modern Alfisols, which provide excellent records of regional paleoclimate. Our data from a wide variety of proxies (paleopedology and sedimentology, paleosol geochemistry, stable isotope analyses) show that during the EECO, regional climate was characterized as warm-temperate and semi-arid to sub-humid, with a peak interval of about 0.5 Myr that exhibited warmer (~7˚C) and significantly wetter (~750 mm yr^{-1}) conditions that resulted in major changes in the local weathering regime. This chapter also

presents paleobarometric estimates from this site, which show a rapid 3–5× increase to high atmospheric pCO_2 values (>1500 ppmV) and appear to define and provide a cause for this peak interval of major regional climatic change, suggesting that the broad-scale EECO may contain a shorter-term and more aberrant hyperthermal "maximum" than previously documented in marine records (~4°C temperature change over 2 Ma). Additionally, this chapter helps constrain the dynamics of early Eocene climate by providing evidence of near-modern temperature-CO_2 sensitivities (2.8°C warming per doubling of atmospheric pCO_2).

6.1.2 Chapter 3

This chapter builds on the work of the previous chapter by developing a new paleosol-based method for high-resolution reconstructions of paleoclimatic conditions using a record from the Green River Basin during the early Eocene as a case study. Specifically, the chapter describes the study of magnetic properties such as the ratio of pedogenic goethite to hematite in a suite of modern soil samples from a large range of climatic conditions in order to develop a new proxy for paleoprecipitation. Our results suggest that goethite-hematite ratios of modern soil B-horizons can be related quantitatively to modern precipitation regimes worldwide via a highly significant ($p < 0.001$) and extremely strong ($R^2 = 0.96$) linear regression model. Based on this relationship, we present a newly derived paleoprecipitation climofunction that is applicable to a wide range of soil types and climatic regimes worldwide. As a case study, we apply this relationship to the same paleosols described in Chapter 2 from the Green River Basin in order to test the relationship against previously published estimates and provide a higher-resolution record of paleoprecipitation during the Early Eocene Climatic Optimum in North America.

6.1.3 Chapter 4

This chapter expands upon North American high-resolution multiproxy records of the EECO by developing a new comparison point for the data presented in Chapters 2 and 3, this

time from the paleomargin of the Wind River Basin (Eocene Wind River Formation). Similar to the Green River Basin, the Wind River Basin was also a fluvial distributary system characterized by channels and floodplain paleosol development, which means it provides an excellent regional comparison point for climatic and ecological changes during the EECO. Multiproxy records from these paleosols describe a short peak period of < 1 Ma (~51 Mya) during which carbon isotopic enrichment (up to 2‰ higher) and elevated atmospheric pCO_2 (~2–3× increase), high MAT (up to 8 °C higher), increased MAP (up to 500 mm yr^{-1} higher), and shifts (up to 10%) in floral assemblage composition derived from phytolith assemblages more fully describe regional responses to the previously defined EECO maxima (e.g., Chapter 2). This record agrees well with our other terrestrial records of the EECO, and along with these western basin records may provide a detailed account of the ways in which topographically complex regions like western North America respond to global climatic events. Additionally, the rapidity and dynamics of change during the peak climatic and environmental change interval in this Wind River record further suggests that the terrestrial response to the EECO was transient and may have resulted from short-term drivers like changes in oceanic carbon ventilation instead of long-term trends like volcanism and silicate weathering.

6.1.4 Chapter 5

This final results chapter presents the first high-resolution multiproxy record of the early Eocene from the Southern Hemisphere and compares this record to Northern Hemisphere sites in order to develop a global carbon cycle model by which to assess causal mechanisms for the EECO. This record comes from a site on the margin of the Salta Basin (Cerro Bayo), where we show based on both biostratigraphy and magnetostratigraphy that the Maíz Gordo Formation is early Eocene in age and contains a sequence of fluvial and paleosol sediments that correspond to

the EECO. Multiproxy records from these paleosols describe a peak period of carbon isotopic enrichment (up to 5‰ higher), increased MAT (up to 6°C higher), and increased MAP (up to 500 mm yr^{-1} higher), consistent with the temperate Northern Hemisphere sites detailed in Chapters 2–4. When paired with marine records of the EECO, these consistent responses provide a set of target observations for testing carbon cycle perturbation scenarios using the LOSCAR global carbon cycle model. We test a series of previously suggested scenarios including increased volcanism, methane releases, carbonate weathering/metamorphism, and oceanic carbon ventilation, and find that our target observations are matched most closely by increased oceanic carbon ventilation via mixing. However, we suggest that in order to predict fully carbon cycle changes and global climatic and ecological responses to the EECO, a more complex combined scenario including both increased ventilation and inputs from increased carbonate weathering may be more appropriate. Additionally, these results suggest that further modeling of the EECO using more advanced modeling resources (coupled GCM and isotope-enabled carbon models) may be necessary to understand fully the causes and feedbacks associated with carbon cycle dynamics during the EECO (particularly in terms of terrestrial carbon pools and large lacustrine basins).

6.2 CONTRIBUTIONS AND FUTURE WORK

Due to the unabated use of fossil fuels and continued increases in atmospheric greenhouse gas concentrations, examining past periods of extreme climate change and high CO_2 values such as the EECO is crucial for understanding future changes in important systems like the hydrological cycle or ecological gradients. By improving our understanding of terrestrial climatological and ecological conditions and generating effective models for predicting changes

to these systems during warming periods, we may also be able to contribute to the development of prevention strategies and mitigation practices in the face of continued change and impending future impacts. This dissertation represents a substantial advancement in our understanding of early Eocene climate dynamics, particularly in terms of overall causes of major global changes and their terrestrial impacts during this and other periods of substantial warming. The EECO is of particular importance for the scientific community, because even though the timescale of change is significantly longer (Figure 6.1), it is potentially the best available analogue for overall environmental conditions under a future continued high-emissions/non-mitigation climate change scenario (Scenarios IV through VI; IPCC, 2014). The dearth of high-resolution climatic and environmental proxy information for the EECO had previously resulted in disagreement amongst paleoclimate models and paleoecological predictions, and had led to uncertainty about feedback mechanisms and boundary conditions in global systems during elevated greenhouse periods, conditions which may not have been experienced since the early Eocene.

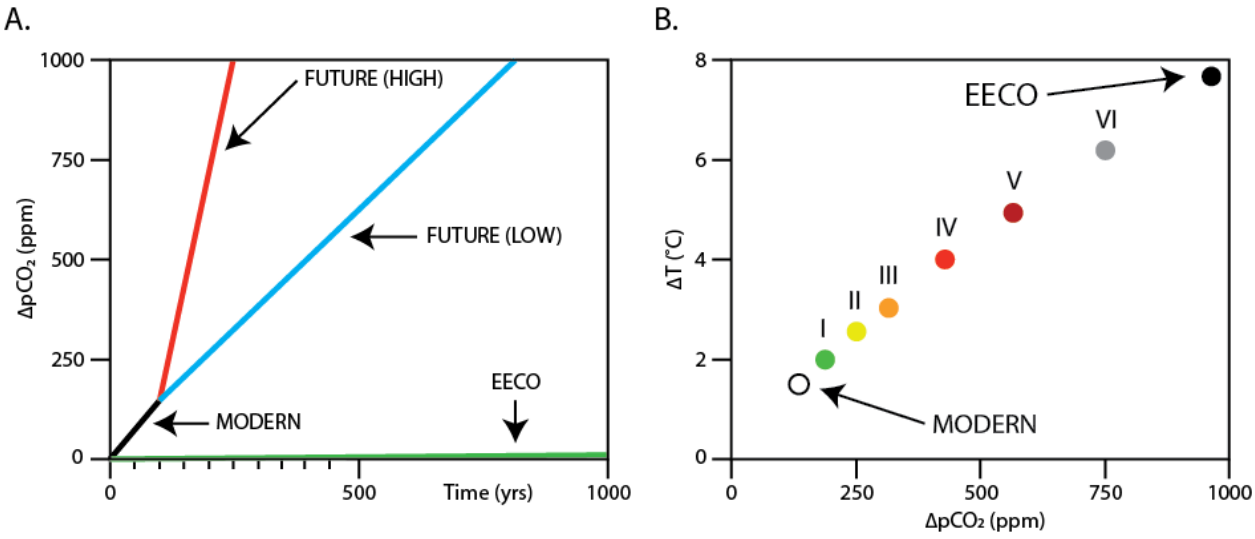

Figure 6.1 Comparison of the early Eocene (e.g., Hyland and Sheldon, 2013) and future climate projections (IPCC, 2014) based on A) rate of change of atmospheric carbon dioxide concentrations, and B) magnitude of overall change in temperature and carbon dioxide concentrations. Note in Panel A, rate of change for EECO is ~ 10 ppm kyr^{-1}. In Panel B, colored/numbered points correspond to IPCC projections for a range of possible emission scenarios.

The data, models, and interpretations generated herein have helped examine the climate system in a number of key ways, including: 1) developing the first high-resolution multiproxy record of terrestrial events during the Early Eocene Climatic Optimum, 2) highlighting the discrepancy between terrestrial and marine timescales of the EECO event, 3) presenting the first proxy-based estimates of early Eocene climate sensitivity, 4) developing a new paleosol-based paleoprecipitation proxy that is applicable to the widest range of potential environments and climatic regimes, 5) developing a series of high-resolution climatic and ecological records from western North America in order to examine regional response patterns during warming events, 6) expanding these records to South America in order to compare temperate terrestrial response patterns between hemispheres, 7) developing a new long-term ocean-atmosphere-sediment carbon cycle reservoir model for the early Eocene (LOSCAR "preEECO" simulation), and 8) model testing the full range of suggested EECO carbon cycle scenarios in order to constrain better the underlying causal mechanism for this major climatic and ecological event. These specific contributions have greatly improved our understanding of the processes and dynamics that led to the major climatic and ecological events of the early Eocene, and have provided a better understanding of the role of the terrestrial realm in the overall global climate system.

This dissertation has also led to a number of other research questions focused on addressing more global dynamics of the early Eocene, particularly in terms of filling in global data gaps and linking proxy data with model simulations. These research questions and related potential future research projects include:

1) *Are early Eocene latitudinal temperature gradients comparable to the modern?*

   High-resolution terrestrial proxies have resolved some of the remaining model-proxy discrepancies in temperate regions (e.g., Chapter 5), but limited proxy data coverage in

both polar and equatorial regions has left open many questions regarding latitudinal gradients and zonal climates during the EECO (cf. Greenwood and Wing, 1995; Huber and Caballero, 2011). In order to address this question directly, I intend to develop high-resolution multiproxy terrestrial records from both polar (Canadian Arctic Archipelago) and equatorial (Saudi Arabia, Columbia) sites in collaboration with a broad group of researchers. Combined with the available temperate region multiproxy records, these polar and equatorial reconstructions will allow for side by side comparisons of model and data-based latitudinal gradients for both the early Eocene and the modern.

2) *How do new causal mechanisms and terrestrial proxy data affect early Eocene model results from global circulation models (GCMs)?* Global circulation models simulating conditions during the EECO have been largely unable to predict the conditions reconstructed from proxy data for this time period. New proxy data records and improved global data coverage, as well as new ideas of causal mechanisms and carbon cycle dynamics during the event, may allow for better constraints while developing GCM results for the early Eocene. GCM and isotope-enabled modeling of the EECO is something I intend to pursue in the future in collaboration with a group of modelers.

3) *How can terrestrial proxy records help inform paleoclimate models and improve data-model synthesis for major climate change events?* Many paleoclimate models are currently forced by oceanic and atmospheric parameters with limited input from the terrestrial realm, and nearly all current carbon cycle models include terrestrial reservoirs and systems as one-dimensional fluxes. New high-resolution terrestrial proxy records and new paleosol-based proxy methods may allow for better constraints on many of the terrestrial conditions and feedbacks that are now either ignored or greatly simplified in

modeling studies, and may improve data-model synthesis and agreement for a wide range of past climate change events. In order to address this topic, I intend to continue expanding terrestrial paleoclimate proxy records to a range of other time periods throughout the Cenozoic (e.g., Paleocene, Oligocene, Miocene–Pliocene, etc.), as well as continuing to use and improve carbon cycle modeling platforms (e.g., LOSCAR) particularly in terms of their terrestrial dynamics.

In conclusion, both terrestrial proxy records and the Early Eocene Climatic Optimum are important topics in the realm of paleoclimatic and paleoecological research, and will continue to be a major part of my academic career in the future, whatever that may be…

- Ethan G. Hyland

Appendix A1. Table of isotopic analyses

Sample	Height (m)	$\delta^{13}C_{org}$ (‰ VPDB)	$\delta^{13}C_{cc}$ (‰ VPDB)[a]	$\delta^{18}O$ (‰ VPDB)[a]
128B	35.5	------	-5.50	-4.74
128C	35.5	------	-5.43	-5.00
187B	113	------	-6.80	-8.02
187C	113	------	-6.62	-8.79
D10	55	------	-10.82	-12.07
D20	55	-21.24	-6.15	-4.42
HB14	24.5	-25.61	-7.69	-9.18
HB15	24.5	-24.04	-9.00	-10.78
HB18	26	-23.84	-6.73	-8.94
HB30	46.5	-22.72	-6.85	-5.10
HB47	61	-22.67	-5.70	-5.13
HB74	92	-22.73	-7.27	-7.22
HB79	94.5	------	-6.62	-9.67
HB81	94.5	-23.14	-6.13	-4.09
HB87	101	-22.82	-14.01	-12.44
HB96	4	-23.20	-8.90	-9.96
HB105	14.5	-23.20	-11.31	-10.28
HB109	3	-21.73	-6.54	-5.67
HB110	1.5	-22.50	-9.30	-11.02
HB121	32	-22.55	-11.01	-14.73
HB124	34	-22.72	-10.25	-10.83
HB128	35.5	-22.08	-5.36	-5.15
HB129	41	-10.86	-6.33	-5.41
HB141	46	-23.32	-7.89	-7.69
HB143	47.5	-21.65	-8.17	-11.50
HB154	72	-23.12	-8.54	-7.93
HB162	79	-22.98	-7.48	-8.49
HB162.5	82.5	-22.06	-8.03	-7.13
HB168	87.5	-23.16	-7.69	-10.30
HB170	95	-21.28	-6.46	-5.44
HB176	101	-23.49	------	------
HB180	107	-22.83	------	------
HB185	109.5	------	-5.47	-7.48
HB187	113	------	-6.50	-5.16

a Reported values are averages of multiple analyses on individual nodules.

Appendix A1. Table of isotopic analyses (cont'd)

Sample	$\delta^{13}C_{cc}$ (‰ VPDB)	$\delta^{18}O$ (‰ VPDB)	Sample	$\delta^{13}C_{cc}$ (‰ VPDB)	$\delta^{18}O$ (‰ VPDB)
HB162.1	-8.02	-9.82	HB128.1	-5.33	-5.04
HB162.2	-6.94	-7.23	HB128.2	-5.41	-5.22
HB162.3	-7.50	-8.44	HB128.3	-5.36	-5.21
HB162.5.1	-8.08	-7.09	HB170.1	-6.29	-5.03
HB162.5.2	-8.48	-7.07	HB170.2	-6.84	-6.31
HB162.5.3	-7.55	-7.24	HB170.3	-6.27	-4.99
187C.1	-6.59	-8.92	HB47.1	-5.71	-5.14
187C.2	-6.63	-8.87	HB47.1.1	-5.66	-5.13
187C.3	-6.64	-8.60	HB47.2	-5.78	-5.08
HB15.1	-8.80	-10.86	HB47.3	-5.69	-5.18
HB15.2	-9.28	-10.76	HB121.1	-10.00	-14.79
HB15.3	-8.94	-10.74	HB121.2	-10.01	-14.79
D20.1	-6.18	-4.36	HB121.3	-12.05	-14.76
D20.1.2	-6.17	-4.34	HB121.3.3	-12.01	-14.61
D20.2	-6.12	-4.43	HB143.1	-9.75	-12.72
D20.2.2	-6.14	-4.31	HB143.2	-8.79	-12.26
D20.3	-6.17	-4.68	HB143.3	-5.98	-9.54
D10.1	-10.12	-12.17	HB14.1	-5.85	-8.95
D10.2	-10.69	-12.31	HB14.2	-8.20	-9.21
D10.3	-11.67	-11.74	HB14.2.2	-8.30	-9.38
HB110.1	-8.58	-10.13	HB96.1	-8.44	-9.26
HB110.2	-8.59	-10.38	HB96.2	-9.37	-10.67
HB110.3	-10.02	-11.86	HB124.1	-9.89	-10.22
HB110.3.1	-10.05	-11.75	HB124.2	-10.61	-11.44
HB74.1	-10.24	-11.73	128C.1	-5.38	-5.16
HB74.2	-5.86	-5.24	128C.1.1	-5.42	-5.04
HB74.3	-5.73	-4.70	128C.2	-5.49	-5.20
HB81.1	-6.06	-4.12	128C.3	-5.46	-4.87
HB81.2	-6.09	-4.21	128C.3.3	-5.44	-4.73
HB81.3	-6.26	-3.96	128B.1	-5.47	-4.76
HB187.1	-6.37	-4.76	128B.2	-5.50	-4.63
HB187.1.1	-6.38	-4.67	128B.3	-5.53	-4.84
HB187.2	-6.76	-6.26	HB109.1	-5.68	-5.21
HB187.3	-6.51	-4.97	HB109.2	-5.65	-5.24
HB18.1	-6.73	-8.92	HB109.3	-8.31	-6.58
HB18.2	-6.79	-9.06	HB154.1	-7.97	-6.61
HB18.3	-6.69	-8.86	HB154.2	-9.12	-9.26
HB79.1	-5.98	-9.88	HB168.1	-9.26	-9.40
HB79.2	-6.31	-9.99	HB168.2	-9.79	-13.09
HB79.2.2	-6.08	-9.95	HB168.3	-5.86	-9.46
HB79.3	-8.12	-10.94	HB168.3.3	-5.87	-9.27
HB30.1	-6.86	-5.53	HB87.1	-14.66	-12.10
HB30.2	-6.86	-4.69	HB87.2	-12.98	-12.88
HB141.1	-6.73	-4.85	HB87.3	-14.42	-12.35
HB141.2	-9.05	-10.54	HB105.1	-11.39	-9.96
187B.1	-6.81	-8.02	HB105.2	-11.05	-10.52
187B.2	-6.80	-8.04	HB105.3	-11.48	-10.38
187B.2.2	-6.78	-8.09	HB185.1	-5.30	-6.66
187B.3	-6.81	-8.04	HB185.1.1	-5.24	-6.50
187B.3.3	-6.81	-7.92	HB185.2	-5.59	-8.38
HB129.1	-6.12	-4.89	HB185.3	-5.76	-8.39
HB129.2	-6.76	-6.29			
HB129.3	-6.13	-5.07			

Appendix A2. Table of elemental analyses

Sample	Horizon	SiO_2	TiO_2	Al_2O_3	Fe_2O_3	MgO	CaO	Na_2O	K_2O	P_2O_5	LOI	Total
						wt %						
HB-10	A	58.7	0.77	15.43	5.74	3.14	0.8	1.94	2.38	0.221	10.4	99.66
HB-11	A	56.28	0.79	16.21	7.42	3.05	0.81	1.85	2.4	0.105	10.85	99.91
HB-12	B	49.63	0.82	17.03	8.12	3.63	0.84	2.12	2.14	0.098	15.25	99.81
HB-13	C	62.07	0.45	8.7	1.75	1.04	11.18	1.61	1.74	0.139	11	99.91
HB-50	A	56.29	0.77	16.56	6.94	2.83	0.62	1.54	2.66	0.159	11.05	99.55
HB-51	A	57	0.77	16.41	6.89	2.79	0.82	1.57	2.69	0.123	10.9	100.1
HB-52	B	58.52	0.75	15.8	6.52	2.59	0.59	1.56	2.89	0.082	10.65	100.05
HB-53	B	58.08	0.69	15.1	6.3	2.58	0.58	1.55	3.03	0.094	11.05	99.18
HB-54	B	54.3	0.7	14.91	6.12	2.85	2.41	1.63	2.78	0.179	12.85	98.88
HB-55	B	51	0.63	13.24	5.44	2.71	6.88	1.71	2.36	0.169	15.55	99.94
HB-57	A	64.77	0.6	11.88	3.99	1.86	4.23	1.6	2.47	0.17	8.42	100.2
HB-58	A	57.71	0.74	15.88	7.6	2.49	0.65	1.51	2.57	0.171	10.65	100.1
HB-59	B	49.22	0.65	14.59	6.27	2.65	7.28	1.22	2.46	0.286	15.1	99.93
HB-60	B	58.6	0.79	15.5	6.82	2.58	0.47	1.6	2.64	0.104	9.47	98.71
HB-61	B	63.56	0.71	13.76	6.3	2.29	0.72	1.59	2.53	0.091	7.82	99.51
HB-73	C	72.41	0.54	11.23	3.31	1.45	1.47	2.16	2.32	0.071	5.11	100.2
HB-75	C	70	0.51	11.56	3.71	1.71	0.94	2.21	2.36	0.043	6.59	99.78
HB-76	A	58	0.66	14.88	7.09	2.86	0.56	1.7	2.77	0.094	11.5	100.25
HB-77	A	62.5	0.52	12.8	5.12	2.26	1.32	1.88	2.74	0.151	10.3	99.72
HB-78	B	49.18	0.37	9.43	3.13	1.9	13.78	1.64	2.01	0.384	17.55	99.73
HB-130	A	58.97	0.71	15.88	6.49	2.51	0.77	2.05	2.76	0.211	9.66	100.15
HB-131	A	61.45	0.58	14.53	5.23	2.13	1.36	2.06	2.9	0.113	9.72	100.2
HB-132	B	56.5	0.56	14.23	5.35	2.25	3.3	2.22	2.85	0.103	12.35	99.88
HB-133	B	60.38	0.57	14.69	5.55	2.34	0.61	2.15	2.96	0.082	10.7	100.2
HB-134	B	69.17	0.42	12.44	3.86	1.41	0.69	2.37	2.58	0.036	6.65	99.77
HB-135	C	74.09	0.24	11.3	1.58	1.01	0.84	2.98	2.34	0.046	5.13	99.8
HB-179	A	59	0.74	14.71	6.42	2.47	0.4	2.07	3.07	0.105	10.95	100.05
HB-180	A	59.24	0.67	13.77	6.07	2.21	2.06	1.9	2.8	0.112	10.95	99.93
HB-181	B	54.98	0.67	14.9	6.96	2.52	0.93	2.14	2.85	0.106	12.8	98.97
HB-182	B	50.57	0.62	14	6.62	2.38	5.08	2.04	2.53	0.152	15.3	99.47
HB-183	B	58.36	0.74	14.96	6.22	2.33	0.83	2.06	2.49	0.176	11.4	99.67

Δ-1	A	55.17	0.77	17.03	7.64	2.93	0.45	1.6	2.79	0.099	11.25	99.84
Δ-2	A	59.2	0.77	15.74	6.44	2.73	0.52	1.78	2.89	0.105	9.6	99.9
Δ-3	B	57.5	0.72	15.81	6.17	2.86	0.8	1.38	3.28	0.125	10.9	99.67
Δ-4	B	59.17	0.7	14.73	5.95	2.83	1.24	1.63	2.96	0.183	10.65	100.15
Δ-5	A	51.56	0.6	11.6	4.17	2	10.2	2.02	2.16	0.185	15.1	100.05
Δ-6	A	55.52	0.73	15.87	6.55	2.89	0.49	2.14	3	0.122	12.25	99.69
Δ-7	B	52.01	0.68	15.01	5.98	2.64	4.26	1.47	3.01	0.207	13.35	98.82
Δ-8	B	54.1	0.71	16.11	6.83	2.92	1.65	1.32	3.5	0.216	12.2	99.69
Δ-9	B	50	0.63	13.45	5.67	2.58	6.78	1.53	2.69	0.258	16.3	100.15
Δ-11	C	59.88	0.55	11.59	4.07	1.82	6.21	1.72	2.14	0.24	11.35	99.79
Δ-12	A	55	0.77	16.27	6.64	2.84	0.98	2.19	2.76	0.167	12.35	100.1
Δ-13	A	57.71	0.76	16.06	6.75	2.64	0.62	1.51	3.06	0.103	10.6	99.94
Δ-14	B	58.59	0.75	15.08	5.88	2.5	0.61	1.45	3.3	0.08	10.6	98.96
Δ-15	B	54.35	0.69	14.44	5.98	2.64	3.72	1.54	2.84	0.229	12.95	99.55
Δ-16	A	52.1	0.73	15.95	7.22	2.77	2.14	2.12	2.62	0.211	13.7	99.72
Δ-17	A	62.49	0.64	14.73	5.94	2.17	0.76	1.82	2.58	0.106	8.57	99.94
Δ-18	B	63	0.55	13.6	5.28	2.19	0.84	1.67	3.1	0.07	9.45	99.88
Δ-19	B	55.2	0.52	10.83	4.53	2.1	8.15	1.86	2.19	0.164	13.9	99.69
Δ-21	C	69.5	0.56	11.59	3.39	1.91	1.51	2.08	2.35	0.2	6.79	100.05
Δ-22	A	54.02	0.78	15.97	6.91	2.78	0.6	2.37	2.56	0.11	12.5	98.73
Δ-23	A	61.2	0.63	15.05	5.82	2.35	0.51	1.71	3.02	0.081	9.4	99.9
Δ-24	B	62.5	0.61	14.11	5.42	2.42	0.98	1.37	3.14	0.089	9.23	99.99
Δ-25	B	58	0.6	12.91	5.8	3.18	3.3	1.46	2.8	0.133	11.65	99.99
Δ-26	A	53.5	0.8	17.59	8.65	3	0.58	1.3	2.76	0.118	11.45	99.89
Δ-27	A	56.41	0.73	16.17	6.73	2.77	1.09	1.42	3.14	0.112	11	99.7
Δ-28	B	61	0.67	15.16	5.41	2.51	0.74	1.49	3.17	0.098	9.5	99.88
Δ-29	B	55	0.71	15.5	6.97	3.1	1.1	1.62	3.25	0.149	12	99.51
Δ-30	A	53.48	0.75	16.39	7.21	2.84	0.6	2.04	2.68	0.094	13.15	99.38
Δ-31	A	57.09	0.68	15.08	6.38	2.76	0.85	1.65	2.97	0.098	12.15	99.82
Δ-32	B	57.5	0.68	14.48	6	2.8	1.18	1.58	3.04	0.095	12.3	99.78
Δ-33	B	62.5	0.61	12.78	5.21	2.23	1.73	1.65	2.88	0.094	10.05	99.92
Δ-34	A	56.22	0.73	16.56	7.59	2.66	0.56	1.74	2.8	0.115	10.6	99.72
Δ-35	A	55.5	0.7	15.33	6.91	2.77	1.84	1.76	2.96	0.136	11.95	100

Δ-36	B	55.69	0.68	14.53	6	2.58	3.47	1.34	2.91	0.107	12.1	99.59
Δ-37	B	57.18	0.69	14.56	6.26	2.7	0.87	1.61	2.98	0.102	11.4	98.48
Δ-38	A	55.07	0.79	17.29	7.51	2.94	0.54	1.44	2.81	0.135	11.25	99.9
Δ-39	B	55.5	0.74	16.55	7.2	3.07	0.42	1.56	3.17	0.112	11.6	100.05
Δ-40	B	54.5	0.67	15	6.64	2.8	2.88	1.65	3.02	0.206	12.3	99.82
Δ-41	B	53.23	0.64	14.8	6.75	2.89	2.8	1.51	3.02	0.139	13	98.93
Δ-42	A	60.75	0.68	15.62	6.93	2.32	0.39	1.63	2.57	0.07	8.87	99.96
Δ-43	A	59.09	0.71	15.8	6.83	2.44	0.47	1.76	2.67	0.096	9.75	99.76
Δ-44	A	54.37	0.74	16.63	7.31	2.94	0.56	2.08	2.68	0.114	12.7	100.25
Δ-45	B	63	0.58	13.63	5.54	2.23	0.71	2.03	2.89	0.115	9.16	100.05
Δ-46	B	51	0.56	11.85	5.24	4.23	6.37	1.77	2.53	0.114	15.8	99.71

Appendix A3. Table of horizon depths and thicknesses

Sample	Height (m)	Pedotype	Depth to Bk (cm)	Bk thickness (cm)	Nodule size (cm)
Δ-10	55	Sweetwater	230	10	3
Δ-20	55	Sweetwater	190	30	3
HB-14/15	24.5	Honeycomb	60	15	1
HB-18	26	Honeycomb	50 (T)	---	---
HB-30	46.5	Honeycomb	85	40	1.5
HB-47	61	Killpecker	0 (T)	---	---
HB-64	76	Killpecker	10 (T)	---	---
HB-74	92	Sweetwater	110	50	2
HB-79	94.5	Sweetwater	90	45	4
HB-81	94.5	Killpecker	0 (T)	---	2.5
HB-87	101	Killpecker	0 (T)	---	---
HB-96	4	Honeycomb	35	15	1
HB-105	14.5	Sweetwater	90	50	---
HB-109	3	Honeycomb	40	25	2
HB-110	1.5	Honeycomb	50	10	2.5
HB-121	32	Killpecker	20	30	2
HB-124	34	Honeycomb	20	30	---
HB-128	35.5	Killpecker	0 (T)	---	2.5
HB-129	41	Sweetwater	230	50	4
HB-141	46	Killpecker	35	10	2
HB-143	47.5	Honeycomb	40	10	---
HB-154	72	Sweetwater	160	45	1
HB-162	79	Honeycomb	40	30	---
HB-162.5	82.5	Honeycomb	60	40	2.5
HB-168	87.5	Honeycomb	55	20	3
HB-170	95	Honeycomb	65	50	3.5
HB-185	109.5	Killpecker	0 (T)	---	---
HB-187	113	Honeycomb	85	60	1.5

(T) represents profiles with known truncation of the paleosol surface

Appendix B1. Table of modern soil sites and climatic variables including literature sources

Sample[a]	Location[b]	G/H ratio	MAP (mm/yr)	MAT (˚C)	RMMP[c] (mm/yr)
1.01	Wongan Hills, WA (Austr.)	0.53	405	25.7	61
1.02	Narrogin, WA (Austr.)	0.35	475	22.4	74
1.03	Pickering, WA (Austr.)	1.00	950	22.5	184
1.04	Dawesville, WA (Austr.)	1.00	1120	23.1	117
1.05	Dudinin, WA (Austr.)	0.55	370	23.2	59
1.06	Boyup Brook, WA (Austr.)	0.74	690	22.8	104
1.07	Bridgetown, WA (Austr.)	0.18	425	22.4	131
1.08	Bannister, WA (Austr.)	0.40	440	23.7	114
1.09	Marradong, WA (Austr.)	0.58	645	23.7	128
1.10	Frankland River, WA (Austr.)	0.19	365	21.0	82
2.01	Montilla, COR (Spain)	0.56	600	16.5	84
2.02	Montilla, COR (Spain)	0.63	600	16.5	84
3.01	Albion, NE (USA)	0.53	710	9.1	92
4.01	Pulau Batam (Indonesia)	2.62	2600	28.1	233
4.02	Pulau Batam (Indonesia)	2.75	2900	26.5	233
4.03	Broadway, GLOU (U.K.)	1.33	975	10.6	43
4.04	Guiyang, GUIZ (China)	1.34	1295	15.2	193
5.01	Willowdale, WA (Austr.)	1.00	1180	23.6	212
5.02	Jarrahdale, WA (Austr.)	0.83	1170	22.5	214
6.01	Alegrete, RGS (Brazil)	1.83	1900	22.1	291
6.02	Santa Maria, RGS (Brazil)	2.70	2450	18.8	25
6.03	Porto Alegre, RGS (Brazil)	1.70	1750	20.6	54
6.04	Mineiros, GOIAS (Brazil)	2.33	2450	24.3	73
6.05	Itaberai, GOIAS (Brazil)	1.65	1700	22.5	314
7.01	Esla River, LEON (Spain)	0.56	450	12.0	35
7.02	Guadalquivir, COR (Spain)	0.75	650	18.2	100
8.01	Lake Danao, LEYTE (Phili.)	2.62	3300	27.2	170
8.02	Ipil, LEYTE (Phili.)	2.12	2500	27.2	170
8.03	Can Adieng, LEYTE (Phili.)	2.33	2450	27.2	170
8.04	Ormoc, LEYTE (Phili.)	2.00	2260	27.2	170
9.01	Minas Gerais, MG (Brazil)	1.35	1470	21.1	306
9.02	Serra de Moeda, MG (Brazil)	1.66	1620	20.5	290
10.01	Brasilia, FD (Brazil)	1.65	1565	21.2	240
10.02	Howard, TX (USA)	0.28	510	17.8	55
10.03	Goainia, GOIAS (Brazil)	1.15	1150	24.7	353
10.04	Gottingen, SAX (Germany)	1.00	750	8.6	36
11.01	Sedghiane, MED (Tunisia)	0.12	235	18.6	55
11.02	Sedghiane, MED (Tunisia)	0.06	190	18.6	55
12.01	Schefferville, QC (Canada)	0.71	820	-5.0	65
12.02	Schefferville, QC (Canada)	0.81	825	-5.0	65
13.01	Cecil, NC (USA)	1.17	1200	19.9	280
13.02	Orangeburg, SC (USA)	1.39	1260	17.3	57
AC2	Williams, AZ (USA)	0.38	550	9.9	41
ALT	Davis Creek, CA (USA)	0.34	315	8.1	55
AME	Honey Lake, CA (USA)	0.05	140	10.3	84
BAL	Santa Paula, CA (USA)	0.27	455	15.7	69
BLAC	Coos Bay, OR (USA)	1.71	1780	11.3	70
BOU	Lucerne Valley, CA (USA)	0.17	100	16.7	31
CA2	Seligman, AZ (USA)	0.29	295	11.2	43
CAU	Moores Creek, NV (USA)	0.09	125	12.4	23
COH	Little Giant, CA (USA)	0.90	1320	16.0	157
DEJ	American House, CA (USA)	2.40	2110	5.3	232
GS2	Casa Grande, AZ (USA)	0.20	215	21.0	23
HODA	Rock Creek, CA (USA)	1.48	1540	6.7	328
ISHI	Humboldt, CA (USA)	1.82	1905	11.0	257
LAV	Adelanto, CA (USA)	0.26	205	16.7	31
LOR	Carr Lake, CA (USA)	1.68	1775	5.3	232
MAR	Brentwood, CA (USA)	0.25	305	16.3	61
MIL	Wasco, CA (USA)	0.14	180	17.3	99
MIN	French Gulch, CA (USA)	1.37	1525	12.1	170
MO	Ann Arbor, MI (USA)	0.85	930	9.7	10
MUR	Rosamond, CA (USA)	0.09	130	17.1	34
N95	Northfield, MN (USA)	0.81	860	6.3	97
NH	Manistee, MI (USA)	0.76	840	8.6	64
OS2	Dexter, MI (USA)	0.68	740	9.6	84
PAR	Boonville, CA (USA)	1.56	1520	11.8	399
PUTT	Emigrant Gap, CA (USA)	1.43	1525	5.3	232
STAG	Camel Peak, CA (USA)	1.95	1970	5.3	232
TIN	Soda Springs, CA (USA)	1.62	1650	5.3	232
USAL	Mendocino, CA (USA)	1.26	1270	10.6	368

1. Singh and Gilkes (1992)
2. Torrent et al. (2010)
3. Geiss et al. (2004)
4. France and Oldfield (2000)
5. Anand and Gilkes (1987)
6. Schwertmann and Kampf (1985)
7. Torrent et al. (1980)
8. Navarette et al. (2008)
9. Curi and Franzmeier (1987)
10. Schulze (1981)
11. Prudencio et al. (2011)
12. Wang et al. (1989)
13. Bigham et al. (1978)

[a] Sample numbers correspond to cited literature list, and named samples are from this study.

[b] Locations are either from the literature, or are the nearest climate monitoring center.

[c] RMMP (range of mean monthly precipitation) is the difference between mean wet-month precipitation and mean dry-month precipitation values.

Appendix B2. Table of mean annual precipitation estimates for the Green River Basin (EECO)

Sample	Age (Myr)	MAP (mm/yr)			
		G/H	CIA-K[a]	DBK[a]	MInA[b]
1	51.95	330 (±157)		448 (±147)	
3	51.92	320 (±157)		392 (±147)	
4	51.90			363 (±147)	
15	51.81	401 (±157)		642 (±147)	
24	51.75		1013 (±181)	501 (±147)	
38	51.59		890 (±181)		
39	51.58		988 (±181)		
40	51.57		715 (±181)		
45	51.53	421 (±157)		363 (±147)	
46	51.52	651 (±157)		392 (±147)	
47	51.51	892 (±157)		620 (±147)	
Wind River	51.50				1040 (+450, -310)
50	51.48	973 (±157)		937 (±147)	
62	51.37	822 (±157)	842 (±181)	937 (±147)	
64	51.35	792 (±157)	1085 (±181)	914 (±147)	
65	51.34		1096 (±181)		
66	51.33		1023 (±181)		
70	51.30	591 (±157)	1104 (±181)	864 (±147)	
71	51.29		579 (±181)		
72	51.28	461 (±157)			
78	51.22			392 (±147)	
82	51.18	290 (±157)		501 (±147)	
87	51.14			475 (±147)	
91	51.10			721 (±147)	
93	51.08	240 (±157)	364 (±181)	526 (±147)	
94	51.05	350 (±157)		642 (±147)	
105	50.98		975 (±181)		
106	50.97	410 (±157)	624 (±181)		
107	50.96		952 (±181)		
112	50.90	360 (±157)		620 (±147)	
Green River	50.50				840 (+360, -250)

[a] Hyland and Sheldon (2013)
[b] Wilf et al. (1998)

Appendix C1. Table of whole rock geochemical ratios of Bt horizons

Sample	Age (Mya)	CIA-K	S	Ti/Al
2DB-7	53.03	33.7	0.48	0.075
2DB-10	53.00	43.8	0.50	0.060
2DB-19	52.92	35.2	0.50	0.072
2DB-30	52.88	45.7	0.47	0.070
2DB-35	52.82	35.1	0.46	0.068
2DB-37	52.80	27.9	0.46	0.070
2DB-41	52.78	33.7	0.49	0.057
2DB-46	52.73	34.3	0.54	0.051
2DB-53	52.64	32.0	0.49	0.070
2DB-55	52.61	22.6	0.52	0.058
2DB-57	52.61	50.3	0.52	0.061
2DB-61	52.36	69.4	0.51	0.039
2DB-64	52.28	48.0	0.47	0.043
2DB-72	52.01	81.5	0.45	0.038
2DB-76	51.84	81.5	0.43	0.047
2DB-79	51.82	43.0	0.38	0.051
2DB-86	51.75	31.5	0.41	0.049
2DB-88	51.70	45.0	0.39	0.051
2DB-92	51.63	80.2	0.41	0.047
2DB-112	51.14	51.7	0.38	0.051
2DB-115	51.10	58.2	0.43	0.053
2DB-117	51.05	51.4	0.38	0.047
2DB-119	50.98	62.0	0.38	0.050
2DB-124	50.84	52.0	0.43	0.051
2DB-127	50.83	70.6	0.42	0.046

Appendix C2. Table of isotopic results from $\delta^{13}C_{cc}$ and $\delta^{13}C_{org}$ analyses

Sample	Age (Mya)	$\delta^{13}C_{org}$ (‰ VPDB)	$\delta^{13}C_{cc}$ (‰ VPDB)
2DB-35	52.81	-25.2	-9.5
2DB-49	52.68	-25.6	-----
2DB-59	52.57	-27.6	-8.8
1DB-4	52.37	-26.4	-----
1DB-16	52.30	-28.0	-----
2DB-63	52.28	-26.1	-----
1DB-18	52.22	-25.8	-----
2DB-65	52.09	-24.2	-----
1DB-20	52.03	-25.6	-----
1DB-24	51.90	-24.6	-7.3
2DB-73	51.84	-25.4	-8.0
1DB-31	51.82	-26.1	-----
1DB-39	51.80	-25.6	-----
2DB-87	51.70	-24.3	-----
1DB-42	51.68	-24.5	-----
1DB-45	51.67	-26.7	-----
1DB-51	51.65	-26.0	-----
1DB-48	51.64	-25.4	-----
2DB-91	51.63	-24.2	-----
1DB-55	51.63	-26.6	-----
1DB-66	51.51	-25.4	-----
1DB-73	51.42	-27.5	-----
2DB-94	51.37	-26.9	-----
2DB-109	51.30	-26.5	-----
2DB-111	51.14	-25.0	-8.4
2DB-118	50.98	-24.6	-----
2DB-121	50.87	-25.8	-----

Appendix C3. Table of phytolith counts and compound groups for diagnostic morphotypes

Morphotype (Strömberg, 2003; 2005)	Compound	1DB-76	1DB-68	1DB-54	1DB-37	1DB-24	1DB-20	1DB-11	1DB-1	2DB-121	2DB-111	2DB-100	2DB-93	2DB-54	2DB-42	2DB-11	2DB-2
Rondels (CO-1, CO-2)	POOID	25	9	10	8	4	4	5	6	6	9	6	21	1	3	0	3
Bilobates (Bl-5)	PACCAD	2	2	0	0	0	1	0	0	0	0	1	0	0	0	0	0
Branch elongate (Epi-10)	GRASS-D	0	0	0	0	0	0	0	0	0	0	0	0	1	0	0	0
Elongates (Elo-8, Elo-18)	DICOT	58	86	88	61	114	109	94	93	101	94	89	96	79	89	92	87
Mesophyll (Kn-4, M-4)	DICOT	24	40	26	42	19	15	24	25	31	18	27	14	19	27	27	34
Trichome (Tri-4)	DICOT	7	14	23	6	3	7	3	4	0	2	8	5	0	0	2	0
Sphere (Cl-1)	DICOT	0	0	0	0	18	14	18	23	14	11	17	8	26	17	29	21
Block (Blo-3)	CONI	28	11	18	27	24	25	25	28	16	19	23	20	45	36	39	32
Echinate (Clm-2)	PALM	6	11	11	7	0	1	0	2	3	3	3	3	0	3	0	1
Block (Blo-6)	FI-GEN	34	8	14	18	22	21	34	19	16	22	18	17	29	13	14	13
Sphere (Cl-4)	FI-GEN	4	12	13	14	8	16	6	10	23	19	19	15	15	11	13	14
Block (Kn-1)	FI-GEN	20	15	11	20	6	10	2	9	3	10	14	13	9	12	9	10
Others (Elo-1, Elo-11, Blo-2)	OTH	46	66	81	108	136	97	68	55	69	78	87	93	74	71	63	45
Aquatics (diatoms, sponges)	OTH	0	0	0	7	0	0	0	3	0	0	5	3	4	0	0	0
TOTAL		254	274	295	318	354	320	279	277	282	285	317	308	302	282	288	260
DIAGNOSTIC		208	208	214	203	218	223	211	219	213	207	225	212	224	211	225	215
GI		27	11	10	8	4	5	5	6	6	9	7	21	2	3	0	3
FI		181	197	204	195	214	218	206	213	207	198	218	191	222	208	225	212
%GI		13.0	5.3	4.7	3.9	1.8	2.2	2.4	2.7	2.8	4.3	3.1	9.9	0.9	1.4	0.0	1.4
%FI		87.0	94.7	95.3	96.1	98.2	97.8	97.6	97.3	97.2	95.7	96.9	90.1	99.1	98.6	100.0	98.6

%GI is calculated as (POOID+PACCAD)/DIAGNOSTIC
%FI is calculated as (DICOT+CONI+PALM+FIGEN)/DIAGNOSTIC

Appendix D1. Magnetostratigraphic data for the Maiz Gordo Formation

Sample name[a,b]	Height (m)[c]	Dec. (˚)	Inc. (˚)	MAD (˚)
PM-1	0	153.3	46.7	12.3
PM-2	4	311.0	-43.7	12.1
PM-3	11	348.5	-56.5	12.8
PM-4	16	003.3	-31.5	6.9
PM-5	25	290.0	-52.4	4.2
PM-6	31	153.0	38.0	13.1
PM-7	36	178.0	48.0	7.2
PM-8	41	350.0	-72.3	9.3
PM-9	48	282.3	-16.0	8.1
PM-10	55	336.3	-43.0	6.9
PM-11	59	358.0	-44.3	9.2
PM-12	64	325.3	-42.3	8.8
PM-13	69	357.0	-46.0	9.1
PM-14	75	336.7	-38.7	10.4
PM-15	79	338.3	-40.0	9.7
PM-16	83	359.7	-23.3	12.2
PM-17	90	345.1	-29.0	13.2
PM-18	97	314.0	-37.5	7.1
PM-19	101	136.5	24.8	9.4
PM-20	107	211.0	61.3	8.1
PM-21	110	162.2	27.0	7.4
PM-22	121	217.3	30.0	11.8
PM-23	131	190.0	58.5	7.8
PM-24	136	336.5	-24.0	10.8
PM-25	141	180.2	10.0	4.5
PM-29	166	008.1	-35.4	14.3
PM-34	236	169.0	14.0	8.2
PM-35	226	040.5	-59.6	4.0
PM-38	193	008.5	-41.0	5.7
PM-39	181	028.2	-39.2	10.1

[a] Sample names refer to paleomagnetic cores (prefix PM) from Cerro Bayo locality.
[b] PM samples are reported as means for sites collected within 1 meter (~3 samples per site).
[c] Height refers to stratigraphic height from base of the Tunal Fm.

Appendix D2. Table of isotopic analyses from Cerro Bayo (Salta, Argentina)

Sample	Height (m)	Average $\delta^{13}C_{org}$ (‰ VPDB)	$\delta^{13}C_{org}$ (A1)	$\delta^{13}C_{org}$ (A2)	C (wt%)
CB-1	19.3	-24.18	-24.39	-23.96	0.036
CB-2	19.0	-21.77	-22.65	-20.88	0.031
CB-3	27.3	-22.13	-22.21	-22.04	0.038
CB-4	26.9	-22.08	-22.08	--------	0.030
CB-5	31.7	-22.15	-22.56	-21.73	0.021
CB-6	31.4	-22.15	-22.15	--------	0.040
CB-7	32.0	-20.96	-20.96	--------	0.010
CB-8	44.2	-22.83	-22.40	-23.26	0.040
CB-9	44.0	-21.53	-21.40	-21.66	0.029
CB-10	46.1	-24.94	-24.93	-24.95	0.023
CB-11	48.4	-24.77	-24.94	-24.60	0.033
CB-12	58.2	-21.50	-21.84	-21.16	0.020
CB-13	58.0	-22.48	-22.48	--------	0.020
CB-15	74.7	-25.10	-24.68	-25.51	0.030
CB-16	77.4	-24.30	-24.64	-23.96	0.063
CB-17	77.0	-22.65	-22.82	-22.48	0.033
CB-18	81.6	-24.62	-24.16	-25.01	0.030
CB-19	81.2	-23.48	-23.68	-23.28	0.017
CB-20	83.1	-26.54	-26.83	-26.25	0.031
CB-21	82.6	-24.77	-24.77	--------	0.030
CB-22	82.3	-22.23	-22.45	-22.00	0.041
CB-23	82.0	-22.29	-22.37	-22.21	0.039
CB-25	97.6	-25.72	-25.72	--------	0.040
CB-26	97.2	-25.44	-25.40	-25.48	0.010
CB-27	96.5	-26.22	-26.62	-25.81	0.030
CB-29	126.4	-26.39	-27.22	-25.55	0.030
CB-30	126.0	-23.16	-23.38	-22.94	0.011
CB-31	135.5	-23.32	-23.92	-22.66	0.020
CB-31.5	136.5	-20.69	-20.79	-20.59	0.023
CB-32	134.9	-21.17	-21.33	-21.01	0.030
CB-33	138.2	-26.21	-26.35	-26.07	0.031
CB-34	137.8	-21.88	-22.00	-21.76	0.025
CB-35	147.2	-28.23	-28.47	-27.99	0.050
CB-36	146.9	-26.11	-26.36	-25.86	0.023
CB-37	164.9	-25.48	-25.55	-25.40	0.009
CB-38	164.6	-26.64	-26.64	-26.64	0.020
CB-39	183.9	-23.12	-23.12	--------	0.010
CB-40	183.6	-23.72	-23.72	--------	0.010
CB-41	183.4	-27.79	-27.92	-27.66	0.050
CB-42	187.2	-24.35	-24.20	-24.49	0.010
CB-44	186.0	-28.04	-28.12	-27.96	0.021
CB-45	219.4	-24.66	-24.54	-24.78	0.040
CB-46	219.0	-20.96	-20.62	-21.30	0.020

Appendix D3. Table of elemental analyses from Cerro Bayo (Salta, Argentina)

Sample	Horizon	SiO_2	TiO_2	Al_2O_3	Fe_2O_3	MgO	CaO	Na_2O	K_2O	P_2O_5	LOI	Total
						wt %						
CB-1	A	57.8	0.87	16.6	6.7	2.3	0.96	2.7	4.6	0.16	7.5	100.5
CB-2	B	54.7	0.91	16.9	7.3	2.3	1.03	3.2	4.2	0.27	8.0	98.9
CB-3	A	52.6	0.99	18.1	7.8	2.7	0.80	2.9	4.9	0.18	8.4	99.5
CB-4	B	55.3	0.90	17.9	7.4	2.4	0.87	3.0	4.7	0.16	7.8	100.5
CB-5	A	55.5	0.88	17.5	7.4	2.3	0.83	3.0	4.6	0.23	7.2	99.6
CB-6	B	51.0	0.97	18.6	8.5	2.8	0.54	2.7	5.3	0.12	9.2	99.7
CB-7	A	61.2	0.85	17.1	5.2	1.7	0.88	4.0	4.0	0.22	5.2	100.5
CB-8	A	56.3	0.91	17.7	6.7	2.0	0.98	3.5	4.6	0.34	5.7	98.8
CB-9	B	54.6	0.97	18.1	7.6	2.2	0.70	3.2	4.8	0.17	6.6	99.1
CB-10	A	62.8	0.63	16.3	4.9	1.4	0.97	3.6	4.0	0.16	4.4	99.3
CB-11	A	57.8	0.85	17.5	6.8	1.9	0.92	3.2	4.4	0.21	6.9	100.5
CB-12	A	54.5	0.86	17.5	7.1	1.3	0.61	3.3	4.9	0.12	8.2	99.5
CB-13	B	57.7	0.79	16.3	6.3	2.0	0.67	3.8	4.3	0.13	7.5	99.5
CB-4	A	62.2	0.78	16.0	5.4	1.5	0.96	3.4	3.9	0.31	4.6	99.2
CB-15	B	62.7	0.79	16.1	5.2	1.5	0.88	3.5	4.0	0.20	4.3	99.3
CB-16	A	50.5	0.98	19.2	8.4	2.6	0.64	2.1	5.3	0.12	8.4	98.3
CB-17	B	53.7	0.94	18.9	7.5	2.4	0.75	2.2	5.1	0.08	8.5	100.0
CB-18	A	60.1	0.69	17.4	4.9	1.5	1.29	4.1	3.7	0.29	5.6	99.6
CB-19	B	59.3	0.87	17.6	5.9	1.9	1.11	2.7	4.7	0.30	5.3	99.8
CB-20	A	61.9	0.66	15.5	5.0	1.7	1.02	2.7	4.3	0.21	7.1	100.0
CB-21	A/B	51.6	0.95	19.0	7.6	2.6	0.73	2.8	5.0	0.26	9.2	99.7
CB-22	B	50.9	0.98	19.3	8.5	2.6	0.57	2.6	5.0	0.16	9.1	99.8
CB-23	B	58.8	0.89	17.9	5.6	2.0	0.73	3.2	4.4	0.10	6.7	100.5
CB-24	A											
CB-25	B	61.7	0.84	16.5	5.3	1.8	0.88	2.9	4.1	0.09	6.1	100.5
CB-26	B	68.1	0.60	14.4	3.8	1.1	0.89	3.2	3.5	0.10	4.3	100.0
CB-27	Bk	62.2	0.74	16.1	4.8	1.7	1.09	2.9	4.1	0.17	6.6	100.5
CB-28	Bk											
CB-29	A	64.9	0.69	15.5	3.8	1.7	0.71	2.5	4.0	0.09	5.8	99.7
CB-30	B	61.7	0.70	15.9	5.5	1.8	0.79	2.3	4.1	0.16	7.7	101.0

Sample	Horizon	SiO_2	TiO_2	Al_2O_3	Fe_2O_3	MgO	CaO	Na_2O	K_2O	P_2O_5	LOI	Total
						wt %						
CB-31	A	61.9	0.68	15.5	5.1	1.8	1.03	2.1	4.0	0.14	7.3	99.6
CB-31.5	B	57.6	0.86	17.1	5.9	2.2	1.16	2.5	4.5	0.20	7.9	100.0
CB-32	B	56.0	0.85	17.4	6.7	2.3	1.14	2.4	4.6	0.21	8.8	100.5
CB-33	A	62.0	0.67	15.4	6.0	1.9	1.25	2.2	4.5	0.33	6.2	100.5
CB-34	B	61.5	0.67	15.6	5.1	1.9	1.74	2.3	4.4	0.45	7.3	101.0
CB-35	A	72.4	0.30	13.3	1.9	0.8	1.31	4.0	2.7	0.09	4.1	101.0
CB-36	B	68.1	0.54	13.2	4.0	1.5	2.15	2.0	4.0	0.99	5.2	101.5
CB-37	A	70.3	0.56	13.4	3.7	1.3	0.93	1.8	3.9	0.08	4.6	100.5
CB-38	B	67.7	0.58	14.2	3.8	1.4	0.64	1.9	4.3	0.10	4.7	99.5
CB-39	A	69.5	0.53	13.1	4.2	1.3	0.44	1.0	4.1	0.09	5.2	99.5
CB-40	B	66.0	0.61	14.4	4.6	1.5	0.54	0.8	4.4	0.14	5.8	98.7
CB-41	Bk	66.2	0.58	13.8	4.3	1.3	1.05	0.9	4.1	0.11	6.3	98.7
CB-42	A	71.8	0.41	11.7	3.2	1.0	0.55	0.7	4.1	0.09	5.1	98.6
CB-43	A/B	71.2	0.38	12.3	2.8	1.0	0.93	1.1	3.9	0.18	5.1	98.9
CB-44	A/B	74.7	0.31	10.5	2.1	0.8	1.33	1.1	3.5	0.08	4.1	98.5
CB-45	A	59.1	0.67	16.5	6.6	1.5	1.36	0.4	4.7	0.81	7.5	99.2
CB-46	B	50.5	0.85	21.6	7.2	2.1	1.54	0.3	5.9	0.88	10.1	101.0

Appendix D4. LOSCAR model setup conditions (preEECO)

Parameter	Symbol	prePETM[a]	preEECO*	Units
Ocean conveyor transport	T	25		Sv
Tethyan transport	Tt	2		Sv
Upwelling (D-M)[b]	tA, tl	0.2, 0.2		---
Mixing (L-M)[b,c]	mlk	13,13,27		Sv
Mixing (H-D)[b,c]	mlk	5,5,8		Sv
Tethyan mixing	mlk	12,1,8		Sv
Initial temperature[d]	Tc	12,16,25,12	14,20,30,14[e]	˚C
Temperature relaxation time[d]	tn	1000, 200, 20		yrs
Salinity	S	34.7		---
Gas exchange (CO_2)	kas	0.06		mol(atm m^2 yr)
Biopump efficiency	fepl	0.80		---
Remineralization (M)[b]	frim	0.78		---
Remineralization (D)[b]	1-frim	0.22		---
P/C in organic C	REDpc	1/130		---
N/C in organic C	REDnc	15/130		---
O/C	REDo2c	165/130		---
C export	feph	1.8		mol m^{-2} yr^{-1}
P export	fpph	0.014		mol m^{-2} yr^{-1}
Rain ratio	rrain	6.7		---
$CaCO_3$ water	vwc	0.31		---
$CaCO_3$ weathering flux	fcc	16		10^{12} mol yr^{-1}
$CaSiO_3$ weathering flux	fsi	6		10^{12} mol yr^{-1}
CO_2 degassing flux	fvc	6		10^{12} mol yr^{-1}
$CaCO_3$ weathering exp.	ncc	0.4		---
$CaSiO_3$ weathering exp.	nsi	0.2		---
$d^{13}C$ weathering	d13cin	2.0		‰
$d^{13}C$ degassing	d13cvc	-4.0		‰
$d^{13}C$ atmosphere	d13ca	-6.5	-5.5[f]	‰
Height of sed. mixing	hs	0.08		m
Density of solids	ps	2500		kg m^{-3}
non-$CaCO_3$ flux	frrf	0.0035		kg m^{-2} yr^{-1}
Porosity of clay	r0	0.85		---
Porosity of $CaCO_3$	r1	0.62		---
Dissolution rate constant	ksd	$20.36x10^{10}$		mol m^{-2} yr^{-1}
Dissolution rate order	nsd	2.40		---

[a] Values from Zeebe (2012) and references therein
[b] D = deep ocean, M = intermediate ocean, L = surface ocean
[c] Atlantic, Indian, Pacific
[d] D, M, L, H (high-latitude)
[e] Creech et al., 2010; Brinkhuis et al., 2006
[f] Tipple et al., 2010

* Values same as prePETM unless indicated

Appendix D5. Specific conditions of LOSCAR carbon scenarios

Scenario	Parameters changed*	Amount changed
1.1 Volcanism	CO_2 degassing flux	+10%
1.2 Volcanism		+25%
1.3 Volcanism		+50%
2.1 Methane	Carbon input flux (100 kyr timescale)	+1000 Pg
2.2 Methane		+3000 Pg
2.3 Methane		+6000 Pg
3.1 Carbonates	Carbonate sediment area (Tethys basin)	-33% (+1135 Pg)
3.2 Carbonates	Carbon input flux (100 kyr timescale)	-66% (+2270 Pg)
4.1 Ventilation	Mixing (L-M), Mixing (H-D), Upwelling (D-M)	+10%
4.2 Ventilation		+25%
4.3 Ventilation		+50%
5.0 Combined	Mixing (L-M), Mixing (H-D), Upwelling (D-M) Carbon input flux (100 kyr timescale)	+50% (+3000 Pg)

* Parameters changed are altered for all scenarios of a given type

Appendix D6. Model exemplars from LOSCAR scenarios failing EECO target criteria